Low Velocity Blood Flow Imaging using Aperture Domain Clutter Suppression Techniques

By

Kathryn Ann Ozgun

Dissertation
Submitted to the Faculty of the
Graduate School of Vanderbilt University
in partial fulfillment of the requirements
for the degree of

DOCTOR OF PHILOSOPHY
in
Biomedical Engineering

August 13, 2021

Nashville, Tennessee

Approved:
Brett Byram, Ph.D. (Chair)

Daniel Brown, M.D.

Charles Caskey, Ph.D.

Michael Miga, Ph.D.

Kenny Tao, Ph.D.

DEDICATION

This thesis is dedicated foremost to my parents, Mary Ann and Bert, as well as to Holly, Michael, and Christian. Thank you for your unconditional support and encouragement.

ACKNOWLEDGMENTS

First, I would like to thank my advisor, Dr. Brett Byram for the privilege of being part of the BEAM lab. His encouragement, supervision, and support have been invaluable for my academic and personal growth during the course of my PhD. I am grateful for his mentorship and technical insight, particularly during an unprecedented year of remote work due to the COVID-19 pandemic. I would also like to thank my committee members for their time, feedback, and guidance during my time at Vanderbilt. I particularly thank Dr. Michael Miga and Dr. Dan Brown for facilitating my clinical research experiences.

I thank the members of the BEAM lab for their collaboration and camaraderie. In particular, I thank Jaime Tierney-Stanton, Kaz Dei, and Kristy Walsh for their mentorship and support when I was a junior graduate student. I thank Sigi Schlunk for his companionship throughout graduate school, including our time at Siemens, our travel in Japan, and our numerous game nights. Finally, I am grateful for my many fun memories with Abbie Weeks, Chris Khan, and Emelina Vienneau, especially during our collaboration in lab, VISE events, and trips to Taco Bell.

I appreciate the encouragement I received to participate in research as an undergraduate, especially from Dr. David Lalush, Dr. Greg Bashford, Dr. Paul Dayton, and Dr. Brooks Lindsey. I also thank Dr. Dongwoon Hyun for sharing the spatcov library for fast spatial coherence computation, as well as the contributors to the UltraSound ToolBox library.

I thank Dr. Abhay Patil and the Advanced Development team at Siemens for hosting me for an internship. I am particularly grateful for the mentorship provided by Dr. Lei Sui, Dr. Aaron Engel, and Dr. Stephen Rosenzweig.

I gratefully acknowledge my funding support from the National Institute of Biomedical Imaging and Bioengineering (T32-EB021937) and from the National Science Foundation (IIS-1750994).

I am thankful to my friends for so many wonderful memories in Nashville. I especially glad to have met my roommates, Allison Bosworth and Natalie Noll (and our cat Mittens), and to have spent five fun years together. I would also like to thank Jonah Rosch, Mohsin Rahim, Prarthana Patil, Kyle Garland, Ella Hoogenboezem, Dickie D'Arcy, Evan Glass, and Stephanie Pearlman for their friendship.

I particularly thank my boyfriend of seven years, Dr. Christian Pedersen, for celebrating all of my victories and for supporting me through the challenges of graduate school. He is my best friend and biggest role model. I am so proud of the hard work he put forth to complete his PhD and I am excited for our adventure to come.

Finally, I attribute many of my achievements to the support of my family. I am thankful that my parents helped me develop a strong academic foundation and have always encouraged my interests in science, math, and technology. I thank my mother for always being willing to proof-read my technical writing and I thank my father for introducing me to the field of medical imaging. I am also grateful to have a close relationship with my siblings, Holly and Michael, who have always supported me along the way.

TABLE OF CONTENTS

LIST OF TABLES

LIST OF FIGURES

Figure Page

LIST OF ABBREVIATIONS

HCC	Hepatocellular Carcinoma
TACE	Transarterial Chemoembolization
BCLC	Barcelona Clinic Liver Cancer
mRECIST	Modified Response Evaluation Criteria in Solid Tumors
PRF	pulse repetition frequency
PWSF	plane wave synthetic focusing
VCZ	van Cittert-Zernike
SNR	signal-to-noise ratio
CNR	contrast-to-noise ratio
SCR	signal-to-clutter ratio
IIR	infinite impulse response
FIR	finite impulse response
SVD	singular value decomposition
HOSVD	higher-order singular value decomposition
PD	Power Doppler
CFPD	Coherent Flow Power Doppler
ppCFPD	power preserving Coherent Flow Power Doppler
INV	inverse normalized variance estimator

LIST OF SYMBOLS

$\lambda = \frac{c}{f_0}$	Wavelength
μ	Mean
σ^2	Variance
A	Number of Frames
c	Speed of sound, assumed to be 1540 m/s in tissue
D	Array Size
f_0	Transmit center frequency
$F_{\#} = \frac{Z}{D}$	F-number, the ratio of depth to transducer array length
f_s	Receive sampling frequency
$M = XZ$	Number of Samples
N	Number of Elements
N_{ang}	Number of Plane Wave Transmissions
N_{lines}	Number of Focused Scanline Transmissions
v	Blood Flow Velocity
X	Number of Lateral Samples or Lateral Dimension
Z	Number of Axial Samples or Axial Dimension

Chapter 1

Background and Introduction

1.1 Clinical Motivation

In the United States, liver cancer incidence is rising at a higher rate than any other cancer type, increasing by 2-3% per year [1]. The most common form of liver cancer is Hepatocellular Carcinoma (HCC), which comprises >90% of cases [2]. Despite advances in clinical care, less than 30% of patients are eligible for curative surgical intervention and the five-year survival rate for HCC remains below 20% [2, 3]. Overall, liver cancer is a leading cause of cancer-related death, accounting for roughly 300,000 deaths in the United States over the past two decades [4].

Liver cancer is associated with a poor prognosis due to the prevalence of advanced-stage disease at diagnosis. The Barcelona Clinic Liver Cancer (BCLC) scoring system is widely used to stratify HCC into five levels (0, A-D) based on morphological (number and size of lesions) and functional (Child-Pugh score and bilirubin) parameters [5, 6]. Only patients that have early stage (BCLC-A) HCC with 3 or fewer small lesions are eligible for curative liver transplantation [7]. For intermediate and advanced stage HCC, locoregional therapies are employed for tumor down-staging, bridge to transplantation, and palliative care.

Transarterial Chemoembolization (TACE) is the preferred locoregional therapy for the treatment of intermediate-stage HCC [8]. Conventional TACE involves the delivery of a chemotherapy drug in Lipiodol, an ethiodized oil, to the tumor site. An embolic agent is then injected into the tumor's feeding vasculature to improve chemotherapeutic retention and elicit tumor ischemia. TACE has been shown to prolong survival up to 5 years, though the objective response rate is reported from 51-76 % [9–13]. TACE outcome variability is partly attributed to insufficient intraprocedural assessment of embolization endpoints [14].

Repeat TACE treatment is typically performed ‘on demand’ based on therapeutic response, rather than at fixed intervals [8, 11, 15]. However, therapeutic efficacy cannot be established until 4-6 weeks following the procedure, which may delay additional sessions [8, 10, 16]. Therapeutic efficacy is assessed using contrast-enhanced computed tomography (CT) or magnetic resonance imaging (MRI) and measured using the mRECIST criteria, as shown in Table 1.1 [8, 17]. Earlier assessment is precluded by confounding imaging features including lipiodol deposition for CT and inflammation on MRI [8, 18].

In clinical practice, sufficient embolization is qualitatively evidenced by contrast backflow on digital subtraction angiography (DSA). Efforts to standardize grading of progressive embolization based on the appearance of antegrade flow and tumor blush have not been widely adopted due to inter-reader variability [14, 19]. Quantitative measures, including contrast time-to-peak and tumor blood supply time, have shown preliminary efficacy [19, 20]. However, a drawback of angiography is the necessity for contrast injection, which prevents continuous real-time imaging. Additionally, the field of view on DSA is limited to the extent of contrast diffusion; as a result, tumor-feeding vessels may be missed in roughly 20% of cases [21].

Contrast-enhanced and power Doppler ultrasound modalities have also been considered for early assessment of tumor response to TACE. Contrast-enhanced ultrasound (CEUS) involves the application of a harmonic pulse to induce cavitation of an intravascular microbubble contrast, which yields enhancement of viable tumor. CEUS methods including time-intensity analysis, morphological feature detection, and qualitative enhancement have been proposed for TACE evaluation as early as 1-2 weeks post-treatment [18, 22]. Immediate post-procedural evaluation is impaired by tumoral hyperenhancement induced by trapped air bubbles, necrotic gas formation, and the deposition of drug-eluting beads (DEB) used in DEB-TACE [18, 23, 24]. Non-contrast power Doppler has consequently been proposed for immediate evaluation of blood flow in liver lesions, as power Doppler is less susceptible to hyperenhancing artifacts and is not limited by contrast dose. Historically,

Response	**Qualification**
Complete Response	Complete disappearance of arterial enhancement in all lesions.
Partial Response	At least 30% decrease in sum of diameters of enhancing lesions from pre-treatment baseline.
Stable Disease	Intermediate cases that do not qualify for PR or PD.
Progressive Disease	At least 20% increase in sum of diameters of enhancing lesions from pre-treatment baseline.

Table 1.1: mRECIST Classification

power Doppler evaluation of blood flow in liver lesions suffered from poor sensitivity toward low velocity blood flow; however, the development of advanced methods for motion compensation, high frame rate imaging, and filtering have aided in overcoming these barriers [25, 26].

Prior research performed by Tierney *et al.*demonstrated that non-contrast power Doppler can detect changes in blood flow induced by TACE [27]. This thesis builds on these findings and presents two techniques to improve visualization of low velocity blood flow using ultrasound. The clinical objective of this research is to establish the feasibility of using non-contrast ultrasound during TACE procedures for immediate evaluation of therapeutic response.

1.2 Fundamentals of Ultrasound Imaging

1.2.1 Transmission and Reception

Pulse-echo ultrasound imaging involves the transmission of an acoustic wave into the body and subsequent reception of reflected echo signals, which are reconstructed to form an image. Transmission and reception events are controlled by an ultrasound transducer, which contains one or more piezoelectric elements arranged in a linear or curvilinear geometry. During transmission, the elements are excited in succession by a phased voltage to achieve wavefront steering and focusing. The spherical wavefields produced by each element combine to form a unified wavefront, as characterized by Huygen's principle [28].

Reflected echoes arise due to acoustic impedance mismatches at region boundaries, as well as from impedance inhomogeneities throughout a scattering medium. The size of the scattering object (*e.g.* the scatterer) influences the scattering characteristics of an incident wavefront. Bodily tissues are primarily composed of acoustic scatterers that are much smaller than the acoustic wavelength, which produce diffuse Rayleigh scattering. For instance, blood is effectively modeled by a collection of sub-resolution scatterers. However, some anatomical boundaries and structures, such as bone, yield strong specular reflections [28]. The amplitude of the received echo signal represents the superposition of these numerous scatterered echoes, which gives rise to the unique contrast and speckle texture of anatomy in ultrasound images.

Acoustic scattering by a diffuse medium is much weaker than the incident wavefront, so higher-order scattering events can be neglected [29]. This assumption, known as the Born approximation, implies that received echoes have undergone a single scattering event. As a result, the depth of a target, d, can be measured based on the time, t, at which the echo signal is received as $d = ct/2$, where c is the speed of sound in tissue (1540 m/s [30]). This relationship is fundamental for beamforming, the process of ultrasonic image formation.

1.2.2 Conventional B-Mode Imaging

After transmission, the N_{elem} elements of the transducer record the backscattered echoes. The echoes are sampled at a high rate, forming a time-series of length T_{fast} along 'fast-time'. After a complete transmit-receive cycle, the transducer has recorded a matrix, $x \in \mathbb{R}^{T_{fast} \times N_{elem}}$, known as channel data.

The process by which an ultrasound image is reconstructed from the channel data is termed 'beamforming'. Beamforming is a means to preferentially focus the sampled

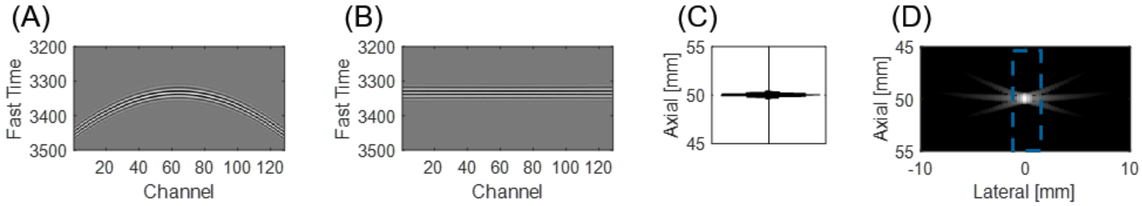

Figure 1.1: The process of delay-and-sum beamforming. (A) The transducer samples the received echo, forming channel data. (B) Focusing is achieved by time-delaying the channel data. (C) The contributions of each channel are summed to produce a scanline of radiofrequency (RF). (D) Multiple scanlines are acquired and displayed on a log-scale as the B-mode image.

echoes using propagation time relations. The generic method for beamforming is termed ‘delay and sum’ beamforming, as outlined in Figure 1.1. Delay and sum beamforming first involves delaying the channel data along fast-time to align the echoes returning from a specific spatial location. The delayed channel data is then summed across the channel dimension, which forms a scanline of radiofrequency (RF) data. Repeating this process for consecutive lateral locations forms the image matrix. For tissue imaging, envelope detection and log compression are performed, which yield the anatomical Brightness Mode (B-mode) image.

1.2.3 Blood Flow Imaging

Non-contrast ultrasound imaging of blood flow comprises four principal imaging modes: continuous wave, pulse wave, color Doppler, and power Doppler. These methods leverage principles of the Doppler effect to generate images of spectral, velocity, or power characteristics of blood flow.

When an ultrasonic wave interacts with a moving scatterer, the echoes exhibit a frequency shift characterized by the Doppler effect. This frequency shift may be observed by comparing the transmitted and received echo frequencies, described by

$$f_d = f_r - f_0 = 2 f_0 \frac{v \cos(\theta)}{c} \tag{1.1}$$

where f_d is the Doppler shift frequency, f_r is the frequency observed by the receiver, f_0 is the transmitted center frequency, and $v\cos(\theta)$ describes the axial component of the scatterer velocity for a vessel positioned at an angle of θ relative to the transducer [28].

Continuous wave Doppler operates by directly measuring the frequency shift between the transmitted and received signal. CW systems employ two transducer elements to transmit and receive continuously, which enables measurement of velocity. CW imaging cannot resolve range or spatial information, so the CW signal is often presented in a spectral or audio format.

Pulse wave systems enable range resolution by transmitting a series of short pulses. Measuring the Doppler shift directly is non-trivial for pulse wave techniques due to attenuation and pulse-length limitations [28]. As a result, the Doppler shift is measured from consecutive echoes, which form the 'slow-time' dimension. For a given frame rate, T_{prf}, a scatterer moving with an axial velocity, v_z, will exhibit an axial translation proportional to $T_{prf}\ v_z$ between consecutive frames. Using the lag-one correlation between successive complex echoes, R, a phase angle can be estimated as

$$\angle = atan\frac{Im(R)}{Re(R)} \tag{1.2}$$

where atan is the four-quadrant arctangent bounded by $[-\pi : \pi]$, which corresponds to displacements between $[-\frac{\lambda}{2} : \frac{\lambda}{2}]$. Using the complex demodulated RF signal, a velocity estimate can be derived as

$$v_{1D} = \frac{c}{2}\frac{f_{prf}}{2\pi}\frac{atan(\frac{Im(R)}{Re(R)})}{f_0 f_s}. \tag{1.3}$$

Averaging over a two dimensional kernel may also be implemented to reduce jitter [31–33]. Of note, the maximum velocity that can be estimated is bound by

$$v_{max} \leq \frac{c}{2}\frac{f_{prf}}{2f_0}. \tag{1.4}$$

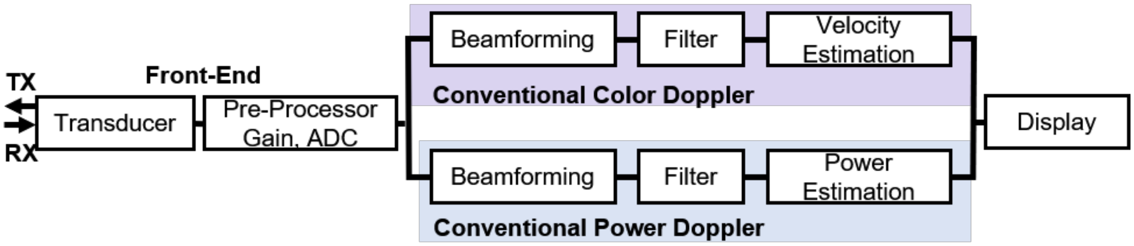

Figure 1.2: Color and Power Doppler employ a similar processing methodology. Color Doppler images display the velocity, measured using a lag-one correlation between successive frames. Power Doppler images display the energy, measured using a zero-lag correlation.

Conventional pulse wave imaging presents the spectral or velocity information for a signal returning from a selected range. Color Doppler imaging employs a similar methodology to estimate the mean velocity, rather than the spectra. Color Doppler yields a complete image of blood flow where the velocity is encoded as a color intensity. Alternatively, the signal energy (*e.g.* power) can be encoded by the intensity, which forms a power Doppler image. The general processing pipeline for power and color Doppler imaging is shown in Figure 1.2

1.3 Power Doppler Imaging

The work in this thesis primarily considers power Doppler imaging techniques. Power Doppler images measure the power of the Doppler spectra, which is proportional to the number of scatterers per voxel to a first approximation [34]. Power Doppler is considered to offer higher sensitivity toward blood flow than color Doppler; this is because noise signals often have a uniform power density, producing a single intensity in power Doppler image, whereas in color Doppler, the random phase of noise presents as a multitude of random velocities [28]. In addition, power Doppler is less prone to aliasing and is independent of insonation angle.

Power Doppler images are produced by estimating the lag-zero autocorrelation of the filtered Doppler signal, as shown in Equation 1.5. Averaging over an axial kernel may additionally be introduced to improve the estimation, as described by Loupas *et al.*[31]. High-pass filtering is necessary to remove the stationary tissue signal, which can be 40-100 dB larger than the blood signal.

$$PD = \sum_{a=1}^{A} |RF(a)|^2. \tag{1.5}$$

The magnitude of a power Doppler image is linearly proportional to the number of moving blood scatterers within a pixel, termed the 'fractional moving blood volume' [34]. The scattering of ultrasound by blood is primarily attributed to red blood cells. The average diameter of a red blood cell is 7 μm, which is much smaller than typical wavelengths used for clinical ultrasound imaging (approximately 0.1 - 1 mm) [35]. As a result, red blood cells produce diffuse Rayleigh scattering proportional to the fourth-power of the imaging frequency. Scattering is additionally influenced by a number of complex parameters, including hematocrit, flow turbulence, and shear effects [34, 35]. However, blood can be generally modeled as a collection of scatterers; by applying the principle of superposition, the total backscattered echo is the sum of the echoes produced by each scatterer. Therefore, the magnitude of the backscattered echo encodes the number of blood scatterers in a first approximation [34]. The relationship between power Doppler image intensity and changes in blood flow has been leveraged for semi-quantitative assessment of functional activity and therapeutic response [27, 36, 37]. However, the primary role of power Doppler in clinical settings is for qualitative assessment and detection tasks.

1.4 Challenges for Low Velocity Blood Flow Imaging

The presence of residual tissue, noise, and acoustic 'clutter' (*e.g.* reverberation, off-axis scattering) signals cause ultrasound image degradation which can lead to exam failure. Clinical failure rates for non-contrast ultrasound detection of hepatocellular carcinoma ranges from 20-50%, particularly for patients with obesity and cirrhosis [38, 39]. Overall, the reported sensitivity of ultrasound B-mode surveillance for hepatocellular carcinoma is approximately 60% [39, 40]. Additionally, non-contrast power Doppler evaluation of intertumoral vascularity in the liver has historically suffered from poor image quality, with sensitivity reported below 40% [26, 41]. In this section, two primary barriers for power Doppler addressed in this thesis are identified.

1.4.1 Limitations Due to the Signal-to-Noise Ratio

The first obstacle for robust Doppler imaging is discriminating low amplitude ultrasonic echoes arising from deep imaging targets. The transmitted wavefront is susceptible to attenuation and aberration effects, which limits the penetration of the ultrasound signal. As a result, received echoes from deep targets are difficult to distinguish from acoustic clutter signals and thermal noise, which manifests as a poor SNR.

Thermal noise, which arises from electronic components, is often modeled as an additive random noise source with a uniform power spectrum. This noise is biased by imaging settings such as time-gain compensation, which leads to a spatially-variant noise profile. Thermal noise limits the detection of weak blood flow echoes and increases measurement jitter, imposing a fundamental lower bound on the variance of estimators [42]. Methods to reduce noise include digital and morphological filtering operations, coherence-based beamforming, and post-processing techniques to equalize bias [43–45].

Propagation through non-homogeneous mediums also degrade the received echo signal due to aberration. Phase aberration is caused by sound speed variations that distort the echo wavefront. These distortions decrease focusing efficacy, which reduce the lateral resolution, signal-to-noise ratio (SNR), and contrast. Efforts to correct aberration often employ phase screen models or channel-domain correlations to estimate the errors in beamforming [46, 47].

Layered subcutaneous tissue boundaries additionally cause reverberation artifacts, which are a form of acoustic clutter. Reverberation is a primary form of image degradation in ultrasound imaging that occurs when echoes undergo multiple reflections before being received by the transducer. Conventional beamforming methods invoke the Born approximation, which models scattering events as linear, single scattering events. However, in the presence of large impedance mismatches, higher-order or multiple scattering events become non-negligible [48]. Reverberant echoes received by the transducer have delayed arrival times relative to a single scattering event, which results in artifacts and degraded axial resolution [49]. Reverberation clutter can be characterised as coherent or diffuse, arising from strong specular boundaries or propagation paths through a specular medium, respectively [50]. Techniques to address reverberation are primarily focused on aperture-domain processing methods, including spatial coherence and non-linear modeling techniques [51, 52].

1.4.2 Limitations Due to Signal Separation

The second barrier for low-velocity blood flow imaging is the presence of dominant tissue signals. Since blood is a weakly scattering medium, the tissue echo can be 40-100 dB larger than the blood echo [52, 53]. To remove the tissue signal from Doppler images, a filter is applied to the radiofrequency data prior to velocity or power estimation.

Tissue rejection filters typically operate along the ensemble (slow-time) dimension of the data. Tissue signals are largely characterized by low frequencies, under the assumption that tissue is relatively stationary. In comparison, blood signals incur a Doppler shift proportional to their velocity, as described in Eq. 1.1. Filters that are based on Fourier domain separation, including finite impulse response (FIR) and infinite impulse response (IIR), are widely used. Time-domain methods, such as polynomial regression filters, have also been proposed [54, 55].

However, these filters suffer when the frequency characteristics of the blood signal and tissue signal overlap. Motion induced by the sonographer and physiological effects can result in a non-zero mean Doppler frequency of the tissue signal. Similarly, accelerative motion increases the tissue signal bandwidth. As a result, there is often a trade-off between preservation of low velocity blood flow and rejection of the tissue signal. Historically, this has imposed a minimum resolvable blood flow velocity of 5 - 15 mm/sec for clinical Doppler imaging [53].

To overcome these limitations, adaptive filters that employ blind source separation have been developed. Blind source separation techniques generate a set of underlying source signals, or bases, that characterize the dominant directions of variance in the data. Filters that employ blind source separation methods, including SVD, can therefore enable more adaptive separation of the blood signal and tissue signal in clinical conditions [56, 57].

1.5 Techniques for Low Velocity Blood Flow Imaging

To overcome the barriers of poor SNR and signal separation for reliable imaging of low velocity blood flow, several advanced imaging methods have been proposed. This section will discuss methods considered in this thesis, as well as discuss remaining challenges.

1.5.1 Plane Wave Synthetic Focusing

In conventional focused ultrasound imaging, the medium is sequentially illuminated using a series of focused transmits. Transmit focusing is achieved by time-delaying the pulse emission from each element of the array such that the wavefront converges at a specified focal depth. During beamforming, synthetic aperture methods may be performed to

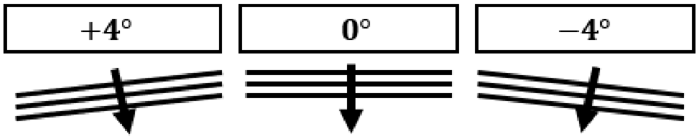

Figure 1.3: To perform plane wave synthetic focusing, multiple plane waves are steered along different angles.

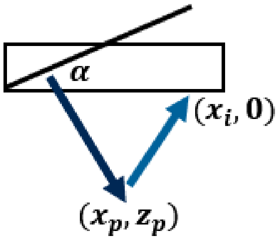

Figure 1.4: Time-of-flight for plane wave imaging.

$$t_d(i) = \frac{z_p\cos(\alpha) + x_p\sin(\alpha) + \sqrt{(x_p - x_i)^2 + z_i^2}}{c} \tag{1.7}$$

achieve uniform focusing over the insonated field. However, multiple focused transmits are required to form a complete image, which limits the achievable frame rate.

Ultrasonic imaging at high frame rates is desirable for imaging of low velocity blood flow. High frame rates enable a longer temporal ensemble to be accumulated so that Fourier-based filters with a higher roll-off and adaptive filters can be implemented. To achieve high frame rate imaging without limiting the field of view, unfocused plane wave or diverging wave sequences can be used to illuminate a broader region during transmission. In plane wave imaging, several transmit events are performed where the plane wave is steered along different tilt angles, as shown in Figure 1.3. Transmit focusing is synthetically achieved by summing the time-delayed echo data obtained from each steered transmit. The time delay for each transmit is computed using the geometric time-of-flight, shown in Equation (1.7). As a result, the time required to form an image is

$$t_{\text{image}} = \frac{N_{\text{ang}} * 2 * z_{\text{max}}}{c}, \tag{1.6}$$

where N_{ang} is the number of angled plane wave transmissions compounded to form an image. Since plane wave sequences illuminate a broader region, fewer transmissions are required to form an image in comparison to focused sequences, enabling a higher frame rate.

The plane wave sequence is characterized by the angular span and number of transmissions, which influence the resolution, contrast, and frame rate of the imaging system. The lateral image resolution depends on the maximum steering angle, $\alpha_{\max}$. For a given angle, the F-number can be expressed as

$$F_{\#} = \frac{z}{D} \approx \frac{1}{2\alpha_{\max}}. \tag{1.8}$$

where z indicates the imaging depth and D is the aperture size [58]. The number of angles affects the contrast of the image as the summation of N emissions yields a $\sqrt(N)$ gain in SNR. Since the number of angles incurs a trade-off between image quality and frame rate, sparse angular sequences are often used for high-frame-rate blood flow applications [59]. However, decimation of the angular sequence introduces grating lobes, which decreases image quality [58].

1.5.2 Spatial Coherence Beamforming

In addition to delay and sum beamforming, several adaptive beamformers have been developed that employ measures of spatial coherence. Spatial coherence is derived from statistical optics, and in ultrasound, refers to the covariance of fast-time signals recorded by a pair of transducer elements. The van Cittert-Zernike (VCZ) theorem describes the

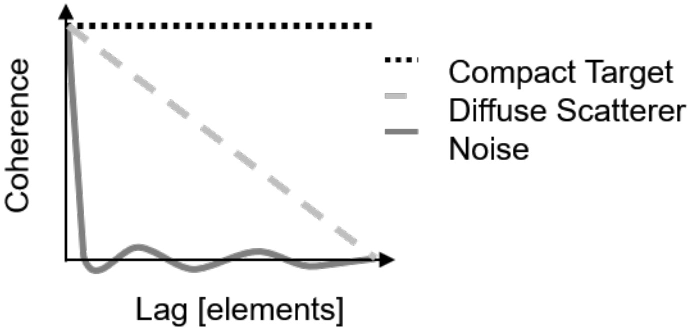

Figure 1.5: The van Cittert-Zernike theorem characterizes the spatial coherence function of a diffuse scatterer. For a rectangular transmit aperture, the spatial coherence is a triangular function. In comparison, noise is uncorrelated in the aperture domain.

development of wavefront coherence as a wave propagates away from an incoherent, quasi-monochromatic source [60]. In the context of ultrasound, the backscattered echo produced by an incoherent scattering medium such as tissue is functionally equivalent to the medium acting as an incoherent source. As a result, the coherence of the echo observed at two channel positions takes a predictable form [61]. For a pair of time-delayed channel signals, $y_1(f)$ and $y_2(f)$, at a given depth, z, the spatial coherence may be written as

$$\breve{R}(x_1, x_2, z, f) = y_1(f)y_2(f) = \frac{\chi(f)}{z^4} R_o\{x_1 - x_2\}, \tag{1.9}$$

where $\chi(f)$ is the scattering function and R_o is the autocorrelation of the transmit aperture function evaluated as a function of the spatial separation between the channels, $x_1 - x_2$. This is a favorable result, as we note that the spatial coherence is not dependent on the actual locations of the observation points, but rather the distance between them.

The predictable spatial coherence of echo signals can be used to differentiate and reject extraneous clutter signals. In the case of an unapodized linear array with N elements, the aperture function, $O(x)$, is a rectangular function so we obtain a triangular coherence function for tissue and blood, $\Lambda[\frac{m}{N}]$, as shown in Figure 1.5 [61]. In comparison, signals produced by noise, reverberation, and off-axis scattering are largely uncorrelated, producing a coherence function modeled by a delta function. Tissue and blood echoes can be readily distinguished from clutter using spatial coherence measured between elements separated by a short distance, or lag, m; this characteristic is the basis for 'short-lag spatial coherence' beamforming.

1.5.2.1 Short Lag Spatial Coherence

Short lag spatial coherence (SLSC) is an image formation method that depicts the spatial coherence of the backscattered echo. Rather than performing a delay and sum process to obtain radiofrequency data, the channel data is only delayed to form 'aperture data'. After applying the focusing delay, the signals recorded by each channel are aligned. SLSC computes the normalized coherence (*e.g.* correlation) between pairs of aperture signals recorded at separate channels. This is measured as

$$R(m) = \frac{1}{N-m}\sum_{i=1}^{N-m} \frac{\sum_{n=n_1}^{n_2} y_i(n) y_{i+m}(n)}{\sqrt{\sum_{n=n_1}^{n_2} y_i^2(n) \sum_{n=n_1}^{n_2} y_{i+m}^2(n)}}, \tag{1.10}$$

which is calculated for all pairs of time-delayed, filtered RF channel signals, y_i and y_{i+m}, separated by a given lag, m, within an axial window between n_1 and n_2. The SLSC metric, or pixel intensity, is then computed by summing the normalized coherence over a set of M lags, as

$$V(a) = \frac{1}{M}\sum_{m=1}^{M} R(m). \tag{1.11}$$

1.5.2.2 Coherent Flow Power Doppler

Coherent Flow Power Doppler is an image formation method for blood flow imaging that employs the SLSC technique. Using an ensemble of channel data that has been filtered to reject the tissue signal, the SLSC metric for each frame can be computed as shown in Eq. 1.11. The SLSC metric is then squared and summed to form an image qualitatively similar to power Doppler, as

$$\text{CFPD} = \sum_{a=1}^{A} V(a)^2. \tag{1.12}$$

Unlike power Doppler, which displays the signal power, CFPD images portray the normalized spatial coherence. As demonstrated by Li *et al.*, normalized spatial coherence may be utilized to improve sensitivity toward blood flow in cluttered environments [62]. However, the non-linear response of CFPD toward the signal power limits sensitivity toward changes in blood flow, which is valuable for functional and therapeutic assessment. To address this barrier, we proposed a modified form of CFPD called 'power preserving CFPD', described in Chapter 2.

1.5.3 Adaptive Filtering

In traditional blood flow imaging algorithms, the tissue signal is removed via application of an FIR, IIR, or polynomial regression high pass filter. However, the performance of these filters relies on the separation of tissue and blood signals in the Fourier or polynomial domain. This assumption is often violated in clinical environments, where spectral overlap can occur due to tissue motion. In addition, conventional high pass filters face a number of practical drawbacks: FIR filters have wider transition bands, IIR filters require appropriate initialization to reduce the transient response, and polynomial regression filters require appropriate regression modeling of the clutter space [54, 55, 63].

Filters that employ singular value decomposition have demonstrated strong performance for visualizing low-velocity blood flow in clinical environments [57, 64, 65]. Singular value decomposition (SVD) is a matrix factorization technique that can be used to perform clutter rejection for blood flow imaging. SVD filtering can be advantageous over conventional methods because (1) it is inherently adaptive, as the basis set is defined by the covariance characteristics of the data, and (2) temporal and spatial features can be used to classify and reject clutter signals. The SVD of the matrix X is given by

$$\mathrm{SVD}(X) = USV' = \sum_k \sigma_k u_k v_k', \tag{1.13}$$

where σ_k is the k^{th} singular value, with u_k and v_k as the corresponding left and right singular vectors. The symbol $'$ indicates the conjugate transpose. The singular vectors characterize the dominant features of the data, conventionally along the spatial (U) and temporal (V) dimensions. Singular values indicate the scale of each singular vector. The singular value/vector pairs are ordered by descending energy, meaning the features that characterize the greatest proportion of the data are contained in the first few singular vectors.

To perform SVD filtering on Doppler RF or complex (IQ) data, the depth and lateral spatial extents are often combined in a Casorati form [1]. This produces a 2-D data matrix,

$X \in \mathbb{C}^{N \times M}$, with N spatial samples and M frames. Alternative formulations have been posed to iteratively filter single A-line, single depth, and higher-order data matrices [54, 66–68].

After decomposing the data into its constituent singular value and vector matrices, filtering is performed by weighting or zeroing components that correspond to clutter or noise. The set of components to remove is determined manually or with a classifier that leverages a priori assumptions about the data features. After clutter rejection, the filtered matrix is reconstructed. Early techniques manually discarded subspaces corresponding to eigenvalues exceeding a pre-defined energy, as tissue is expected to correspond to higher magnitude signal components than blood [55, 69]. More recently, a number of adaptive techniques have been proposed to leverage characteristics of slow-time and fast time singular vectors, as well as attributes of the singular value curve. This enables filtering on the basis of spatial or temporal characteristics.

Limited research has been performed to investigate SVD-based filtering of aperture data. The rationale for SVD-filtering of aperture data is that the predominant or first k largest subspaces are likely to correspond to main lobe signals, whereas off-axis signals will accumulate in later subspaces. Initial studies have demonstrated that using singular value thresholding techniques can effectively suppress these off-axis signals, which can be used to reduce focusing errors in synthetic aperture data and improve minimum variance weighting [69–71]. To improve visualization of blood flow in poor SNR environments, we propose the application of a higher-order SVD filter applied to aperture data, described in Chapter 3.

1.5.4 Summary

Non-contrast ultrasound has substantial potential for assessment of low velocity blood flow in the liver. The development of high-frame-rate acquisitions, motion compensation techniques, and adaptive filters have aided in resolving these barriers, but clinical imaging of low-velocity blood flow remains challenging [26, 41, 72]. In this thesis, two aperture domain technologies are presented and evaluated for immediate post-operative evaluation of TACE procedures.

Chapter 2

Spatial Coherence Beamformer Design for Power Doppler Imaging

This work has been reprinted, with permission, from [73] K. Ozgun, J. Tierney, and B. Byram, ”A spatial coherence beamformer design for power Doppler imaging,” *IEEE Transactions on Medical Imaging*, vol. 39, no. 5, pp. 1558–1570, 2019. © 2019 IEEE.

2.1 Introduction

Assessment of blood flow using ultrasound has substantial clinical utility for diagnosis and surveillance. However, achieving adequate visualization in all patients remains a challenge for power Doppler imaging. Extraneous signals imposed by thermal noise, off-axis scattering, and reverberation can degrade image quality and obscure perception of blood flow [53, 74, 75].

A number of signal processing techniques may be used with conventional beamforming to improve sensitivity toward blood flow [76, 77]. Ultrafast acquisition sequences employ synthetic aperture focusing to amend the reduction in image quality inherent to unfocused transmissions [59, 78]. To improve rejection of the tissue signal, advanced filtering techniques, such as eigen-based filtering, have been proposed [55–57]. Further, filtering efficiency can be improved through down-mixing and motion compensation techniques [55, 79].

Despite these advancements, however, conventional delay-and-sum beamforming remains susceptible to acoustic clutter and thermal noise. This has motivated the development of coherence-based beamformers, which use aperture domain coherence as the basis of image formation rather than the magnitude of echo reflectivity [52, 62, 80].

Aperture domain, or ‘spatial’ coherence quantifies the similarity between echo signals received by a pair of elements. Mediums with diffuse structure, such as tissue or blood, exhibit a characteristic coherence behavior described by the van Cittert-Zernike (VCZ) theorem [60]. As described by Mallart and Fink, the spatial coherence function of these signals is proportional to the autocorrelation of the transmitter's aperture function [61, 81]. In comparison, thermal noise and several forms of acoustic clutter are regarded as spatially incoherent signals [49, 82]. As a result, the coherence of aperture domain data can be leveraged to achieve suppression of acoustic clutter and thermal noise.

Li *et al.*established a coherence-based beamforming technique for blood flow visualization called CFPD, which employs a measure of correlation between received echo signals. In a number of studies, CFPD has demonstrated greater sensitivity over conventional PD in cluttered environments [45, 62, 83]. However, a drawback of CFPD is that the image intensity portrays the normalized echo coherence, which is influenced by the signal-to-noise ratio [82, 84]. This implies that CFPD image intensity does not scale linearly with respect to blood signal power, but rather as a function of the relative noise power.

The non-linear relationship between CFPD image intensity and echo power compromises quantification of blood flow volume. In comparison, PD may be used to assess the fractional moving blood volume, as PD image intensity is proportional to the number of scatterers incurring a Doppler shift [34, 85, 86]. Assessment of the fractional moving blood volume is clinically valuable, as changes in local blood volume are correlated with malignancy and therapeutic response [27, 87, 88].

Herein, we propose a modification to the CFPD beamforming technique, termed ppCFPD. We demonstrate that utilizing a non-normalized coherence metric preserves sensitivity toward the underlying blood echo power, while maintaining superior rejection of acoustic clutter and thermal noise in comparison to conventional power Doppler. Furthermore, we derive a theoretical model for thresholding residual incoherent noise incurred by small, partial correlations. The efficacy of these techniques is demonstrated using simulation, phantom, and *in vivo* data.

2.2 Image Formation Techniques

2.2.1 Power Doppler

Power Doppler is a conventional technique for blood flow imaging, depicting the integrated echo amplitude. In comparison to color Doppler, power Doppler offers several clinical advantages, namely being unaffected by aliasing and being relatively independent of insonation angle [34]. Unlike other Doppler methods, power Doppler does not measure blood flow velocity, but instead depicts the relative amount of flow within a pixel, termed the 'fractional moving blood volume' [86].

To isolate the blood signal, a clutter filter is applied to an ensemble of delay-and-sum beamformed RF-data to attenuate slowly moving tissue clutter. The power may then be estimated from the filtered complex data, $r(a)$, over a temporal ensemble of length A.

$$\mathrm{PD} = \sum_{a=1}^{A} |r(a)|^2 \tag{2.1}$$

Additionally, averaging over an axial kernel may be introduced to improve the estimation, as described by Loupas *et al.*[89].

2.2.2 Coherent Flow Power Doppler

Coherent Flow Power Doppler portrays the normalized spatial coherence of the backscattered echo. CFPD adapts the Short Lag Spatial Coherence (SLSC) tissue imaging technique by initially applying a filter to the delayed channel data to suppress the tissue signal. Subsequent calculation of the SLSC metric and summation over a temporal ensemble suppresses spatially incoherent clutter [62].

The SLSC metric is formulated using the normalized spatial coherence measured between two channel signals separated by a given distance, or 'lag'. The normalized coherence, $R(m)$, for a transmit aperture of size N may be written as

$$R(m) = \frac{1}{N-m} \sum_{i=1}^{N-m} \frac{\sum_{n=n_1}^{n_2} y_i(n) y_{i+m}(n)}{\sqrt{\sum_{n=n_1}^{n_2} y_i^2(n) \sum_{n=n_1}^{n_2} y_{i+m}^2(n)}}, \tag{2.2}$$

which is calculated for all pairs of time-delayed, filtered RF channel signals, y_i and y_{i+m}, separated by a given lag, m. To reduce random errors, estimation over a kernel, n, spanning approximately one wavelength is employed. Conventionally, m and N are described in terms of number of elements.

Measurement of the average normalized covariance is repeated for a set of M successive lags, which is used to obtain the SLSC metric,

$$V(a) = \frac{1}{M} \sum_{m=1}^{M} R(m). \tag{2.3}$$

The final CFPD image is reconstructed through computation of the SLSC metric for each pixel, which is squared and summed over a slow-time ensemble of length A, as

$$\text{CFPD} = \sum_{a=1}^{A} V(a)^2. \tag{2.4}$$

2.2.3 Power Preserving Coherent Flow Power Doppler

The proposed approach involves a modest, but impactful, modification to the CFPD beamforming scheme [90]. These adaptations are enacted to preserve the linear relation between pixel intensity and the blood echo power, while maintaining improved suppression of incoherent signals over PD. Omission of the denominator in the calculation for normalized coherence yields the spatial coherence, which may be written

$$\breve{R}(m) = \frac{1}{N-m} \sum_{i=1}^{N-m} \sum_{n=n_1}^{n_2} y_i(n) y_{i+m}(n). \tag{2.5}$$

In this thesis, the term spatial coherence will be used to refer to Equation (2.5), and the term normalized spatial coherence will be used in reference to Equation (2.2). Coherence, also called mutual intensity, can be difficult to interpret in comparison to normalized coherence, as the resultant value is scaled by the relative signal intensities. However, in the context of a backscattered blood or tissue echo, spatial coherence may be theoretically described through an assessment of the van Cittert-Zernike theorem, as described in Section 2.3.1.

Observing the spatial coherence for a given lag, m, allows the underlying signal energy to be conveyed in the intensity of the beamformed image. Averaging the spatial coherence for a defined set of M lags produces

$$\breve{V}(a) = \frac{1}{M}\sum_{m=1}^{M}\breve{R}(m). \tag{2.6}$$

Subsequently, the ppCFPD image is reconstructed by summing over a temporal ensemble, shown in Equation (2.7). Noting the omission of the squaring term used in Equation (2.4), the computation of the spatial coherence shown in Equation (2.7) effectively yields units of amplitude squared. As a result, the amplitude of the ppCFPD image exhibits a power scale equivalent to power Doppler.

$$\text{ppCFPD} = \sum_{a=1}^{A}\breve{V}(a) \tag{2.7}$$

2.3 Theory

2.3.1 Coherence of Signals in the Aperture Domain

The van Cittert-Zernike theorem describes the development of wavefront coherence as a wave propagates away from an incoherent, quasi-monochromatic source [60]. In the context of ultrasound, insonification of an incoherent scattering medium gives rise to a backscattered echo, which is functionally equivalent to the medium acting as an incoherent source. As such, the coherence of the time-delayed echo observed at two channel positions across the aperture takes a predictable form [61]. For a pair of delayed channel signals, $y_1(f)$ and $y_2(f)$ at the focal depth, z, the spatial coherence may be written as

$$\breve{R}(x_1, x_2, z, f) = y_1(f) y_2(f) = \frac{\chi(f)}{z^4} R_o(x_1 - x_2), \tag{2.8}$$

where $\chi(f)$ is the scattering function and R_o is the autocorrelation of the transmit aperture function evaluated as a function of the spatial separation between the channels, $x_1 - x_2$. As described in prior literature, the autocorrelation of a rectangular aperture may be modeled as a triangular function, $\Lambda[\frac{m}{N}]$ [61]. Assuming a rectangular aperture, we may equivalently describe spatial coherence using the relation

$$\breve{R}(m) = \frac{\chi(f)}{z^4} \Lambda[\frac{m}{N}]. \tag{2.9}$$

The scattering function, $\chi(f)$, describes the collective acoustic scattering produced by the scatterers contained in the illuminated media. In a general sense, the scattering intensity and integrated Doppler spectra are linearly proportional to the number of scatterers incurring a Doppler shift [81, 85]; thus, spatial coherence is proportional to the fractional moving blood volume. Comparatively, measures of normalized spatial coherence portray only the transmitter aperture function and omit dependence on the scattering amplitude and depth [61].

2.3.2 The Effect of Noise on Coherence Measures

Acoustic clutter and thermal noise limit the performance of Doppler imaging techniques, particularly for slow flow assessment [53] and deep imaging targets [84]. These incoherent signals, which we refer to as ‘noise’ for brevity, produce a spatial coherence function that may be modeled by a delta function at lag zero [49, 82]. Coherence-based beamformers leverage this characteristic, as tissue and blood signals exhibit higher measures of normalized coherence in the short lag region ($M < 30\%\ N$) [52, 62]. However, normalization imparts a dependency on SNR level, which is a practical drawback for beamforming applications.

This effect can be demonstrated by considering a scenario in which a received echo has been corrupted by noise. To begin, we note that the normalized spatial coherence described in Equation (2.2) is equivalent to the first moment, or mean, of the correlation, $\rho_{y_1y_2}$, measured between two channel signals.

If we consider the noise signal, n, to be uncorrelated from the signal of interest, s, the correlation measured between the two channel signals may be written

$$\rho_{y_1y_2} = \frac{\mathbb{E}[(s_1+n_1)(s_2+n_2)]}{\sqrt{\mathbb{E}[s_1^2+n_1^2] \quad \mathbb{E}[s_2^2+n_2^2]}}, \tag{2.10}$$

where the symbol $\mathbb{E}[\cdot]$ denotes the expectation operator.

Assuming a rectangular receive aperture and that the respective signal powers associated with any two elements on the array are approximately equal, we can describe the correlation coefficient as

$$\rho_{y_1y_2} = \frac{P_s(1-\frac{m}{N})}{P_s+P_n} = \frac{1-\frac{m}{N}}{1+\frac{P_n}{P_s}}, \tag{2.11}$$

where P_s represents the underlying blood signal power and P_n denotes noise power [82]. Thus, the normalized coherence observed between two signals retains a dependence on the signal SNR.

In comparison, we may perform an analogous derivation for the spatial coherence posed in Equation (2.5). We note that this spatial coherence expression is equivalent to the first moment of the covariance, $\sigma_{y_1y_2}$. Using the same assumptions as before, we obtain

$$\sigma_{y_1y_2} = \mathbb{E}[(s_1+n_1)(s_2+n_2)] = P_s(1-\frac{m}{N}) + P_n\delta(0). \tag{2.12}$$

As described in prior literature, the spatial coherence function of incoherent noise signals can be approximated as a delta function at lag zero, which is excluded from the summation in Equation (2.6) [49]. Therefore, we may theoretically conclude that the ppCFPD pixel intensity scales linearly with the power of the received blood echo, and is independent of additive noise for non-zero lags, as performed in Equation (2.6).

2.4 Robust Noise Thresholding

Despite a favorable theoretical assessment, a small amount of uncorrelated noise will persist at non-zero lags due to random partial correlations [82]. The residual noise signal is often low amplitude; however, remaining noise may misguide assessment of flow, particularly in SNR-limited environments.

Further, a consequence of employing a measure of coherence in the ppCFPD beamforming scheme is the potential for negative pixel values to be produced. Negative pixel values confound image quality metrics and need to be addressed for standard log compression. Prior literature in related areas have associated negative pixel values with partial correlations incurred by clutter, and thus have enforced thresholding to set all negative pixel values to zero [91, 92].

We propose a statistically-driven threshold to adaptively suppress residual additive noise and simultaneously justify eliminating the negative signals generated by incoherent backscattered signals. The additive noise is modeled as a statistically independent process from the blood signal. Therefore, the threshold may be defined through an exercise where we presume that the channel data contain only noise.

2.4.1 An Expression of ppCFPD Pixel Intensity for Noise Signals

We begin by writing an equivalent statement of the ppCFPD pixel intensity, shown in Equation (2.7), for the particular scenario in which the channel data contain only noise. We model this noise signal as an independent, normally distributed random variable with constant variance, distributed identically across all elements. The ppCFPD coherence measure described in Equation (2.5) may be written in terms of the normalized correlation coefficient, $\rho_{y_i y_{i+m}}$, through the relationship

$$\breve{R}(m) = \frac{1}{N-m} \sum_{i-1}^{N-m} \rho_{y_i y_{i+m}} \sqrt{\sum_{n=n_1}^{n_2} y_i^2(n) \sum_{n=n_1}^{n_2} y_{i+m}^2(n)}. \tag{2.13}$$

Due to the assumption of constant variance, this equation may be simplified by noting that the noise variance can be equivalently written as

$$\sigma_{noise}^2 = \sqrt{\frac{1}{H} \sum_{n=n_1}^{n_2} y_i^2(n) \frac{1}{H} \sum_{n=n_1}^{n_2} y_{i+m}^2(n)}, \tag{2.14}$$

where H indicates the axial kernel size. Thus we may further simplify Equation (2.13) to

$$\breve{R}(m) = \frac{H\sigma_{noise}^2}{N-m} \sum_{i-1}^{N-m} \rho_{y_i y_{i+m}}. \tag{2.15}$$

Modeling $\rho_{y_i y_{i+m}}$ as an ergodic random variable, we may extend this derivation to Equations (2.6) and (2.7), to obtain an expression of ppCFPD pixel intensity as

$$\text{ppCFPD} = AH\sigma_{noise}^2 \frac{1}{M} \sum_{m=1}^{M} \frac{1}{N-m} \sum_{i=1}^{N-m} \rho_{y_i y_{i+m}}. \tag{2.16}$$

2.4.2 Modeling Gaussian Statistics of ppCFPD Pixel Intensity for Noise Signals

Next, we consider the statistical character of the correlation measured between channel signals, $\rho_{y_i y_{i+m}}$, and subsequently, the statistical character of ppCFPD pixel intensity. For a Gaussian noise signal, the expected value of the correlation coefficient is zero. In application, estimation of the sample correlation using finite signal lengths will incur non-zero correlation measures, *i.e.* non-zero variance.

The exact distribution of the sample correlation measured between two normal variables is rather arduous, so we employ an approximation as follows [93]. For small correlations, we note the Fisher transform is approximately an identity function, such that the value of $\rho(m)$ is approximately equal to its related Z-score, $z(m)$. The correlation coefficient may be transformed to the Z-space via the Fisher Transform,

$$z(m) = \frac{1}{2}\ln\frac{1+\rho(m)}{1-\rho(m)} = \text{arctanh}(\rho(m)). \tag{2.17}$$

For the derivation of ppCFPD pixel intensity statistics, we will approximate the distribution of the correlation coefficient using its correspondent Z-score statistical distribution, which is approximately normally distributed, $(z \sim N(0, \sigma_z))$, with calculable standard deviation

$$\sigma_z = \frac{1}{\sqrt{H-3}}. \tag{2.18}$$

Modeling $\rho(m)$ as a normally distributed random variable allows us to generalize the statistical character of ppCFPD pixel intensity via properties of location-scale family probability distributions, which we briefly discuss in Appendix A. Thus, we find that the pixel intensity for noise signals is normally distributed with a mean and variance described as

$$\begin{aligned} \mu_{\text{pixel}} &= AH\sigma^2_{\text{noise}}\,\mu_z \approx 0 \\ \sigma^2_{\text{pixel}} &= A(\frac{1}{M}H\sigma^2_{\text{noise}}\,\sigma_z)^2 \sum_{m=1}^{M}\frac{1}{N-m}. \end{aligned} \tag{2.19}$$

Additionally, it may be noted that the summation term may be expressed via generalized harmonic numbers, as

$$\sum_{m=1}^{M}\frac{1}{N-m} = \mathcal{H}_{\text{N-1}} - \mathcal{H}_{\text{N-M-1}}, \tag{2.20}$$

such that a closed form approximation can be obtained using the truncated series form

$$\mathcal{H}_{\text{a}} - \mathcal{H}_{\text{b}} = \ln(\frac{\text{a}}{\text{b}}) + \frac{\text{a}^{-1}-\text{b}^{-1}}{2} - \frac{\text{a}^{-2}-\text{b}^{-2}}{12}. \tag{2.21}$$

This derivation is further described in Appendix B.

2.4.3 Approximation of Noise Variance

In practice, it is necessary to estimate the noise variance, σ^2_{noise}, as depicted in Equation (2.14). Reasserting our assumption that the noise signal is zero-mean, the noise variance is equal to the noise power $\left(\mathbb{E}[(x-\mu)^2] = \mathbb{E}[x^2]\right)$. As described in prior literature [82, 94], we can obtain an expression for noise power in terms of the SNR, as

$$\sigma^2_{noise} \equiv P_n = \frac{P_{s+n}}{\text{SNR } + 1}, \tag{2.22}$$

where the SNR can be estimated via a lag-one autocorrelation technique described by Long *et al.*[95].

2.4.4 Definition of a Threshold

Once we obtain an estimate of the ppCFPD pixel variance for the noise signal as shown in Equation (2.19), we can derive a threshold to suppress residual noise. Here, we will define the threshold as the upper bound of the 95% statistical interval of noise signal intensity. For a given pixel, x, this may be written

$$f(x) = \begin{cases} x, & \text{if } x \geq 1.96\, \sigma_{pixel}, \\ 0, & \text{otherwise.} \end{cases} \tag{2.23}$$

We note that the method of setting negative pixel values to zero used by other investigators is equivalent to defining the threshold as the upper bound of the 50% statistical interval of pixel intensity [44, 91, 92].

Comparatively, PD and CFPD pixel intensity is biased by noise. A supplementary derivation of pixel intensity for PD is presented in Appendix C. For channel data containing only noise, we observe PD pixel intensity is approximately Gamma distributed with mean and variance described as

$$\begin{aligned} \mu_{\text{pixel}} &= AN\sigma^2_{\text{noise}} \\ \sigma^2_{\text{pixel}} &= 2A(N\sigma^2_{\text{noise}})^2. \end{aligned} \tag{2.24}$$

2.5 Methods

2.5.1 Simulated Data Acquisition

Simulations were performed using Field II to study the performance of ppCFPD under varied noise conditions [96, 97]. The simulated phantom included a single blood vessel with a 5 mm diameter, embedded in a 9 cm by 5 cm homogeneous tissue block at a 45° angle relative to the transducer. The blood signal was simulated using scatterers moving in a laminar flow state. The velocity distribution was parabolic [98], with a maximum velocity of 5 cm/sec. This models the range of velocities observed in capillary (<1 mm/sec),

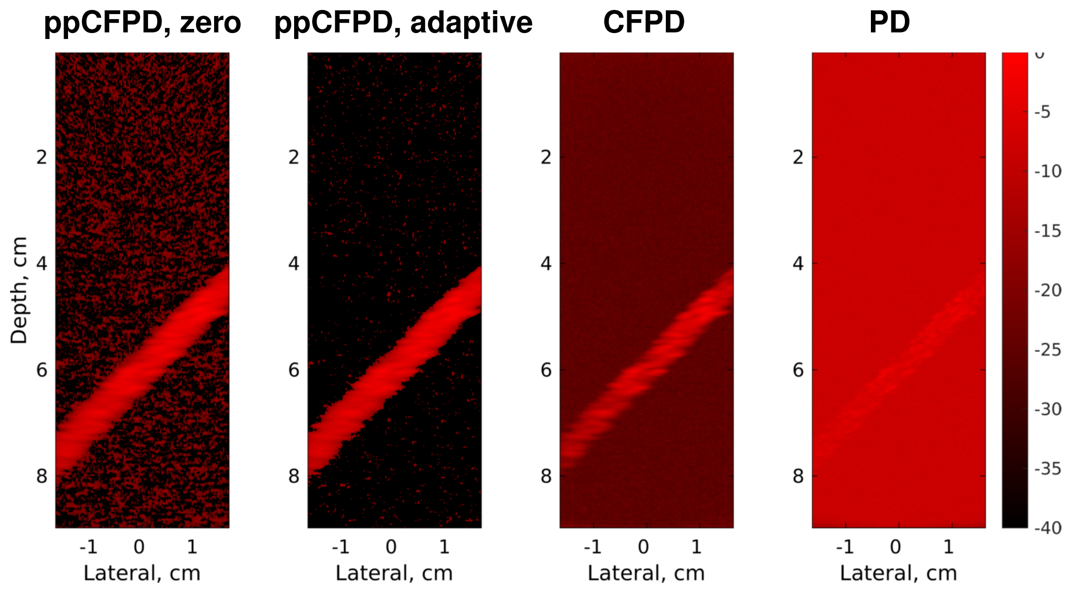

Figure 2.1: Comparison of image formation techniques. For ppCFPD, application of the theoretical threshold (ppCFPD, adaptive) suppressed the noise floor more effectively than thresholding negative values (ppCFPD, zero). Note that the dynamic range is extended so that the noise floor is visible in all cases. Images depict a 100% fractional moving blood volume realization with -10dB blood channel SNR.

arteriole (<1 cm/sec), and small arteries [53, 98].

Channel data for the blood scatterers and tissue scatterers were simulated separately, then combined into a single channel data set. The blood channel data were scaled -60 dB relative to the surrounding tissue. Normally distributed white noise was added to the channel data to simulate thermal noise [82]. The noise was scaled between 20 to -20 dB relative to the power of the blood channel data. No temporal motion was simulated.

The simulated acquisitions were performed using a 128-element linear array transducer with a center frequency of 3 MHz and pitch of 0.257 mm. For each acquisition, plane waves between -4° and 4° spaced by 1° were simulated at a pulse repetition frequency (PRF) of 9 kHz. The channel data were delayed using Plane Wave Synthetic Focusing (PWSF), in which the delayed channel data acquired at consecutive angles were summed to produce a final pulse repetition frequency of 1 kHz [99]. PWSF achieves a uniform focusing throughout the image and maintains consistent coherence measures [82]. A 10 Hz IIR filter cutoff was used for temporal clutter suppression, chosen empirically to provide filter stability and rejection of the tissue signal.

Matched PD, CFPD, and ppCFPD images were generated as shown in Figure 2.1. For ppCFPD and CFPD processing, a maximum lag (M) of 20 was used to correspond with prior literature [45]. A kernel size (H) equal to one wavelength was employed, to reconcile the trade-off between jitter and loss of spatial resolution [33]. Images were formed using an ensemble of 50 frames, and displayed on a $10\log_{10}(\cdot)$ dB scale.

2.5.2 Perception of Fractional Moving Blood Volume

The assertion that ppCFPD image intensity is linearly proportional to the blood echo power was evaluated via a successive dilution study, emulating a prior PD assessment by Rubin *et al.*[86]. As described in subsection 2.5.1, the blood channel data was obtained independently from the tissue channel data using Field II. The blood scatterers were separated into two groups: a stationary subset and a moving subset. The fractional moving

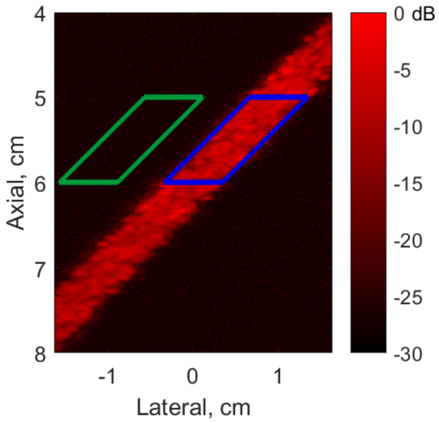

Figure 2.2: Signal (blue) and background (green) ROIs for image quality metrics.

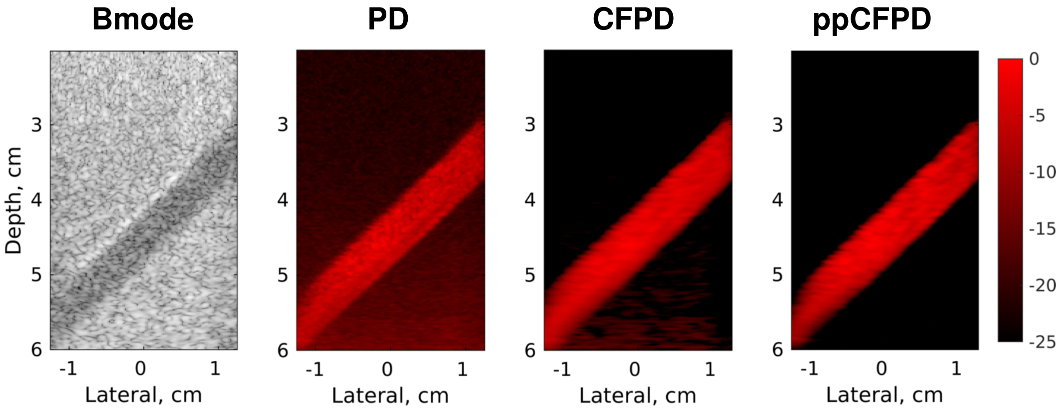

Figure 2.3: Phantom study images. Figure depicts a 100% fractional moving blood volume realization with 5 cm/s flow, obtained at 11 V. Bmode image shown on a 60 dB scale.

blood volume was modified by incrementally changing the ratio of moving-to-stationary blood scatterers. This was done to fix the acoustic scattering strength of the blood scatterers across fractional levels and produce equivalent scaling for a given SNR. The stationary blood scatterers are rejected during processing, so the observed blood signal power decreases proportionally with the fractional moving blood volume, in agreement with prior literature [85, 86]. The fraction of moving blood scatterers was iteratively decreased from 100% (all moving) to 1% (nearly all stationary). Five independent simulations of blood and tissue were generated for each fractional step. In addition, additive thermal noise was added to the channel data containing blood and tissue to assess discrimination of fractional moving blood volume at five blood channel SNR levels.

The average blood pixel intensity was measured within a defined region of interest for each non-log compressed image, as shown in Figure 2.2. For each fractional step, the mean and standard deviation of the average intensity was measured across the five independent simulations to generate curves. The curves were normalized to the highest mean value for each noise case, in accordance with the technique by Rubin *et al.*[86]. The theoretical thresholding was not applied when estimating the fractional moving blood volume. However, negative pixels were excluded from the calculation of mean and standard deviation, since negative pixels are produced by out-of-phase noise signals [92].

2.5.3 Image Quality Metrics

Conventional image quality metrics, including contrast and CNR, were calculated as shown in Equations (2.25) and (2.26). Negative pixels were not considered when calculating image quality metrics. This approach is consistent with similar coherence algorithms used in prior literature, which set negative pixels to zero [44, 91, 92].

We calculated image quality using

$$\text{Contrast} = 10\log_{10}\left(\frac{\bar{S}_i}{\bar{S}_o}\right) \tag{2.25}$$

$$\text{CNR} = \frac{|\bar{S}_i - \bar{S}_o|}{\sqrt{\sigma_i^2 + \sigma_o^2}} \tag{2.26}$$

where S_i indicates the signal within the vessel ROI, and S_o indicates the signal within the background ROI, as shown in Figure 2.2. The standard deviation of the pixel values is represented by σ. The mean signal value is denoted by an overbar symbol. The theoretical thresholding was not applied when calculating metrics.

We acknowledge that the image quality metrics measured across PD, CFPD, and ppCFPD may not be entirely comparable; these algorithms depict fundamentally different quantities (echo intensity and spatial coherence, respectively), so conventional metrics may not equally impute the ability to discriminate structures with a similar intensity level. For instance, squaring the SLSC metric in the summation of Equation (2.4) extends the dynamic range of CFPD, which improves measures of contrast, but does not necessarily improve feature detection. Recently, Rodriguez-Morales *et al.*proposed an alternative image quality metric termed the generalized contrast-to-noise ratio (GCNR) [100]. The GCNR metric depicts the likelihood of discriminating a signal of interest as an expression of probability density function overlap, which is invariant to changes in dynamic-range. For completeness, we include an assessment of image quality in terms of the GCNR, measured

$$GCNR = 1 - OVL, \tag{2.27}$$

where OVL is the overlap between the intensity distribution of the background and the intensity distribution of the blood signal. This formulation implies that GCNR = 1 if there is complete discrimination of the blood signal, and GCNR = 0 if the distributions completely overlap. To compute the GCNR, histograms with 1,000 equally spaced bins were generated for the data within the signal and noise ROIs, respectively. The fraction of pixels contained in overlapping bins was measured as OVL. The GCNR was measured at each fractional moving blood volume increment, for blood channel SNR levels between -20 and 20 dB.

2.5.4 Assessment of Theoretical Bound for Noise Thresholding

For algorithm validation, the theoretical noise threshold was applied to the simulation and phantom data produced in subsections 2.5.1 and 2.5.5. The noise power was estimated using the lag-one spatial coherence described by Long *et al.*[95]. For the Field II simulations, a single estimate of pixel variance was obtained as shown in Equation 2.19, using the average of the noise power estimates for σ^2_{noise}. Values below the theoretical threshold were set to zero prior to log compression.

For the phantom data, local estimates of pixel variance were obtained to accommodate depth-dependent attenuation. Noise variance, as shown in Equation 2.12, was computed for each pixel via lag-one spatial coherence, using a kernel matching the SLSC axial kernel.

2.5.5 Phantom Data Acquisition

A wall-less vessel phantom study was conducted for further validation. An aqueous solution of 6% (mass %) polyvinyl-alcohol (PVA) with a molecular weight of 89,000 (Sigma-Aldrich, St. Louis, MO) was heated to 85° C and stirred until fully dissolved. To form a scattering medium, graphite powder was added to the solution at a 6% mass concentration

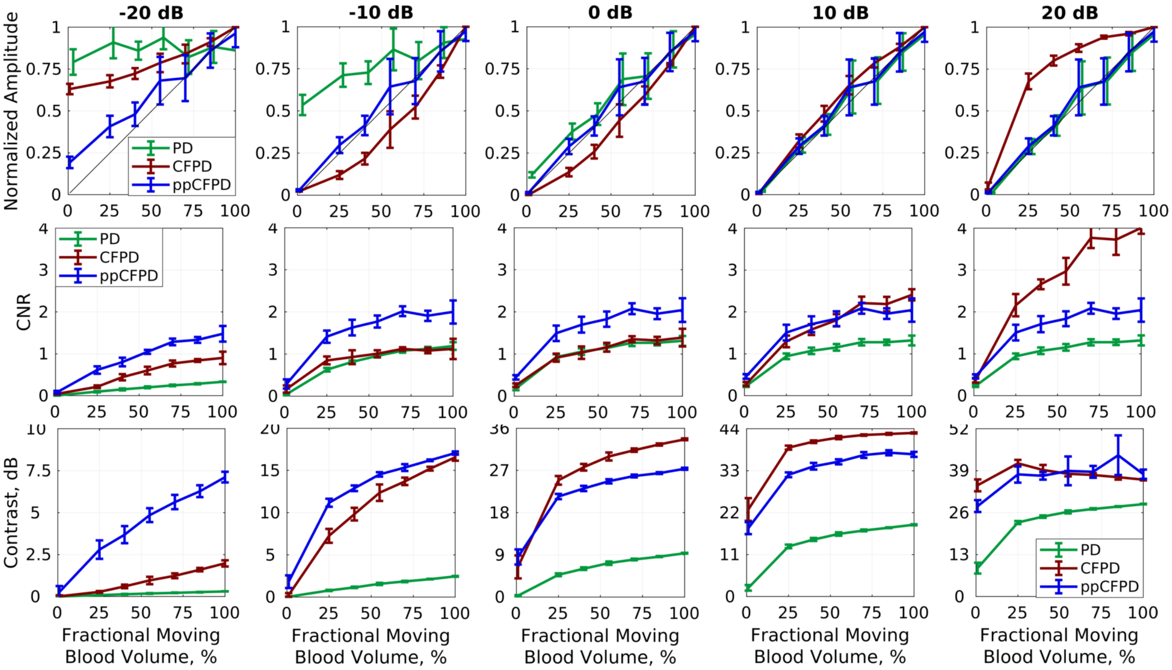

Figure 2.4: Plots depict the mean and standard deviation of image quality metrics measured across simulation realizations.
Top Row: The ppCFPD blood signal amplitude remains a linear approximation of the fractional moving blood volume despite variation in the blood channel signal-to-noise ratio (SNR) from -20 dB to 20 dB. This may be observed in the figure, as the ppCFPD curve closely approximates the theoretical value, shown in black. *Center Row:* The CNR of ppCFPD remained nearly constant across noise levels indicating effective suppression of the noise floor relative to the blood signal. *Bottom Row:* For all noise cases, ppCFPD and CFPD offered greater contrast than conventional PD.

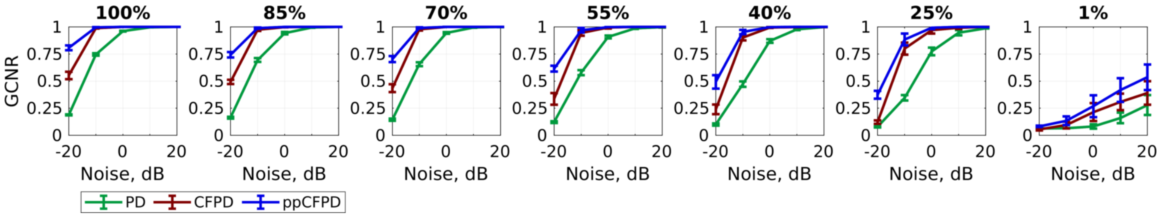

Figure 2.5: Each plot depicts the GCNR metric as a function of the blood channel signal-to-noise ratio, for incrementally decreasing fractional blood volume levels. The fractional moving blood volume ranged from 100% (*left*), indicating full flow, to 1% (*right*), indicating nearly no flow. The ppCFPD images produced a higher GCNR for blood flow at all levels of flow, indicating greater discrimination capability in comparison to PD and CFPD.

[101]. Once the solution reached room temperature, the PVA/graphite solution was poured into a mold made of a 12 oz disposable paper cup. Prior to adding a PVA/graphite solution, a 6.35 mm (1/4 in) diameter glass rod was inserted to form a single 45 degree vessel. The phantom was stored in a freezer at -20°C for 16 hours, then thawed at room temperature for 8 hours to complete one freeze-thaw cycle. Three freeze-thaw cycles were completed to increase phantom stiffness and preserve the vessel structure upon removal of the glass rod.

An aqueous cornstarch solution served as a blood-mimicking fluid. The concentration of cornstarch was varied to emulate fractional changes in the proportion of blood scatterers. The base solution contained contained 3% (mass %) cornstarch [62], which corresponded to the 100% relative concentration. The base solution was diluted to obtain 85, 70, 55, 40,

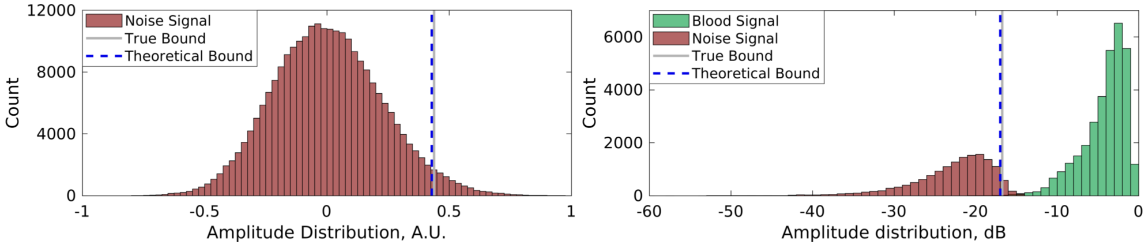

Figure 2.6: *Left:* Distribution of pixel intensity for channel data containing only noise. The theoretical threshold is an effective approximation of the 95% confidence interval, compared to the empirically measured value. *Right:* The confidence interval remained a robust approximation of noise pixel variance for simulations additionally containing blood. Data shown depicts a 100% fractional moving blood volume realization with -10dB SNR.

25, 10 and 0% relative concentrations. To ensure the concentration remained constant, the solution was placed in a beaker and continuously stirred. A continuous-flow pump (Cole-Parmer, Vernon Hills, IL) was used to circulate the solution through the vessel at velocities of 3 and 5 cm/s (95 and 57 ml/min). Proximal to the phantom, the blood mimicking fluid was passed through a pulse dampener to obtain a laminar flow profile.

The phantom study was conducted using a Verasonics Vantage system (Verasonics, Inc., Kirkland, WA) and an L12-5 linear array probe with a 5.43 MHz center frequency. Channel data were acquired from nine angled plane wave transmits spanning from -4° to 4°, spaced by 1°. The channel data acquired at the nine angles were compounded to achieve synthetic aperture focusing, resulting in a final PRF of 1 KHz. Data were acquired at 11, 16, and 21 Volts to obtain varied SNR. For each voltage, the SNR was estimated from the RF data using the temporal lag-one correlation [94]. A 50 Hz IIR filter was used to suppress tissue clutter. The PD, CFPD, and ppCFPD images were formed using matched ensembles of 50 frames, as shown in Figure 2.3. For ppCFPD and CFPD processing, a maximum lag (M) of 20 and a kernel size (H) equal to one wavelength was employed.

2.5.6 *In vivo* Data Acquisition

An *in vivo* liver imaging case was obtained from a healthy adult male subject in compliance with Vanderbilt's Institutional Review Board (IRB) protocol. The study was conducted using a Verasonics Vantage system (Verasonics, Inc., Kirkland, WA) and a C5-2 curvilinear array probe with a 4.16 MHz center frequency. Channel data were acquired at 21 V from nine angled unfocused transmits spanning from -4° to 4°, spaced by 1°. The steered transmit delays were calculated as $t = \frac{r\phi \sin\theta}{c}$, where r is the probe radius, ϕ is the elemental angle span, θ is the steering angle, and c is the speed of sound. The channel data were coherently compounded to achieve synthetic aperture focusing, producing a final PRF of 600 Hz.

An adaptive demodulation scheme was applied to the channel data to reduce motion

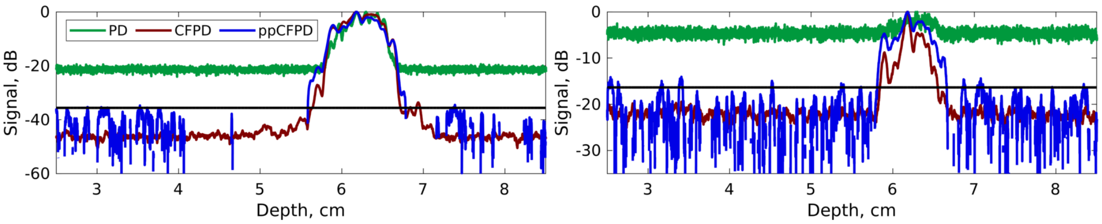

Figure 2.7: Axial cross sections of simulation data for 10dB channel SNR (*left*) and -10dB channel SNR (*right*) cases. Realization shown depicts a 100% fractional moving blood volume case. The black line depicts the theoretical threshold.

incurred by the patient and sonographer, using a kernel size of 10 λ and a lag of 1 frame [76, 79]. A 120 Hz IIR filter was applied to suppress tissue clutter. For ppCFPD and CFPD processing, a maximum lag (M) of 20 and a kernel size (H) equal to one wavelength was employed. The theoretical threshold was applied. The images were formed using 50 frame ensembles.

2.6 Results

2.6.1 Fractional Moving Blood Volume

Figure 2.4 depicts plots of PD, CFPD, and ppCFPD image intensity as a function of the fractional moving blood volume for five simulated SNR levels. CFPD produces a non-

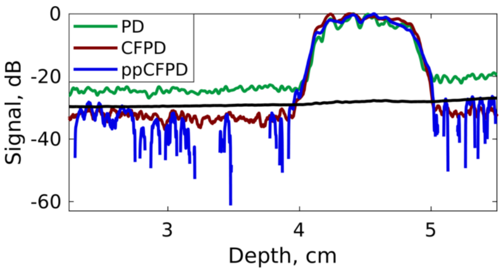

Figure 2.8: Axial cross section of phantom ppCFPD data (blue) depicting the theoretical threshold (black) obtained using local estimates.

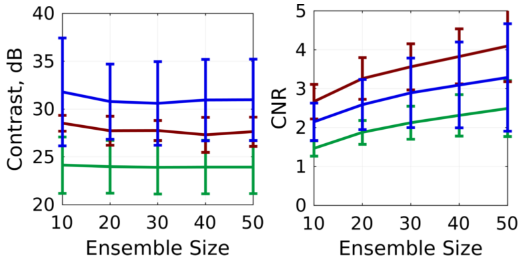

Figure 2.9: Contrast and CNR for varied ensemble lengths. Phantom data shown corresponds to the 5cm/s flow rate and 21 V acquisition.

linear response with respect to echo magnitude, whereas the ppCFPD image response is linear. The observed variability of CFPD is a result of normalization, which imparts a dependence on SNR, as CFPD image intensity is proportional to $\left(\frac{1-m/N}{1+P_n/P_s}\right)^2$. This relationship results in a concave or convex function of intensity, depending on the SNR.

As observed in prior literature, PD is an effective linear estimator of the fractional moving blood volume in good imaging conditions [34]. However, this relationship is compromised in SNR-limited environments, as noise overwhelms the PD signal. In comparison, ppCFPD is robust to varied SNR and remains proportional to the fractional moving blood volume. The greater capability of ppCFPD to accurately estimate relative concentrations of blood flow in SNR-limited environments is attributed to greater suppression of incoherent noise, which extends the dynamic range and improves sensitivity toward low-amplitude features.

2.6.2 Image Quality

Figures 2.4 and 2.5 depict image quality measures for ppCFPD, CFPD, and PD obtained at seven blood volume concentrations and five levels of SNR. In matched simulations, ppCFPD yielded marked image quality improvement over PD, exhibiting contrast improvements up to 26.24 dB and a CNR gain of 1.38.

In Figure 2.4, we observe that measures of contrast and CNR for CFPD exceed those of ppCFPD in several cases. This illustrates the dependence of CFPD image quality on SNR. At 20dB SNR, CFPD demonstrates a substantial CNR gain in comparison to lower SNR levels. This behavior is similar to SLSC performance, where the CNR value has been shown to peak at a specific SNR depending on intrinsic contrast of the medium [82, 102]. In comparison, CNR performance of ppCFPD is fairly flat, indicating that it is robust to noise.

It is worth noting that we observed low intensity side lobes in both CFPD and ppCFPD under conditions of low channel noise, which has also been observed in previous literature

[62, 91]. These side lobe artifacts are due to out-of-phase correlations produced by off-axis signals. The squaring term in CFPD transforms these negative correlation values to positive pixel intensities; as a result, CFPD exhibits a slight reduction in contrast at high SNR levels due to the presence of these side lobes [62]. In ppCFPD image formation, negative values are removed, so these side lobes do not degrade image quality metrics. The squaring operation in CFPD additionally decreases the GCNR of CFPD in SNR-limited environments, as a greater proportion of the noise pixel intensity may overlap with low, positive blood pixel values.

2.6.3 Theoretical Thresholding

Initial simulations demonstrate feasibility in using the theoretical threshold for robust noise suppression. For a case of channel data containing only noise, the assumption that the statistical distribution of the correlation coefficient is equivalent to the distribution of the Z-score appears to hold. Extension of this model to ppCFPD pixel intensity appears to remain valid in simulation, as depicted in Figures 2.6 and 2.7. Figure 2.7 depicts an axial cross section for simulations with 10 dB and -10 dB channel SNR. Both ppCFPD and CFPD demonstrate greater dynamic ranges as a result of improved noise suppression. The theoretical threshold remains effective at both SNR levels.

Both ppCFPD and CFPD beamforming improve discrimination of the blood signal from background noise in comparison to PD. Application of the theoretical threshold further improves this delineation, shown in single vessel simulations in Figure 2.1.

The presence of side lobes in the high SNR cases did skew the distribution of ppCFPD pixel intensity toward negative values, which violates the assumption of Gaussian distributed noise. As a result, we observed underestimation of the theoretical noise threshold for simulations with high SNR. However, in these conditions, the blood is readily observed without thresholding.

Preliminary efficacy of the theoretical threshold was also observed in phantom data.

Figure 2.8 shows an axial cross section of the phantom with locally-derived threshold estimates. The theoretical threshold can be applied to effectively suppress the noise floor in the ppCFPD images.

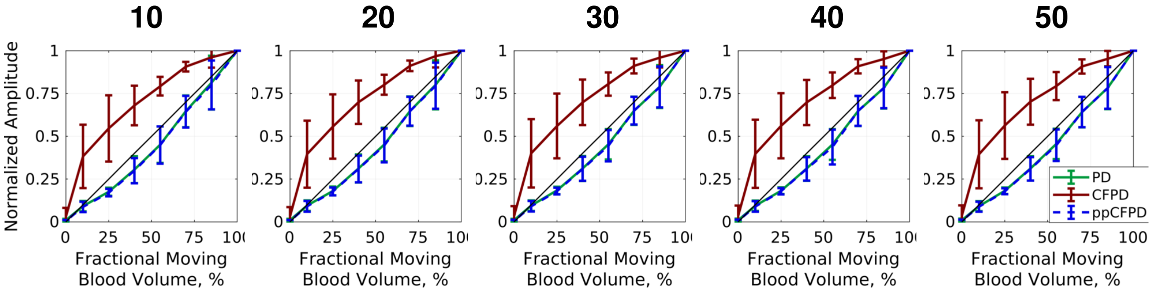

Figure 2.10: Fractional moving blood volume plots for ensemble lengths between 10 (*left*) and 50 (*right*) frames. The phantom data shown correspond to 5 cm/s flow obtained at 21 Volts.

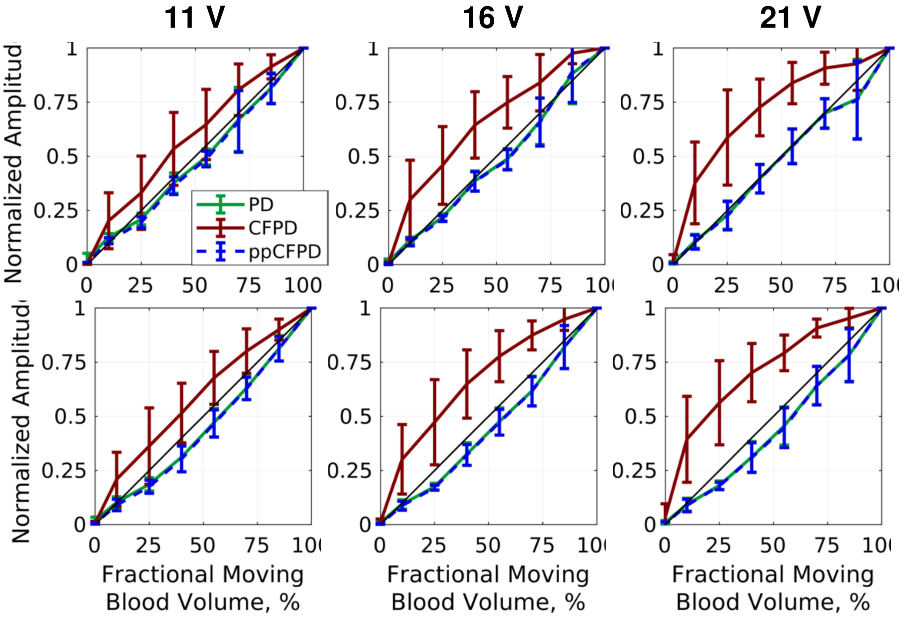

Figure 2.11: Fractional moving blood volume plots for phantom data obtained at 11, 16, and 21 V for 3 cm/s (*top*) and 5 cm/s (*bottom*) blood flow velocities.

2.6.4 Phantom Study

Overall, ppCFPD offered greater noise suppression than PD, resulting in image quality improvements of up to 13.42 dB in contrast and 2.1757 for CNR. Figure 2.12 depicts image quality metrics for the 5 cm/s case across voltages. Varying the acquisition voltage between

11, 16, and 21 Volts produced varied SNR levels of 28.14 ± 3.67 dB, 31.16 ± 3.66 dB, and 33.31 ± 3.68 dB, respectively.

Figures 2.9 and 2.10 depict results for ensemble lengths ranging from 10 to 50 frames. As shown in Fig. 2.10, ppCFPD remains an effective estimator of the fractional moving blood volume for short ensemble lengths, which is necessary for most clinical systems.

Figures 2.11 and 2.12 demonstrate that ppCFPD image performance was consistent across the varied voltage levels, indicating that ppCFPD is robust to varied SNR. In comparison, the CFPD image performance exhibits a non-linear relationship toward the fractional moving blood volume.

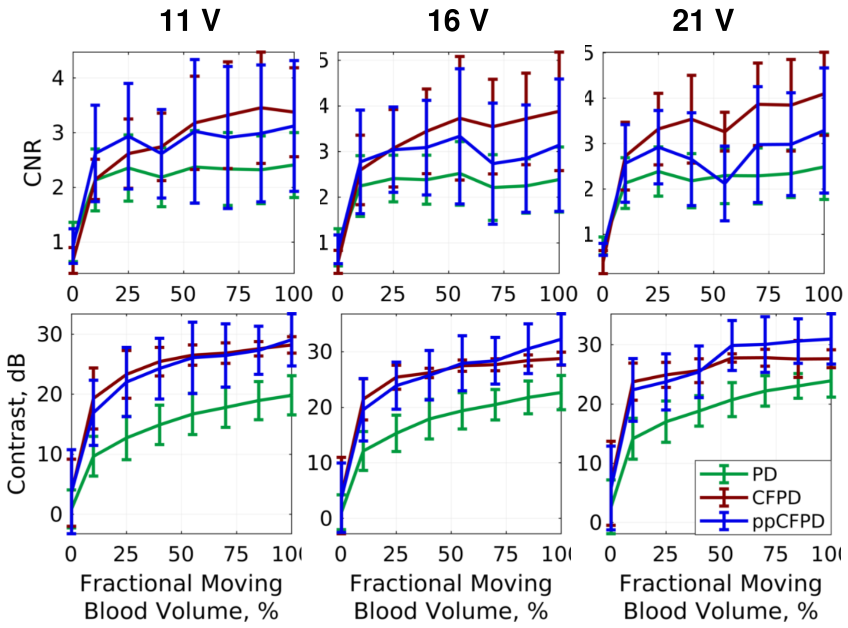

Figure 2.12: CNR and Contrast plots for phantom data obtained at 11, 16, and 21 V. Mean and standard deviation of metrics shown for the 5 cm/s velocity realizations.

A small amount of clutter is visible in the deeper region of the ppCFPD image of Figure 2.3; however, the clutter signal is likely tissue signal that was not suppressed by the wall filter. The application of motion compensation techniques [79] and advanced clutter filters [56] would improve suppression of residual tissue signals.

2.6.5 *In vivo* Case

PD, CFPD, and ppCFPD images of a healthy liver were produced to demonstrate preliminary *in vivo* efficacy, as shown in Figure 2.13. The *in vivo* case had a beamformed SNR of 33.14 dB.

The CFPD and ppCFPD images have a greater dynamic range than the PD image, resulting in greater discrimination of low amplitude vasculature. As shown with *in vivo* data, limiting the PD display dynamic range improves contrast, but results in the loss of low intensity image features.

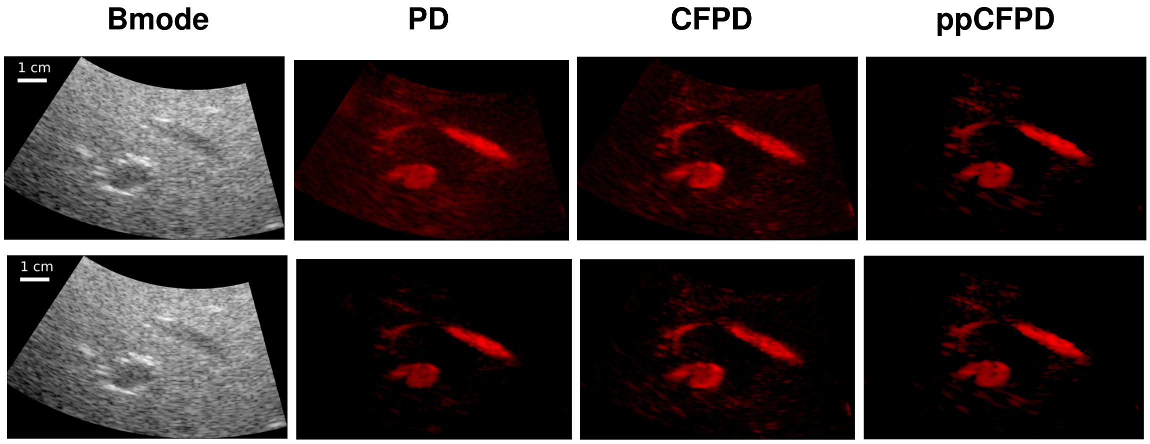

Figure 2.13: Preliminary images of liver blood flow to demonstrate *in vivo* feasibility. Bmode images shown on a 60 dB scale.
Top Row: PD, CFPD, and ppCFPD images displayed on a 27 dB scale. Images produced via the ppCFPD algorithm effectively delineated small vessels, which are nearly indistinguishable from the noise floor in the PD case.
Bottom Row: The dynamic range is scaled to just above the perceptible noise floor for each image. The dynamic range is 21 dB for PD, 25 dB for CFPD, and 27 dB for ppCFPD. Decreasing the dynamic range compromises the visibility of low-intensity vasculature in PD relative to ppCFPD and CFPD.

2.7 Discussion and Conclusions

This paper presents an adapted coherence-based beamforming technique based on a measure of spatial coherence, rather than normalized spatial coherence, to mitigate incoherent clutter signals while preserving the backscattered echo intensity. In addition, a theoretical threshold was derived to rigorously justify the suppression of negative pixel values and small positive pixels associated with clutter signals, and to facilitate improved perception of vasculature.

The performance of ppCFPD was robust to varied ensemble lengths, SNR levels, and blood flow velocities. The coherence metric used in ppCFPD is not normalized; therefore, ppCFPD images portray the mutual intensity of the channel signals. As shown in simulation and phantom data, the resultant ppCFPD image intensity scales linearly with the underlying echo magnitude. This means that the ppCFPD image intensity portrays the fractional moving blood volume, which may be clinically valuable for *in vivo* assessment of local changes in perfusion. In comparison, CFPD employs a normalized measure of coherence, which results in varied performance depending on the SNR.

The ppCFPD technique produced higher image quality over PD, which is ascribed to improved suppression of thermal noise and incoherent clutter. Subsequently, ppCFPD images exhibit a greater dynamic range than PD images, which enables low intensity blood vessels to be more readily observed.

The simulation and phantom experiments assessed ppCFPD performance for varied conditions of white thermal noise. We anticipate that other forms of spatially incoherent clutter, such as reverberation, will be suppressed in accordance with our theoretical derivation, though not directly studied here. However, other forms of image degradation, such as phase aberration, may reduce overall coherence measures [49]. In the presence of these factors, spatial coherence would be decreased and the ppCFPD pixel intensity would likely be degraded, though PD would suffer as well.

We note that coherence-based beamformers can be used in conjunction with other advanced tissue clutter suppression techniques. In this paper, an adaptive demodulation technique proposed by Tierney *et al.*was used to compensate for tissue motion *in vivo* [79]. Advanced filtering techniques would likely further improve suppression of residual tissue, which is not inherently mitigated in coherence-based beamforming. Filtering is necessary because tissue signals are coherent in the aperture domain. We expect that the combination of coherence beamforming and advanced clutter filters will yield superior sensitivity toward blood flow.

As described for similar coherence-based beamforming approaches, computational cost remains a practical drawback of this technique. The ppCFPD beamforming scheme has a substantially larger computational burden in comparison to power Doppler due to the necessity to perform coherence estimates of channel data signals. We anticipate that a software beamforming implementation would make a real-time implementation of ppCFPD feasible, using approaches developed by others [83].

An unresolved challenge for coherence imaging in general is the presence of so-called 'dark-region artifacts' [103, 104]. These artifacts occur when regions adjacent to bright targets exhibit reduced coherence measures due to high amplitude off-axis scattering. In the context of blood flow imaging, out-of-phase or negative correlation measures produce the appearance of negative pixel values. Since measures of signal power and PD are inherently positive valued, the consensus in prior investigations has been to set these values to zero [44, 91]. We hypothesize that the development of advanced filters may reduce the amplitude of acoustic clutter, which can produce dark-region artifacts and reduce visualization of adjacent, low-amplitude blood flow.

Overall, this approach shows promise for improving discrimination of blood flow within cluttered environments. Both CFPD and ppCFPD offer improved image quality over PD; however, we demonstrated that the CFPD technique exhibited non-linear characteristics as a function of varied SNR. In comparison, ppCFPD was robust to thermal noise power and retained sensitivity to relative variations in fractional moving blood volume. This preliminary study suggests that a mutual intensity metric may be a valuable approach to assess blood flow gradation in cluttered imaging environments.

Chapter 3

Multidimensional Clutter Filtering of Aperture Domain Data

This work has been reprinted, with permission, from [105] K. A. Ozgun and B. C. Byram, “Multidimensional clutter filtering of aperture domain data for improved blood flow sensitivity,” *IEEE Transactions on Ultrasonics, Ferroelectrics,and Frequency Control*, 2021. © 2021 IEEE.

3.1 Introduction

PD imaging is a preferred ultrasonic technique for visualization of low velocity blood flow. When coupled with plane wave synthetic focusing (PWSF), Doppler data can be accumulated at high frame rates with improved sensitivity toward microvasculature [99], [37]. This has enabled visualization of low velocity blood flow without contrast enhancement, which is clinically valuable for functional and therapeutic assessment [37], [27].

However, the sensitivity of power Doppler imaging is inherently tied to the signal-to-clutter ratio (SCR) and the filter rejection band [37]. These constraints particularly impede microvasculature imaging, as low velocity blood echoes are often close to the noise floor [44, 106] and can exhibit similar slow-time characteristics to tissue [44], [106]. For non-contrast PD, these challenges have been primarily addressed through novel beamforming [62, 73, 91, 107], clutter rejection [56, 57, 65, 108–111], and post-processing strategies [43, 106].

Clutter rejection filtering is used to suppress undesirable noise and “clutter” signals, which arise from reverberation, off-axis scattering, and non-stationary tissue echoes [111], [53]. Historically, clutter rejection algorithms have used infinite impulse response, finite impulse response, and regression filters, which have been extensively studied and optimized [54, 55, 112, 113]. These filters are effective when the blood and clutter signals reside in orthogonal Fourier or polynomial basis vectors; however, this assumption can be violated in imaging conditions with patient and sonographer motion, as well as in conditions with strong electronic white noise [111], [53]. Frequently, clutter rejection filters are coupled with motion correction techniques to reduce the mean frequency and bandwidth of the clutter signal [55], [79].

More recently, singular value decomposition (SVD) filters have emerged as a robust alternative to conventional filters. The motivation for using SVD filters is two-fold. First, SVD filtering is inherently adaptive, as the SVD basis set is defined by the covariance characteristics of the data. In addition, SVD filters can operate on 1-D (temporal) or 2-D (spatial and temporal) data, which expands the feature space for signal classification. As a result, SVD filtering can achieve superior performance over conventional methods [109], [57, 65, 111]. However, SVD filter utility suffers when blood, clutter, and noise are not distributed over orthogonal bases. Complex tissue motions and factorization rank limitations can cause signal overlap, which imposes a trade-off between clutter rejection and preservation of the blood signal [106], [110]. Accordingly, SVD filtering improves with longer ensemble sizes [57], [65], but this is not feasible on clinical scanners which rely on short ensemble lengths (typically <50 frames) to achieve reasonable real-time Doppler frame rates [114], [115].

HOSVD filtering has been proposed to improve the SCR while preserving sensitivity toward microvasculature. The application of HOSVD was first proposed by Kim *et al.*, who demonstrated efficacy in filtering a 3-D tensor of multi-rate radiofrequency data [116], [68]. This method has been termed multi-rate because it employs two temporal dimensions: the pulse dimension, which is sampled on the slow time interval at the pulse repetition frequency, and the Doppler frame dimension, which constitutes a set of pulses. Expanding the dimensionality of the data expands the feature space, which enables better separability of the blood signal. To date, research on clutter rejection filtering has been limited to temporal and spatial extents. However, advancements in PD beamforming have primarily focused on leveraging features of delayed channel data and sub-aperture data [56, 57, 65, 108–111].

With the exception of limited research [71], [117], these features have remained broadly unstudied for clutter filtering. In this paper, we present a novel filtering methodology that uses a higher-order SVD applied to a 3-D tensor of aperture data, with spatial, slow-time, and channel dimensions. To demonstrate feasibility of the approach, these methods are applied to simulated and *in vivo* liver data.

3.2 Theory

3.2.1 Doppler Data

In conventional power Doppler processing, filtering is applied to beamformed radiofrequency data, which is composed of Z axial samples, X lateral samples, and A slow-time frames. To perform singular value decomposition, the beamformed data is often reshaped into Casorati form, combining the axial and lateral spatial dimensions to yield the 2-D matrix $X \in \mathbb{C}^{K \times A}$, where $K \equiv XZ$ [57]. We propose using the higher-order SVD to filter aperture data. 'Aperture data' refers to the delayed channel data after synthetic transmit focusing, prior to the beam sum. This data is composed of Z axial samples, X lateral samples, A slow-time frames, and N channels. Combining the spatial samples in a Casorati form, the aperture data is represented as a 3-D matrix, $\mathcal{X} \in \mathbb{C}^{K \times A \times N}$.

3.2.2 Singular Value Decomposition

Conventionally, the singular value decomposition (SVD) of the beamformed data matrix $X \in \mathbb{C}^{K \times A}$ is given by

$$X = USV' \tag{3.1}$$

where unitary matrices $U \in \mathbb{C}^{K \times K}$ and $V \in \mathbb{C}^{A \times A}$ contain the spatial and temporal singular vectors, respectively. The matrix, $S \in \mathbb{R}^{K \times A}$, contains the corresponding singular values along the diagonal.

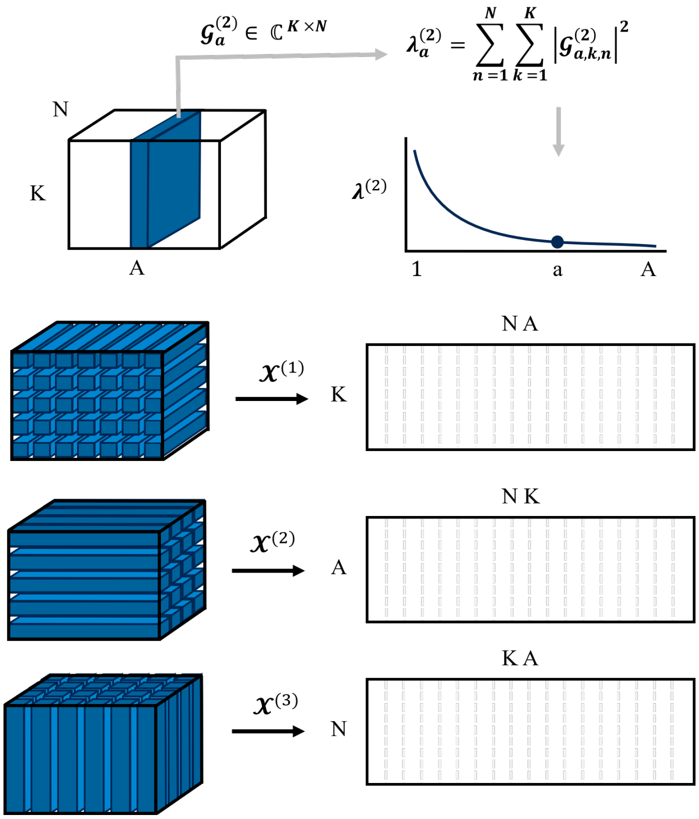

Figure 3.1: *Top:* Computation of the mode-2 eigenvalues from the HOSVD core tensor, $\mathcal{G}$. *Bottom:* Mode-n unfoldings of the data tensor, $\mathcal{X}$, used to compute eigenvectors

3.2.3 Higher-Order Singular Value Decomposition

The higher order singular value decomposition (HOSVD) is a generalization of the SVD and a special case of the Tucker decomposition [118]. The HOSVD of the 3-D aperture data tensor $\mathcal{X} \in \mathbb{C}^{K \times A \times N}$ is given by

$$\mathcal{X} = \mathcal{G} \times_1 U \times_2 V \times_3 W \tag{3.2}$$

where $\times_n$ indicates the mode-n product [118]. The mode-n product, $\mathcal{G} \times_n U$, is equivalent to the multiplication of the matrix and the mode-n unfolding of the tensor, *e.g.* $U\mathcal{G}_{(n)}$. The unfolded matrix, denoted by the subscript $\mathcal{X}_{(n)}$, is the 2-D matrix representation of the data formed by fixing one dimension and combining the other dimensions, as depicted in

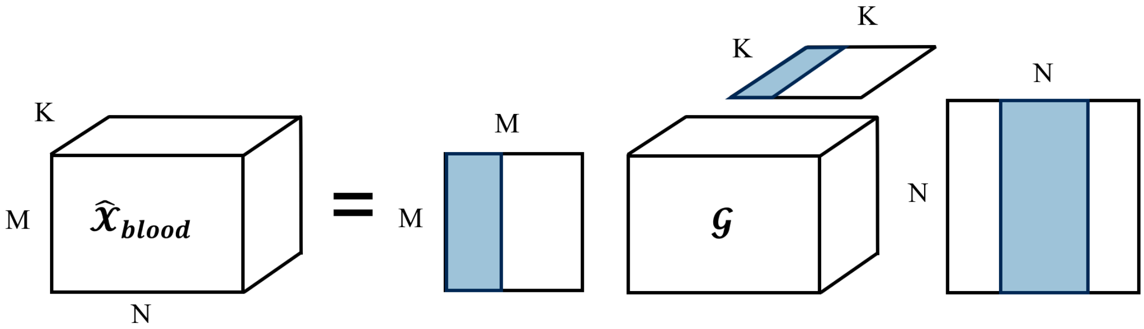

Figure 3.2: The HOSVD of the data tensor, $\mathcal{X}$, yields the core tensor $\mathcal{G}$ and three eigenvector matrices corresponding to temporal, spatial, and aperture dimensions.

Figure 3.1 [119].

As shown in Figure 3.2, HOSVD yields a core tensor, $\mathcal{G} \in \mathbb{C}^{K \times A \times N}$ and three unitary matrices: the spatial singular vectors, $U \in \mathbb{C}^{K \times K}$); the temporal singular vectors, $V \in \mathbb{C}^{A \times A}$); and the channel singular vectors, $W \in \mathbb{C}^{N \times N}$). In practice, the singular vector matrices are computed from the mode-n unfoldings of $\mathcal{X}$. The unfolded matrix is used to produce a covariance matrix, R, from which the singular vector matrix is obtained through eigendecomposition.

$$R_K = \mathcal{X}_{(1)}\mathcal{X}_{(1)}^T = U\Lambda_K U^T \tag{3.3}$$

$$R_A = \mathcal{X}_{(2)}\mathcal{X}_{(2)}^T = V\Lambda_A V^T \tag{3.4}$$

$$R_N = \mathcal{X}_{(3)}\mathcal{X}_{(3)}^T = W\Lambda_N W^T \tag{3.5}$$

The set of mode-n singular values, $\lambda^{(n)}$, are computed as the Frobenius norms of the core tensor, $\mathcal{G}$. This can be written as

$$\lambda_k^{(1)} = \sum_{a=1}^{A}\sum_{n=1}^{N} |g_{k,a,n}|^2 \tag{3.6}$$

$$\lambda_a^{(2)} = \sum_{k=1}^{K}\sum_{n=1}^{N} |g_{k,a,n}|^2 \tag{3.7}$$

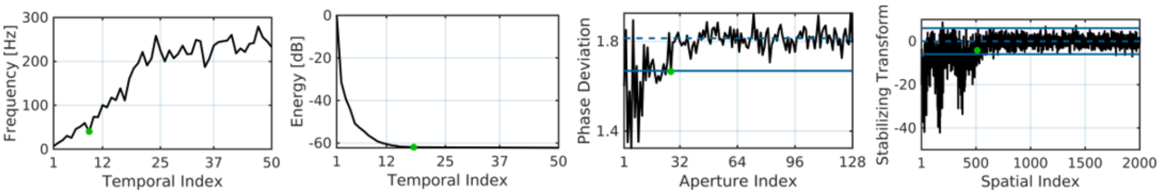

Figure 3.3: *Left to Right:* The features used for HOSVD cutoff selection (green marker) includes temporal singular vector mean frequency, temporal singular value magnitude, aperture singular vector phase deviation, and spatial singular vector amplitude.

$$\lambda_n^{(3)} = \sum_{k=1}^{K} \sum_{a=1}^{A} |g_{k,a,n}|^2 \tag{3.8}$$

3.3 Filter Design

HOSVD and SVD filtering involve a similar process, characterized by (1) decomposition of the Doppler data, (2) classification of the dominant signal type contained in each orthogonal component, and (3) rejection of the components corresponding to clutter and noise. We define the HOSVD filter rejection band using four cutoffs, $\{ c_{t1}, c_{t2}, c_a, c_s \}$, obtained using the following classification scheme. The features used to determine the cutoffs are shown in Figure 3.3.

3.3.1 Temporal domain classification

Two cutoffs are defined in the temporal domain. The lower cutoff is used to reject clutter, which typically exhibits a large magnitude and low mean Doppler frequency. The upper cutoff is defined to reject noise, which typically is clustered in the final singular values. As shown in Fig. 3.4, the spectral content of the temporal singular vectors is nearly symmetric across the positive and negative frequencies. For each singular vector, the mean frequency was estimated from the power spectral density [109], [57]. The lower cutoff, c_{t1}, is chosen to be the point where the mean singular vector frequency exceeds a specified cutoff frequency. The cutoff frequency is selected to reject components that contain the

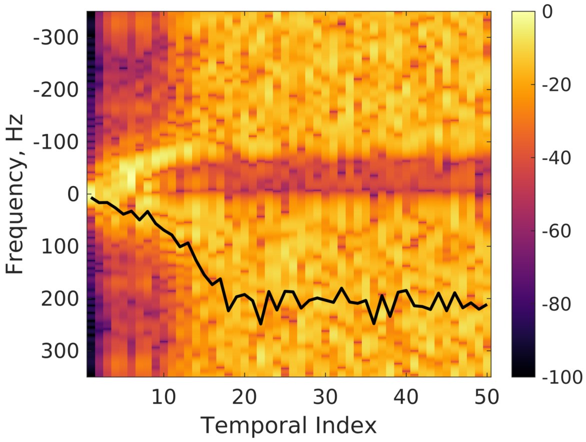

Figure 3.4: Power spectral density of temporal singular vectors. The black line indicates the weighted mean frequency.

clutter signal. The frequency distribution and quantity of clutter-bearing components is influenced by imaging conditions, such as the presence of motion and the clutter-to-blood ratio [56].

For noise rejection, the upper cutoff is determined in two steps, as presented by Song *et al.*[65]. First, a pre-cutoff is defined by fitting the Doppler frequencies to a sigmoid function to find the noise transition point. Second, a linear fit is applied to the singular values after the pre-cutoff point, as the singular value magnitude of noise is expected to follow the Marčenko–Pastur distribution [65], [120]. The upper cutoff, c_{t2}, is chosen as the point where the singular values deviate from this line.

3.3.2 Aperture domain classification

Several aperture domain features have been leveraged by adaptive beamformers, including coherence [52], [121], frequency [122], and phase disparity [80]. Further, a limited number of aperture domain SVD studies have demonstrated that singular value magnitude [71] and singular vector frequency [117] can be used for classification. Here, we propose a single cutoff that uses the phase characteristics of the complex singular vectors. As described by Camacho *et al.*, the phase disparity across the aperture may be used to discriminate between echoes from the focal zone and echoes from other locations [80]. Synthetic aperture focusing achieves uniform focusing over the entire field-of-view, such that on-axis signals are phase aligned, exhibiting low deviation. In comparison, off-axis clutter signals and additive white noise will produce high measures of deviation. Specifically, the phase of additive white noise can be modelled as a uniform distribution between $-\pi$ and π, with a standard deviation of $\frac{\pi}{\sqrt{3}}$. Therefore, we computed the standard deviation of the phase for each aperture domain singular vector. The aperture cutoff, c_a, is determined by finding the point where the standard deviation of the phase plateaus to $\frac{\pi}{\sqrt{3}}$.

In application, a confidence interval for the spatial cutoff was determined empirically. The standard deviation was measured from 100,000 realizations of uniformly distributed random values of length N. The 2.5 and 97.5 percentiles were used to compute a 95% confidence interval. If the measured phase exceeded the upper confidence interval bound, the signal likely crossed the $-\pi$ to π phase boundary, so auxiliary phases were computed, as done by Camacho *et al.*[80]. The aperture cutoff, c_a, was defined as the last point where the measured phase fell below the lower confidence interval bound.

3.3.3 Spatial domain classification

In the spatial domain, we leverage the amplitude characteristics of the singular vectors. Singular vectors containing noise can be modeled as zero-mean complex Gaussian signals, $N(0, \sigma^2)$. The amplitude component of these singular vectors is therefore characterized by the Nakagami distribution with shape and scale parameters of $m = 1$ and $w = 2\sigma^2$.

The Nakagami shape parameter, m, has been used to characterize envelope statistics of backscattered echoes, as the Nakagami distribution encompasses pre-Rayleigh (m<1), Rayleigh (m=1) and Rician (m>1) statistics [123, 124]. The inverse normalized variance estimator (INV) is a common technique for estimating the Nakagami shape parameter [125],

[126]. The INV estimator is $\sqrt{N}$-consistent and asymptotically unbiased, defined as

$$\hat{m}_{INV} = \frac{(E[A^2])^2}{E[A^4] - E[A^2])^2} \tag{3.9}$$

As a result, we can define a stabilizing transform which converges to a zero-mean Gaussian random variable,

$$s = \sqrt{N}(\hat{m}_{INV} - m) \rightarrow N(0, \sigma^2_{INV}) \tag{3.10}$$

with an asymptotic variance of

$$\sigma^2_{INV} = 2m(m+1). \tag{3.11}$$

The stabilizing transform parameter, s, is be computed for every spatial singular vector. Finally, the spatial cutoff, c_s, is defined as the point where s falls within $\pm 3\sigma^2_{INV}$. In practice, a 5-point moving average was first applied to the stabilizing transform parameter, to reduce spurious outliers.

3.3.4 Clutter Rejection and Power Estimation

Filtering is performed by reducing or zeroing the clutter-dominant components. Therefore, we define the blood core tensor, $\hat{\mathcal{G}}$, as

$$\hat{g}_{k,a,n} = \begin{cases} 0, & \text{for } c_s \leq k \leq K \\ 0, & \text{for } c_a \leq a \leq A \\ 0, & \text{for } n \leq c_{t1} \text{ and } n \geq c_{t2} \\ g_{k,a,n}, & \text{otherwise.} \end{cases} \tag{3.12}$$

and filtered dataset as

$$\hat{\mathcal{X}} = \hat{\mathcal{G}} \times_1 U \times_2 V \times_3 W \tag{3.13}$$

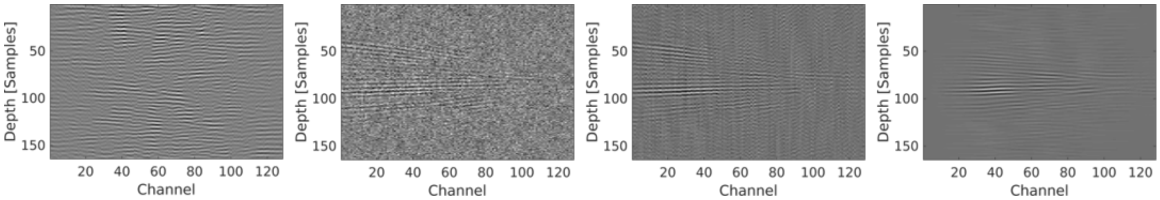

Figure 3.5: Examples of delayed channel data with various levels of clutter rejection filtering. *Left to Right:* (1) Unfiltered data, (2)temporal filtering only, (3) temporal and spatial filtering, (4) temporal, spatial, and aperture filtering.

Finally, the beamsum and power estimation are performed, yielding the power Doppler image, P_{HOSVD}. Fig. 3.5 depicts an example of the benefit of multidimensional clutter rejection, showing that the greatest detection of the on-axis blood flow signal is achieved using temporal, spatial, and aperture domain cutoffs.

3.4 Methods

Processing and analysis were performed in Matlab (version R2018b, MathWorks, Natick, MA). Beamforming was implemented using the UltraSound ToolBox (v2.1) [127]. The TensorLab (v3.0) function mlsvd was used for HOSVD [128]. All power Doppler images are shown on a dynamic range normalized to the maximum intensity of the image.

3.4.1 Performance Metrics

We compare the HOSVD filter to (1) a conventional SVD filter applied to the radiofrequency data, and (2) a novel SVD filter applied to the mode-3 unfolding (*e.g.* frames × space*channels) of the aperture data. 'Gold standard' power Doppler images were formed using these methods, denoted P_{SVD} and P_{SVD-a}, respectively.

The blood flow detection performance was assessed using a receiver operating characteristic curve (ROC) analysis, similar to Chee et. al [129]. ROC curves were generated by plotting the true positive rate against the false positive rate, measured over a set of thresholds. The true positive rate was defined as the fraction of blood pixels that exceeded the threshold value, and the false positive rate was defined as the fraction of tissue pixels that exceeded the threshold value. The thresholds were post-filter Doppler power values, swept between the minimum and maximum Doppler power in 0.2 dB increments. The area under the ROC curve (AUC) was used to quantify how well the blood flow was distinguished from the background. Further, the image quality was measured in terms of the contrast, defined as

$$Contrast = 10 * \log 10\left(\frac{\bar{P}_{blood}}{\bar{P}_{background}}\right) \tag{3.14}$$

and the CNR,

$$\mathrm{CNR} = 10 * \log 10\left(\frac{\bar{P}_{blood} - \bar{P}_{background}}{\sigma_{background}}\right). \tag{3.15}$$

3.4.2 Simulation Design

A simulation study was conducted using Field II [96, 97]. A 2 x 3 cm tissue phantom was designed with a 0.4 mm vessel angled 60° relative to the probe. Blood scatterers were perfused in a parabolic velocity profile, with a peak velocity of 10 mm/s.

To simulate realistic clutter, bulk motion was applied to the tissue and blood scatterers. Five independent motion profiles were obtained by averaging 2D displacement estimates [31] from tissue mimicking phantoms. The five tissue phantoms were composed of a PVA-graphite mixture [73] and acquired using an L12-4 probe held freely by a sonographer. The phantom acquisition was performed using probe parameters similar to the simulation (f_0 = 7.813 MHz, f_s = 31.24 MHz) and the same plane wave acquisition sequence.

Five independent simulation realizations were generated using the five motion profiles. For each simulation, the tissue and blood channel data were simulated separately, and normally distributed random noise was used to simulate electronic noise. The data were combined using a -40 dB blood-to-tissue ratio and a -45 dB noise-to-tissue ratio. Five phantoms were generated for independent speckle and displacement realizations. A sample B-mode is shown in Figure 3.6.

A linear probe was modelled using the parameters shown in Table 3.1. Channel data was acquired using an ultrafast plane wave sequence composed of 13 plane waves evenly spaced between $-2.7°$ and $2.7°$. Plane wave synthetic focusing was applied to achieve uniform focusing [99], yielding a net PRF of 700 Hz. Power Doppler images were formed from a 4 x 13 mm patch (164 x 64 samples) of simulated data.

3.4.3 Simulation Experimental Set Up

3.4.3.1 Optimal Performance

To assess the optimal performance of the filter, a set of power Doppler images were formed by manually defining the HOSVD cutoffs in a bounded grid search over the ranges depicted in Table 3.2. Since the optimal contrast, CNR, and AUC may correspond to unique cutoff choices, each performance metric was optimized separately. The reference SVD filters were manually tuned over the c_{t1} and c_{t2} ranges. Ensembles of 50 frames were used.

Table 3.1: Field II Simulation Parameters

Parameter	**Value**
f_0	7.813 MHz
Bandwidth	65%
f_s	78.13 MHz
Element Number	128
Element Width	0.1703 mm
Element Pitch	0.1953 mm
Sound Speed	1540 m/s

Table 3.2: Optimal Performance Study Cutoff Ranges

Parameter	**Min**	**Max**	**Increment**
c_{t1}	1	K-1	2
c_{t2}	c_{t1}+1	K	2
c_a	8	64	8
c_s	400	1900	300

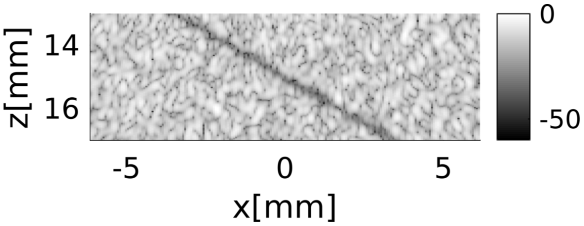

Figure 3.6: Sample B-mode of simulated vessel phantom shown on a 60dB scale.

3.4.4 Classifier Performance

Classifier performance was assessed by comparing the results of the manually-tuned study to power Doppler images formed using the HOSVD cutoffs obtained using the classifier described in Section III.

The spatial and aperture domain cutoffs were determined using the theoretical cutoff points, *e.g.* when the phase deviation plateaued at $\frac{\pi}{\sqrt{3}}$ and when the stabilizing transform parameter plateaued at $\pm 3\sigma_{INV}^2$. The lower temporal cutoff, defined as a cutoff frequency, was the only bound that needed to be parameterized. The temporal cutoff frequency was tuned between 2 to 100 Hz, in 2 Hz increments. Ensembles of 50 frames were used.

3.4.5 Short Ensemble Performance

To assess the value of using HOSVD filtering for power Doppler imaging using relatively short ensembles, images were additionally formed using ensembles of 16 and 25 frames. The same classifier parameterization was used, however, the temporal cutoff frequency was tuned between 2 to 200 Hz, in 2 Hz increments. The extended frequency range was used as shorter ensembles result in temporal singular vectors with more broadband frequency content, which increases the mean frequency.

3.4.6 *In vivo* Study

Efficacy was further demonstrated *in vivo* using a small pilot study of liver imaging data acquired from a healthy adult male subject. Five datasets were obtained in compliance with Vanderbilt's Institutional Review Board (IRB) protocol. Channel data was acquired using a C5-2 probe on a Verasonics research system (Verasonics Inc., Kirkland, WA), with a sequence composed of nine angled plane wave transmits evenly spaced from -4° to 4°. The pulse was designed with a f_0 of 4.167 MHz and f_s of 16.68 MHz. Plane wave synthetic focusing was applied, yielding a net PRF of 600 Hz.

3.4.7 Image Quality

Power Doppler images were formed using ensembles of 50 frames. Since global processing was used, depth-dependent effects such as attenuation and gain may confound accurate estimation of the Nakagami parameters [123] . To overcome this constraint, the power of each singular vector amplitude was normalized through depth when computing the stabilizing transform parameter. For each dataset, a single region of 1299 axial samples and 64 lateral samples was processed. The temporal cutoff frequency was tuned between 2 and 200 Hz, in 2 Hz increments. Image quality was measured in terms of contrast and CNR using manually-segmented regions of interest, as shown in Figure 3.7. To assess the sensitivity of each filter toward the temporal cutoff frequency, the robustness was measured in terms of contrast loss relative to the highest achievable contrast for each dataset. This was measured as $1 - \frac{|Contrast - Contrast_{max}|}{Contrast_{max}}$, using the non-log compressed contrast values.

3.4.8 Computational Complexity

The computational cost of HOSVD filtering is more demanding than conventional SVD filtering. The HOSVD and SVD-a filters are both applied to delayed channel data, which inherently increases the memory demand by the size of the channel count in comparison to

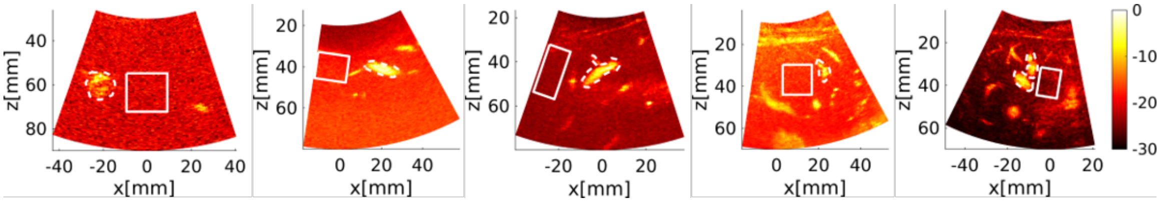

Figure 3.7: Blood (dashed) and background (solid) regions of interest used for human *in vivo* performance assessment. Power Doppler images formed using a conventional SVD filter are shown on a 30dB scale.

conventional SVD filtering, which is applied to beamformed radiofrequency data.

The computational complexity of SVD is often approximated as $O(ka^2)$ for a matrix with dimensions k>a. As a tensor method, the computational complexity of HOSVD is greater, although truncated methods and efficient approximation methods have been developed. The HOSVD of a three-dimensional tensor with dimensions [n,k,a] involves three separate SVDs to obtain the singular vector matrices. We estimate that HOSVD would therefore be associated with a baseline computational complexity of roughly $[O(kan^2) + O(nak^2) + O(nka^2)]$. However, the absolute computational throughput would depend on various factors, including the processing system, available memory, and decomposition algorithm. The time expense of the different decomposition methods was evaluated using the five *in vivo* datasets with varied parameterization. We measured the total serial run time to perform each decomposition in MATLAB (The Mathworks Inc., Natick, MA, USA) on a desktop computer running dual Intel Xeon E5-3643 v4 CPUs at 3.40GHz with 6 cores each. The computation time across each run was measured using the built-in MATLAB tic and toc commands.

For benchmarking, transmit beamforming was applied to each *in vivo* dataset, yielding a tensor with dimensions [K×A×N] corresponding to spatial samples, channels, and frames. The HOSVD computation time was recorded as the time to decompose the full tensor. We assessed the time to perform a standard HOSVD using the function mlsvd. The SVD-a computation time was recorded as the time to perform an SVD on the unfolded matrix with dimensions of [KA×N]. Finally, the conventional SVD computation time was measured

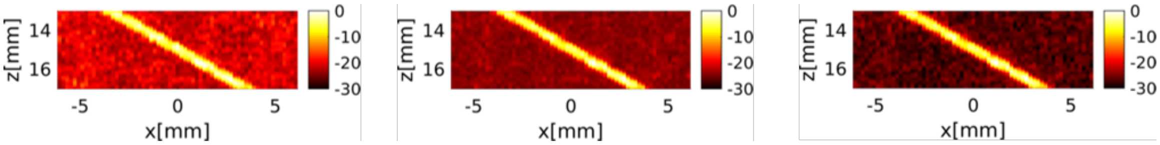

Figure 3.8: Sample power Doppler images obtained using SVD, SVD-a, and HOSVD. Images correspond to the results from the classifier-generated cutoff study that produced the highest contrast for a single simulation case.

as the time to perform an SVD on the beamformed matrix with dimensions of [K×N], obtained by summing over the tensor's channel dimension.

To assess the effects of varied parameterization, we demonstrate the relative effects of (1) changing the temporal ensemble length between 10 and 50 frames and (2) processing a spatial sample containing between 100 and 500 depth samples. For all cases, 128 channels and 64 lateral samples were used. Plots were formed to depict the effect of varying each parameter, while holding the other parameter constant at 50 frames or 500 pixels, respectively.

3.5 Results and Discussion

3.5.1 Simulation study

The HOSVD clutter filter demonstrated improved performance over the SVD filters in simulation, as depicted in Figure 3.8. Result metrics are reported using the mean ± one standard deviation over the five simulated phantoms.

3.5.2 Optimal Performance

HOSVD outperformed conventional SVD filtering in an ideal setting, as depicted in Figure 3.9 and Figure 3.10. Using the optimized set of manually-tuned cutoffs for each filter, HOSVD produced a maximum contrast of 19.99 ± 1.97 dB, compared to SVD (14.48 ± 3.13 dB) and SVD-a (19.54 ± 2.21 dB). Similarly, HOSVD produced a higher maximum

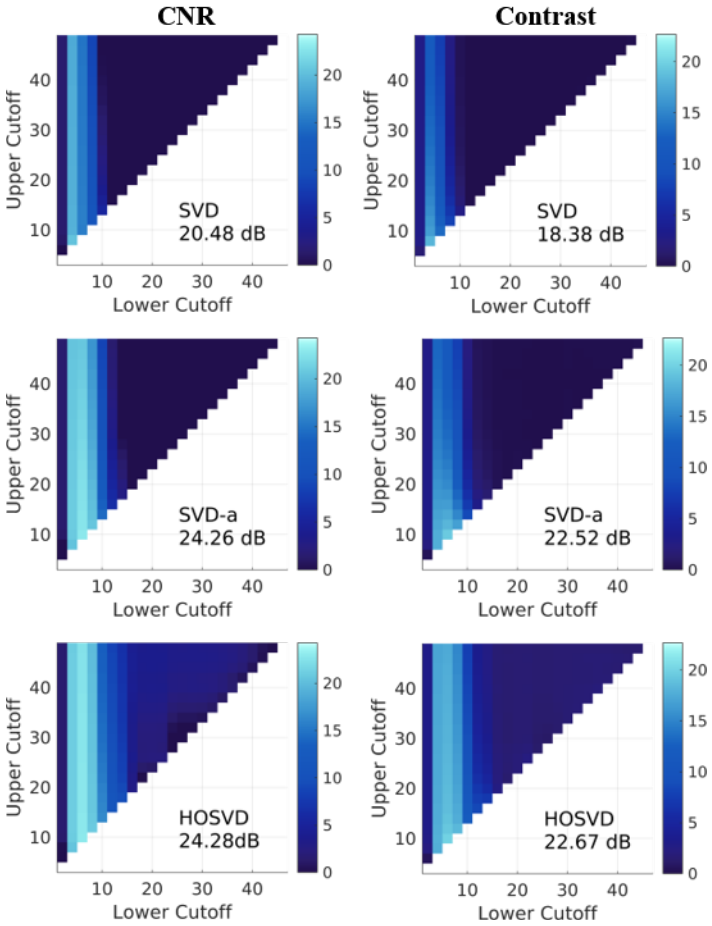

Figure 3.9: Depiction of the optimal performance study grid search. CNR (*left*) and Contrast (*right*) results shown on a dB scale for P_{SVD} (*top*), $P_{\text{SVD}-a}$(*middle*), and P_{HOSVD} (*bottom*) as a function of the lower and upper temporal cutoffs. The HOSVD results depict the highest values obtained over the spatial and aperture ranges. The highest achieved image quality for each method shown in bottom corner.

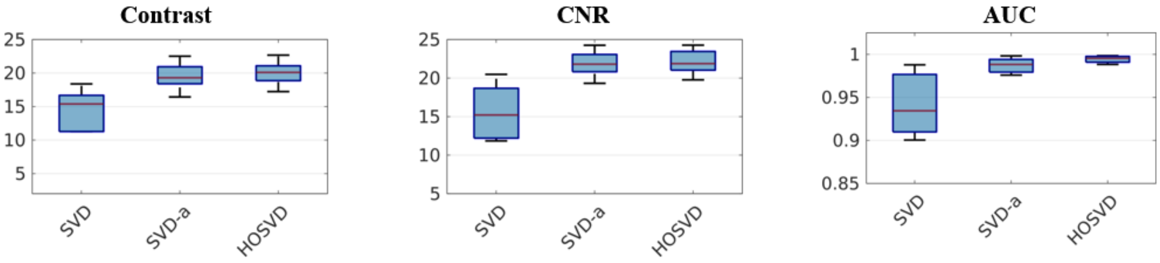

Figure 3.10: Simulation results for the optimal performance study. Contrast and CNR are shown on a dB scale.

CNR (22.11 ± 1.72 dB versus 15.59 ± 3.7 dB for SVD and 21.88 ± 1.81 dB for SVD-a).

However, an additional key benefit of HOSVD is that it is more robust in non-ideal conditions than SVD or SVD-a. Fig. 3.9 depicts contrast and CNR results across all temporal cutoffs for a single simulated dataset. Similar to the findings of Baranger [111], this figure highlights that errors in threshold choice for SVD and SVD-a can cause substantial loss in image quality. The lower temporal cutoff can have the greatest effect on image quality, as it is a primary means of rejecting on-axis clutter and the cutoff is operator-dependent. HOSVD is less sensitive to the temporal frequency cutoff choice than SVD and SVD-a, maintaining a broader region of image quality. This is important for clinical imaging scenarios, where factors such as accelerative motion can confound cutoff selection [56].

The differences observed between SVD and SVD-a merit further research but may be explained by several underlying factors. First, we assume that the temporal information provided by the right singular vectors in SVD and SVD-a are comparable. However, scatterer translation is observed differently across the aperture [130], therefore it is reasonable to hypothesize that temporal information may be encoded differently. In addition, the consistency of basis estimation using sample data matrices is dependent on the ratio between the number of samples and number of observations [131]. Since the temporal singular vectors of SVD-a are derived using a factor equal to the number of channels (N) additional observations, there may be implicit differences between the SVD-a and SVD subspaces.

3.5.3 Classifier Performance

The classifier scheme used to generate the HOSVD filter cutoffs demonstrated robust performance in simulation. The power Doppler images generated using the classifier-generated cutoffs produced reasonably similar image quality in comparison to the to the optimal cutoff case. This result is quantified via the AUC analysis in Fig. 3.11, where the HOSVD classifier cutoff produced a maximal AUC of 0.987 ± 0.009, in comparison to the optimal cutoff AUC of 0.994 ± 0.004. In comparison, the maximal P_{SVD} and P_{SVD-a} AUC

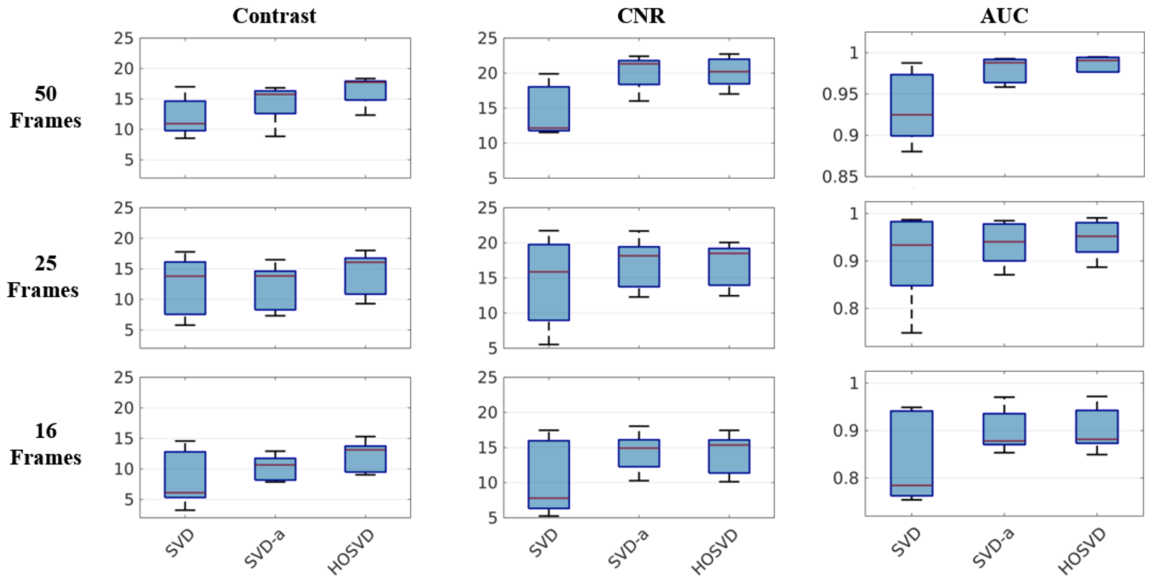

Figure 3.11: Image quality results for ensembles of 50 (*top*), 25 (*center*), and 16 (*bottom*) using the classifier-generated cutoffs. *Left to Right:* Contrast (dB), CNR (dB), AUC.

values were measured as 0.933 ±0.044 and 0.979 ± 0.016. HOSVD produced a maximum contrast of 16.37± 2.45 dB, compared to SVD (12.10 ± 3.34 dB) and SVD-a (14.28 ± 3.24 dB).

3.5.4 Short Ensemble Performance

Across ensemble sizes, HOSVD remained an effective method for clutter rejection. Fig. 3.11 shows maximum contrast, CNR, and AUC for ensemble sizes of 16, 25, and 50 frames. For 16 frames, P_{HOSVD} produced a maximum contrast of 12.07± 2.64 dB, compared to P_{SVD} (8.43 ± 4.74 dB) and P_{SVD-a} (10.21 ± 2.12 dB). For 25 frames, P_{HOSVD} produced a maximum contrast of 14.21 ± 3.69 dB, compared to P_{SVD} (12.21 ± 5.06 dB) and P_{SVD-a} (12.05 ± 3.90 dB).

The HOSVD and SVD-a filters have similar tissue rejection performance because they leverage the same temporal singular vectors produced by the unfolded data tensor for tissue classification, as described in Section III.A. However, the HOSVD filter additionally leverages spatial and aperture domain signal suppression, which enables greater rejection of noise and off-axis signals. In addition, aside from rank limitations, the spatial and aperture domain signal classification methods are independent of temporal ensemble length. This is supported by Figure 3.11, which shows that HOSVD filter consistently yielded contrast gains over the conventional SVD filter, which demonstrates effective clutter rejection despite varied ensemble size. Further, the HOSVD filter consistently yielded a median AUC above 0.85 for varied ensemble lengths indicating that vessel discrimination remained strong. Overall, this demonstrates that HOSVD is robust to ensemble-size constraints observed on clinical scanners.

3.5.5 *In vivo* study

3.5.5.1 Image Quality Performance

In vivo feasibility is demonstrated in liver data, as shown in Figure 3.12, which depicts the P_{HOSVD}, P_{SVD}, and P_{SVD-a} images. As shown in Figure 3.13, HOSVD produced greater rejection of clutter and noise, yielding a maximum contrast of 14.15±2.69 dB and maximum CNR of 19.01 ±3.03 dB. In comparison, the SVD filter produced a contrast of 9.92 ±2.83 dB and CNR of 14.96 ±3.15 dB, and the SVD-a filter produced a contrast of 10.49 ±2.95 dB and CNR of 17.05 ±3.03 dB. Figure 3.14 depicts the effect of over-estimation and under-estimation of the temporal frequency cutoff, which is manually parameterized. Similar to the findings of Baranger et. al [109], threshold estimation error results in decreased image quality for all filters. However, the HOSVD filter retains a higher contrast at non-optimal cutoff frequencies in comparison to SVD and SVD-a.

This pilot study shows that HOSVD filtering can improve visualization of blood flow in clinical imaging scenarios. The HOSVD filter improves contrast, which improves assessment of vasculature through the reduction of clutter and noise. Abdominal ultrasound imaging is associated with higher rates of inadequate clinical visualization and limitations due to poor image quality [84]. Due to improved suppression of noise and clutter, small

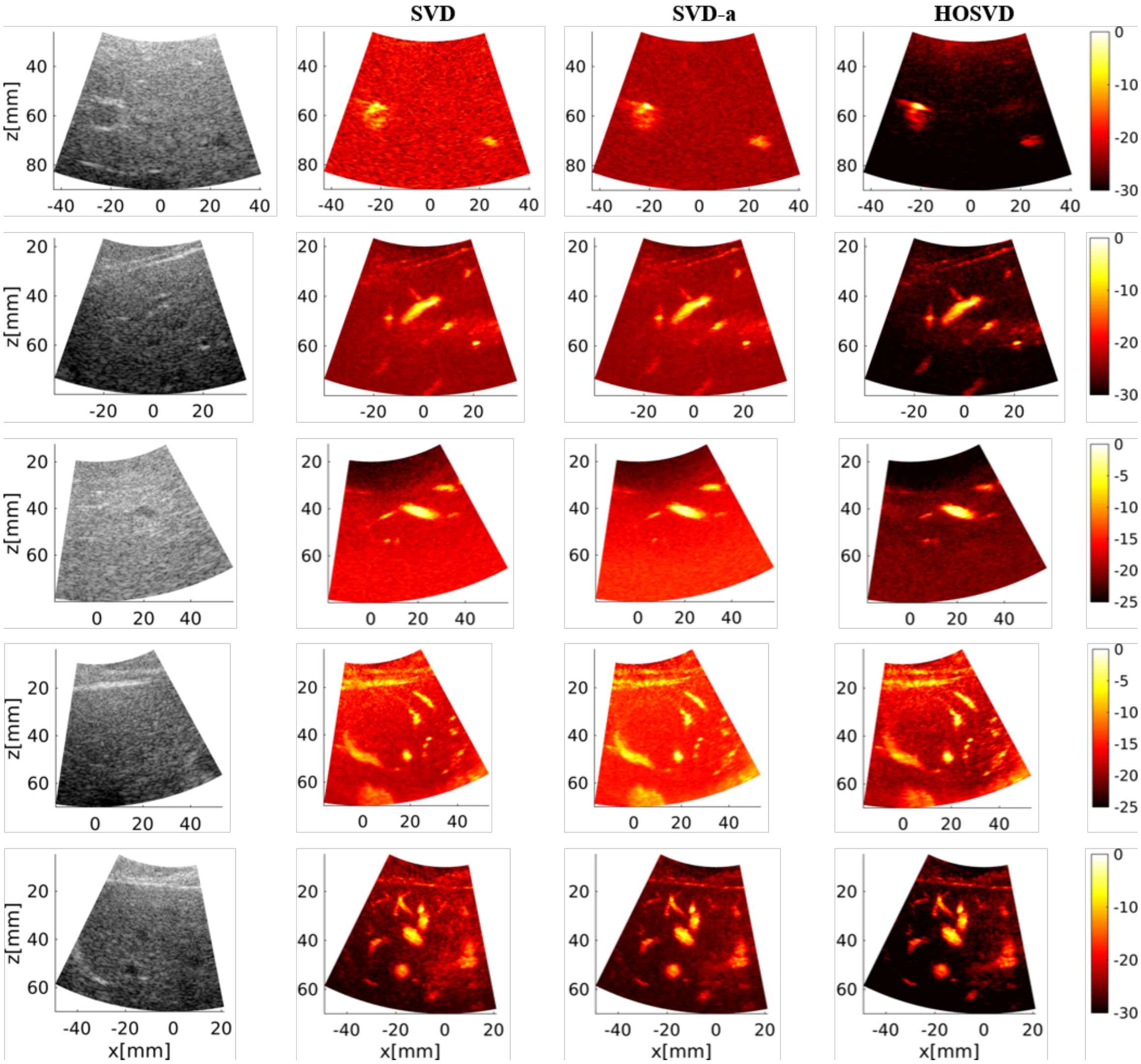

Figure 3.12: *Left to Right:* B-mode, P_{SVD}, $P_{\text{SVD}-a}$, and P_{HOSVD} images depicting peripheral blood flow in a healthy liver. B-mode images are shown on a 60 dB scale. Filtered images display the highest contrast achieved using each filter.

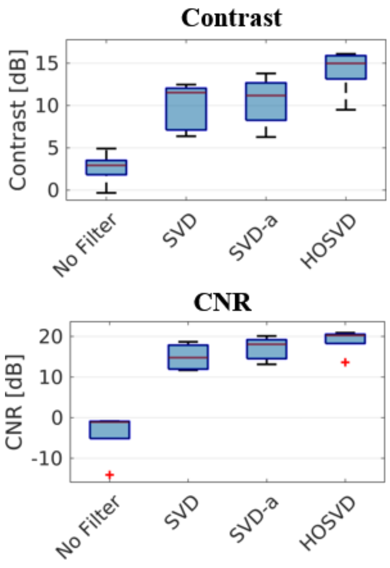

Figure 3.13: Image quality results for *in vivo* study. Results are depicted for power Doppler images formed using SVD, SVD-a, and HOSVD filtering. Metrics for a non-filtered power Doppler image shown for reference.

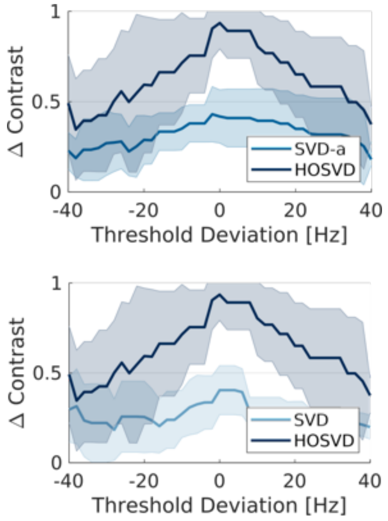

Figure 3.14: Effect of over-estimation and under-estimation of the temporal frequency cutoff on image contrast, shown in terms of relative change in comparison to the maximum achievable contrast.

vasculature is more readily observed with HOSVD filtering in comparison to SVD and SVD-a.

3.5.6 Computational Complexity

One drawback of HOSVD filtering is its associated computational complexity. As shown in Figure 3.15, the computation time increases at a greater rate with HOSVD in comparison to SVD. This suggests that block-wise, downsampling [114], or projecting [132] may greatly improve HOSVD processing speed. In addition, blockwise processing reduces variation caused by time-gain compensation and depth-dependent effects, which may improve estimation of the Nakagami parameters. Further, performing a truncated HOSVD has been shown to improve computational time without a reduction in filtering performance [116]. For example, a sequentially truncated HOSVD [133] could be parameterized with an adaptive tolerance that is defined using the upper channel cutoff, spatial

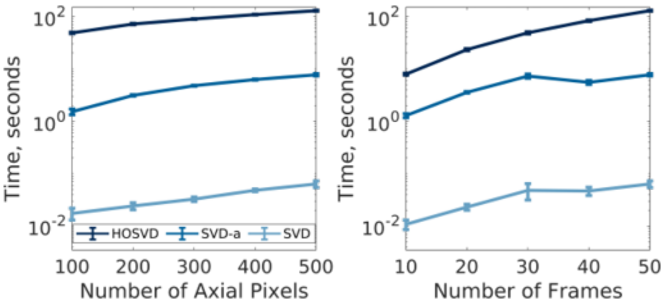

Figure 3.15: Computational expense for SVD, SVD-a, and HOSVD with varied spatial (*left*) and temporal (*right*) parameterization.

cutoff, and channel cutoff.

3.6 Conclusions

Expanding the dimensionality of clutter rejection filters has substantial opportunity for power Doppler imaging. We demonstrate that leveraging spatial, temporal, and aperture features can enable improved rejection of clutter and noise signals. Further, we show that multidimensional decomposition effectively captures dynamic imaging environments in relatively few samples, which is valuable for clinical contexts.

This work validates a semi-automated multidimensional classifier that operates along spatial, temporal, and aperture extents. The classifier leverages theoretical principles of signal phase and amplitude to reject off-axis clutter and noise. These signal features used for classification are likely interchangeable over the different dimensions, as we assume that the noise-bearing components of each dimension are white Gaussian processes. To reject tissue clutter, a frequency-based classifier parameterized by a cutoff frequency is also employed, which is a broadly accepted method within SVD literature [56]. We note that automated approaches to find the lower temporal cutoff have also been proposed, such as computing the minima of the singular value curvature radius [109]. Overall, this semi-automated framework reduces the burden of cutoff parameterization and can improve performance across varied clinical contexts.

Since the HOSVD filter may be used in place of the SVD filter, HOSVD filtering may be used in a variety of imaging applications beyond power Doppler imaging. Singular value decomposition and other blind source separation filtering techniques have been investigated for several other blood flow imaging applications, including color Doppler [56], contrast-enhanced ultrasound [134], and super resolution imaging [135]. Further, similar blind source separation methods have been examined for tissue imaging applications, such as for minimum variance imaging [44], clutter rejection [106], and noise suppression [91]. HOSVD filtering can also be used concurrently with other post-processing methods, including morphological filtering or background noise removal [106], [135]. The combination of adaptive clutter filtering and noise suppression algorithms has been shown to yield remarkable improvements in image quality, and we anticipate HOSVD filtering would yield a similar combinatorial benefit.

Additionally, HOSVD filtering may be directly amenable to adaptive beamformers. A number of techniques have been proposed which require clutter rejection filtering of aperture or sub-aperture data, including coherent flow power Doppler (CFPD) [62], power-preserving coherent flow power doppler (ppCFPD) [73], short-lag angular coherence (SLAC) [52], and acoustic sub-aperture processing (ASAP) [91]. A drawback of coherence-based adaptive beamformers is the presence of ‘dark region artifacts’, which manifest due to strong off-axis scattering [103]. Since HOSVD filtering can reject off-axis contributions, it may effectively mitigate dark region artifacts in adaptive beamforming. Adaptive beamformers have been shown to benefit from synthetic transmit focusing, which aligns with the assumption of low phase dispersion for the aperture domain classifier. Techniques that use a fixed transmit focus will exhibit greater phase dispersion away from the focal point, which may degrade performance of the phase-based classifier. Further, we demonstrated the efficacy of HOSVD filtering for visualization of vasculature in the liver, which suggests that HOSVD filtering is well-suited for deeper clinical imaging applications. Clinical visualization of low velocity blood flows and deep imaging targets are frequently limited by body habitus [84]. Future work will assess the combinatorial benefits of using HOSVD filtering with other advanced processing methods, such as adaptive beamforming or motion correction, to visualize low velocity blood flow in liver lesions. A reliable assessment mechanism of lesion blood flow would improve therapeutic evaluation and clinical outcomes.

In this work, we demonstrate that HOSVD may be used for clutter rejection in a scheme in which contiguous blocks of clutter-dominant components are removed. However, several studies have demonstrated that various imaging conditions may incur subspace overlap, in which tissue and blood features are not separately contained [106], [110], [136]. We anticipate that further study on the selective rejection of indices within the core tensor, $\mathcal{G}$, could produce a clutter rejection filter with even greater efficacy.

Overall, we present a methodology for clutter rejection filtering using a HOSVD filter. The proposed technique effectively overcomes the subspace separation limitations of SVD for short ensembles, achieving greater suppression of clutter and noise without loss of blood flow sensitivity. The novel classification scheme additionally considers features of aperture domain data which have previously not been studied in the context of clutter filtering. Demonstration of the proposed HOSVD filter for *in vivo* visualization of small vasculature demonstrates its potential for clinical translation.

Chapter 4

Non-Contrast Ultrasound Imaging for Immediate Evaluation of Transarterial Chemoembolization Procedures

4.1 Introduction

Over the last decade, liver cancer has become a leading cause of cancer-related death in the United States [1]. Despite advances in clinical care, prognosis remains poor because a majority of patients (>70%) are diagnosed with advanced disease and are not eligible for curative intervention [2, 3]. Global treatment guidelines endorse trans-arterial chemoembolization (TACE) as the standard therapy for palliative care, bridge-to-transplant, and downstaging of intermediate-stage liver cancer [8].

TACE involves the delivery of a chemotherapeutic drug and embolizing agents via a catheter placed within a tumor-feeding arterial vessel. Successful TACE elicits occlusion of the tumor vascular supply and can prolong survival up to 5 years. For improved disease management, multiple TACE sessions are often performed based on initial treatment efficacy [8, 11, 15].

Therapeutic efficacy is determined by reduced contrast enhancement on MRI or CT, which correlates with tumor necrosis [8, 17]. However, therapeutic evaluation is not performed until 4-6 weeks post-treatment due to confounding interactions with the chemotherapeutic delivery agent, lipiodol, and post-embolization inflammatory changes [8, 18]. This delays re-treatment and can lead to interim disease progression. A reliable, early assessment mechanism could improve survival.

Ultrasound has been proposed as an alternative modality for earlier evaluation of TACE response. Contrast-enhanced ultrasound (CEUS) has demonstrated efficacy in several studies for differentiation of TACE outcomes as early as 1-2 weeks post-treatment [23]. Qualitative and quantitative assessment methods, including time-intensity analysis and morphological feature detection, have been proposed for CEUS assessment [18, 22]. CEUS for liver imaging is approved by the United States Food and Drug Administration and is advantageous over other contrast-enhanced modalities due to cost, portability, and lack of ionizing radiation [137]. However, detection earlier than 1-2 weeks can be compromised by hyperechoic artifacts produced by trapped gas and the deposition of drug-eluting beads (DEB) used in DEB-TACE [18, 23]. In addition, not all liver lesions exhibit contrast washout and variations in contrast dose or timing may cause lesion mischaracterization; as a result CEUS is unsuitable for standalone staging [137, 138].

In comparison, non-contrast power Doppler images display the strength or power of the Doppler echo produced by moving red blood cells and are less susceptible to artifacts from the TACE treatment. Historically, power Doppler evaluation of liver lesions was limited by poor sensitivity toward low velocity blood flow; however, the development of advanced Doppler techniques for motion compensation and filtering has aided in overcoming this barrier [25, 26]. Several studies have demonstrated the diagnostic utility of power Doppler with advanced processing techniques for the characterization of liver lesions [139, 140]. Recently, power Doppler has been proposed for the diagnosis of Hepatocellular Carcinoma (HCC) [72, 139] and the detection of residual blood flow following TACE [27, 41].

However, motion artifacts and poor image quality remain primary limitations for non-contrast power Doppler detection of blood flow in liver lesions [41]. Poor image quality results from attenuation of the echo signal, which limits the signal-to-noise (SNR) ratio for deep imaging targets. Cirrhotic liver tissue, which has a higher attenuation than healthy parenchyma, is frequently associated with HCC and can further exacerbate this barrier [141]. In addition, motion or ‘flash’ artifacts are a limitation of Doppler imaging caused by insufficient rejection of the tissue signal, which can be 40-100 dB larger than the blood signal [53]. The presence of motion causes spectral overlap between the tissue and low-velocity blood signals, which compromise conventional filtering methods. For liver imaging, the cardiac cycle and diaphragm motion are primary reported sources of motion artifacts [41].

Recently, several aperture domain techniques to reduce these barriers for blood flow imaging have been proposed. To overcome SNR limitations, coherence-based image formation methods have been developed as an alternative to power Doppler [52, 62, 73, 107, 142]. Li *et al.*proposed Coherent Flow Power Doppler (CFPD), which employs a measure of the short-lag spatial coherence to suppress noise and acoustic clutter [45, 62]. Similarly, an adapted form of this technique, termed power-preserving CFPD (ppCFPD), employs a measure of spatial covariance to retain proportionality between image intensity and blood volume [73, 90, 143].

This study aims to investigate the ability of using non-contrast power Doppler imaging to detect changes in low velocity flow as a means for early evaluation of TACE therapeutic efficacy. Adaptive filtering and processing methods to reduce noise bias and artifacts caused by motion are considered. In addition, this work studies the feasibility of using coherence-based beamforming to improve the detection of low velocity blood flow in liver lesions. This work extends the prior work of Tierney *et al.*who demonstrated the feasibility of detecting residual blood flow after TACE using non-contrast ultrasound with motion correction and adaptive filtering methods [27].

4.2 Data Acquisition

4.2.1 Subject Recruitment

A retrospective analysis was performed using ultrasound data collected from 17 human subjects undergoing conventional TACE for the treatment of liver cancer at the Vanderbilt University Medical Center between February 2018 and October 2019. The data was acquired with informed consent of the subjects and the approval of the Vanderbilt University institutional review board as part of an ongoing study. One of the subjects underwent TACE twice, resulting in a total of 18 procedural data acquisitions. In the present study,

Table 4.1: Subject Characteristics

ID	**BMI [$\frac{kg}{m^2}$]**	**MELD**	**Type**	**Size [cm]**	**Location**	**Response**
1	51.9	11	HCC	4.7	Segment 3	PR
2	24.2	12	HCC	2	Segment 5/6	CR
5	25.8	13	HCC	2.4	Segment 5	PR
6	25.0	N/A	NET	6	Segment 6/7	CR
7	22.4	N/A	NET	4.1	Segment 4B	CR
8	29.9	11	HCC	4.5	Segment 5	PR
9	32.5	7	HCC	3.4	Segment 5/6	CR
10	23.9	7	HCC	4.6	Segment 7	PR
11	24.4	N/A	NET	6	Segment 6	SD
12	24.8	13	HCC	5.3	Segment 6	CR
13	45.9	14	HCC	5.2	Segment 5/6	CR
15	22.7	8	HCC	4	Segment 3	CR

Table of subject demographics and tumor characteristics. The targeted lesions consisted of hepatocellular carcinoma (HCC) or neuroendocrine tumors (NET). The tumor size depicts largest measured diameter. Tumor response indicates the mRECIST score at the first follow-up after TACE.

one dataset was excluded from analysis due to incomplete data acquisition and five were excluded due to insufficient visualization of tumor vasculature on Pre-TACE images. An example of excluded image cases are shown in Figure 4.1. Of the included 12 cases, the targeted lesion was hepatocellular carcinoma (N=9) or a neuroendocrine tumor (N=3). Table 4.1 outlines the patient's demographic characteristics including BMI, tumor size, tumor location, and treatment response. The MELD score, a measure of mortality risk, is provided for subjects with HCC. The MELD score is not an effective predictor for NET cases, as the patient's liver synthetic function is often preserved [144].

The subject demographics were fairly representative of population characteristics described in other published findings. A majority of the cases involved posterior (N=8) or anterior (N=5) segments, rather than lateral (N=2) and medial (N=1) segments. This aligns with previously studied cohorts, which report a greater proportion of lesions in the right lobe [145, 146]. The average lesion diameter (4.35 ± 1.27 cm) and MELD score (10.67 ± 2.70) were also representative of published values (diameter = 1.4-5 cm, MELD = 10-11) [145–149]. In addition, this study includes examples of lesions with large diameters (>5 cm), multi-segment involvement, and medial location (Segments 1 and 4). These features are often associated with poorer treatment response, due to proximal vasculature that is favorable for feeder vessel recruitment and the difficulty of achieving complete embolization in large lesions [145, 148–150].

However, we note that non-contrast ultrasound methods may be less effective for assessment of deep lesions and among patients with obesity. In the current work, only subjects with peripheral lesions (*e.g.* lesion within 10 cm imaging depth) were recruited. We note that roughly 20% of HCC lesions are centrally located (*e.g.* ≥ 3 cm of liver capsule) [149, 151, 152]. Ultrasound imaging of deeper targets is more susceptible to degraded SNR due to attenuation; however, lesion depth has not been identified as a predictor for TACE response [149]. In addition, a majority of the recruited subjects exhibited a healthy body mass index (BMI) ($< 25 kg/m^2$). Obesity is associated with poor TACE outcomes and contributes to degraded ultrasound image quality, which may lead to exam failure [84, 153]. Assessment of TACE response using ultrasound for subjects with deep lesions and obesity will be validated in future work.

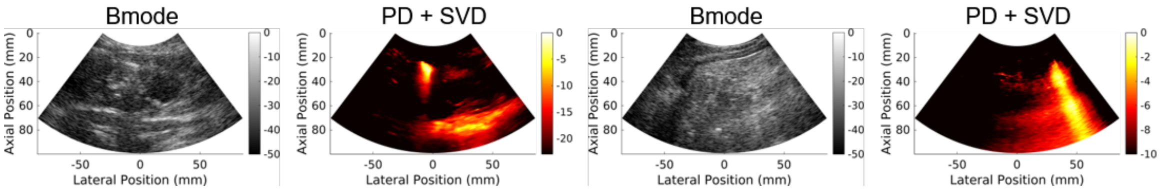

Figure 4.1: Insufficient visualization of tumor vasculature is caused by the presence of hyperechoic imaging artifacts, possibly produced by reverberation or tissue leakage due to motion. Examples of these artifacts are shown for Subjects 3 and 4.

4.2.2 Treatment Response

Treatment response was evaluated approximately one month after treatment using contrast-enhanced CT or MRI. At clinical follow-up, the lesions were classified as exhibiting progressive disease (PD), stable disease (SD), partial response (PR), or complete response (CR) using the modified Response Evaluation Criteria in Solid Tumors [17]. Here, the treatment was defined as incomplete (*i.e.* PD, SD, PR), suggesting residual tumor burden, or defined as complete (*i.e.* CR), indicating a total reduction in enhancement and tumor size. At the first follow-up, 7 cases were classified as complete response (CR=7), and 5 cases yielded an incomplete response (PR=4, SD=1).

4.2.3 Data Acquisition

All data acquisition was completed using a Verasonics research scanner equipped with a C5-2 transducer operating at a center frequency of 4.16 MHz with a 16.6 MHz sampling frequency. The imaging sequence was composed of nine angled plane waves spaced evenly between -8 and 8 degrees at a frame rate of 5.4 KHz. Plane wave synthetic focusing (PWSF) was applied, yielding a net frame rate of 600 Hz [58].

Ultrasound data was collected from subjects in the operating suite immediately before and immediately after undergoing TACE therapy. Selection of the imaging field of view and data collection was performed by a trained interventional radiologist. Three datasets each consisting of 1,200 frames (2 seconds) were obtained at each timepoint, and one dataset was selected for image processing based on tumor visualization and motion characteristics.

The spatiotemporal coherence was computed to adaptively select an ensemble of 300 consecutive frames (0.5 seconds) to form the images. As described by Nayak *et al.*, the

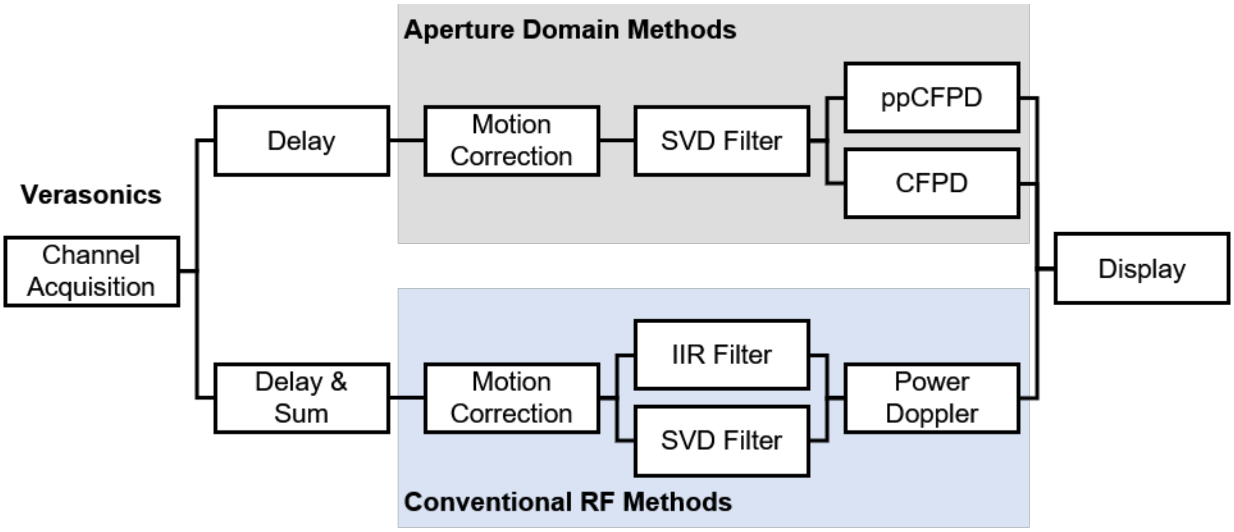

Figure 4.2: Four image processing pipelines were tested: ppCFPD + SVD filtering, CFPD + SVD filtering, Power Doppler + SVD filtering, and conventional Power Doppler + IIR filtering. Adaptive demodulation (AD) was used to reduce degradation due to axial motion.

spatiotemporal coherence matrix can be computed as

$$C(i,j) = \frac{\sum_{x1}^{N_x}\sum_{z=1}^{N_z}\left(y_i(x,z)-\bar{y}_i(x,z)\right)\ \left(y_j(x,z)-\bar{y}_j(x,z)\right)}{\sqrt{\sum_{x=1}^{N_x}\sum_{z=1}^{N_z}\left|y_i(x,z)-\bar{y}_i(x,z)\right|^2\ \ \sum_{x=1}^{N_x}\sum_{z=1}^{N_z}\left|y_j(x,z)-\bar{y}_j(x,z)\right|^2}}. \tag{4.1}$$

between successive frames, y_i and y_j, over all axial and lateral (N_z and N_x) pixels. High spatiotemporal coherence is associated with low axial, lateral, and out-of-frame motion, which are sources of degradation in power Doppler images [154–156]. For the coherence computation, a 7 cm axial range centered around each tumor was used. The 300 frame ensemble with the highest mean coherence was used for image formation.

4.3 Image Formation

4.3.1 Pre-Processing

Four image processing pipelines were considered to assess the utility of adaptive filtering and coherence-based beamforming (CFPD and ppCFPD), as shown in Figure 4.2. The aperture domain methods were compared to conventional power Doppler images formed with adaptive SVD filtering and conventional IIR filtering. All image processing methods studied used matched pre-processing, described as follows.

Processing and analysis were performed with Matlab (version R2018b, MathWorks, Natick, MA), using Vanderbilt's Advanced Computing Center for Research and Education (ACCRE). Beamforming was implemented using the UltraSound ToolBox (v2.1) and the TensorLab (v3.0) function mlsvd was used for HOSVD [127, 128]. In addition, CFPD and ppCFPD processing was performed using a modified implementation of the C++ spatcov library [52, 157].

The conventional power Doppler images were produced from the radiofrequency (RF) data, which was obtained by beamforming the channel data. Since plane wave imaging was used, synthetic transmit focusing was achieved by compounding each steered transmission [58]. The coherence beamforming methods studied in this paper operate on 'aperture data', rather than RF data. Aperture data refers to the delayed channel data after plane wave synthetic transmit focusing, prior to the channel sum.

To reduce axial motion, adaptive demodulation was applied to the RF or aperture data [79]. The estimated motion profile for adaptive demodulation was obtained from the RF data using a 1 mm axial kernel. All images were formed using a 9 cm field of view, processed in 1 cm axial blocks for computational efficiency.

To facilitate SVD filtering, the data is reshaped into a Casorati form. For RF data, this is a matrix of size $\mathbb{C}^{XZ \times T}$, composed of $X \times Z$ spatial pixels and T temporal frames. Similarly, for aperture data, the casorati form is a matrix of size $\mathbb{C}^{XZC \times T}$, where C is the number of channels. Filtering was implemented using random sampling of each 1 cm axial image block to form 10 submatrices as described by Song *et al.*[108].

4.3.2 Power Doppler with IIR Filtering

Power Doppler images are conventionally formed using a wall filter that rejects low frequency signals. However, wall filters impose a trade-off between the rejection of non-stationary clutter and the preservation of low velocity blood flow. These low-frequency signals overlap in the Fourier Domain, which has historically limited Doppler detection of blood flow to velocities greater than 5-15 mm/sec [53]. Here, we employ a 6th order Chebyshev infinite impulse response (IIR) filter applied to the RF data to demonstrate the 'clinical standard'.

The power Doppler image was reconstructed from the filtered RF data, $RF(a)$, over a temporal ensemble of length A as

$$PD = \sum_{a=1}^{A} |RF(a)|^2 \tag{4.2}$$

Averaging was performed over an axial kernel of one wavelength to reduce error, as described by Loupas *et al.*[89].

4.3.3 Power Doppler with SVD Filtering

Recent advances in adaptive SVD filtering have enabled improved sensitivity toward low velocity blood flow. Several clinical systems have developed 'low velocity' imaging modes that use adaptive filtering, including Superb Microvascular Imaging (Canon Medical Systems, Otawara, Japan) and Microvascular Flow Imaging (Samsung Medison Co., Ltd., Seoul, Korea) [41].

Various techniques exist for SVD filter implementation and subspace classification [56]. In this embodiment, the singular value decomposition is performed on the Casorati matrix of RF data. Tissue clutter is suppressed by removing the lower order singular value components, which are classified using the mean frequency of the corresponding temporal singular vectors. Similar to IIR filtering, adaptive cutoff is performed by defining a cutoff frequency [65]. After filtering, the power Doppler image is formed as written in Eq. 4.2.

4.3.4 Coherent Flow Power Doppler (CFPD) with SVD Filtering

Coherent Flow Power Doppler (CFPD) images display the normalized spatial coherence of the backscattered blood echo. CFPD imaging estimates the short-lag spatial coherence after applying a filter to remove the tissue signal. For clarity, we note that ‘spatial’ coherence refers to the measure of coherence across the aperture dimension, *e.g.* between pairs of channels. Several forms of extraneous signals that degrade image quality, including noise and reverberation clutter, are uncorrelated and suppressed in CFPD imaging.

After transmit focusing and performing adaptive demodulation, the aperture data was reshaped into a casorati form, *e.g.* that spatial and channel dimensions were combined. SVD filtering was then performed as described in Subsection 4.3.3, where a lower cutoff was obtained to remove the tissue signal. The filtered aperture data then undergoes short-lag spatial coherence processing, whereby an estimate of the normalized spatial coherence is obtained. The normalized spatial coherence, $R(m)$, for a transmit aperture of size N may be written as

$$R(m) = \frac{1}{N-m} \sum_{i=1}^{N-m} \frac{\sum_{n=n_1}^{n_2} y_i(n) y_{i+m}(n)}{\sqrt{\sum_{n=n_1}^{n_2} y_i^2(n) \sum_{n=n_1}^{n_2} y_{i+m}^2(n)}}, \tag{4.3}$$

which is calculated for all pairs of aperture signals, y_i and y_{i+m}, separated by a given channel separation or lag, m. To reduce random errors, estimation over an axial kernel, n, of one wavelength is employed.

The short lag spatial coherence metric is obtained by averaging the normalized spatial coherence for a set of M successive lags as

$$V(a) = \frac{1}{M} \sum_{m=1}^{M} R(m). \tag{4.4}$$

The CFPD image is then reconstructed using a modified power estimate for an ensemble of length A, as

$$CFPD = \sum_{a=1}^{A} V(a)^2. \tag{4.5}$$

4.3.5 Power Preserving CFPD with SVD Filtering

The image intensity of CFPD portrays the normalized spatial coherence, rather than the power of the Doppler echo [62]. This can be beneficial for detection tasks, as CFPD is less sensitive to depth-dependent effects [84]. However, unlike power Doppler, CFPD intensity has a non-linear response toward the number of blood scatterers, which limits detection of changes in blood flow [73]. Power preserving CFPD (ppCFPD) is a modified form of CFPD that employs a measure of covariance, rather than normalized coherence. This method preserves the linear relation between image intensity and scatterer density, while retaining suppression of incoherent signals [73]. For ppCFPD, the spatial covariance may be written

$$\breve{R}(m) = \frac{1}{N-m} \sum_{i=1}^{N-m} \sum_{n=n_1}^{n_2} y_i(n) y_{i+m}(n). \tag{4.6}$$

Similarly, the spatial covariance is averaged for a set of M successive lags as

$$\breve{V}(a) = \frac{1}{M} \sum_{m=1}^{M} \breve{R}(m). \tag{4.7}$$

and the ppCFPD image is reconstructed using the relation

$$\text{ppCFPD} = \sum_{a=1}^{A} \breve{V}(a). \tag{4.8}$$

Note that Equation 4.8 omits the square term shown in Equation 4.5; the computation of covariance in Eq. 4.6 results in units of amplitude squared, *e.g.* power, so the ppCFPD image scale remains equivalent to power Doppler. For both CFPD and ppCFPD, a maximum lag (M) of 15 was used.

4.4 Analysis

Power Doppler image intensity is proportional to the volume of blood scatterers that exhibit a velocity exceeding the filter cutoff frequency [86, 158]. For equal assessment between paired pre-TACE and post-TACE images, a single cutoff frequency between 10 and 80 Hz (2-15 mm/sec) was chosen for each subject and filter type. The lowest cutoff frequency that enabled rejection of tissue clutter at the tumor site was selected.

4.4.1 Changes in Contrast as a Measure of Therapeutic Efficacy

To quantify the differences between the pre-TACE and post-TACE images, the change in tumor-to-noise contrast was measured. Contrast enables a relative measure of the tumor intensity compared to the background noise. Noise arises from the electronic components of the ultrasound system and is approximately uniform over the full field of view. However, image processing methods, such as as time-gain compensation, cause spatial variation of the noise profile. To facilitate comparison between images, noise equalization was applied to reduce intensity bias. The noise field for each dataset was estimated using the last-rank singular vector obtained from the SVD performed for power Doppler image formation, as described by [106].

The anatomical Bmode image was used to identify the tumor boundary and generate

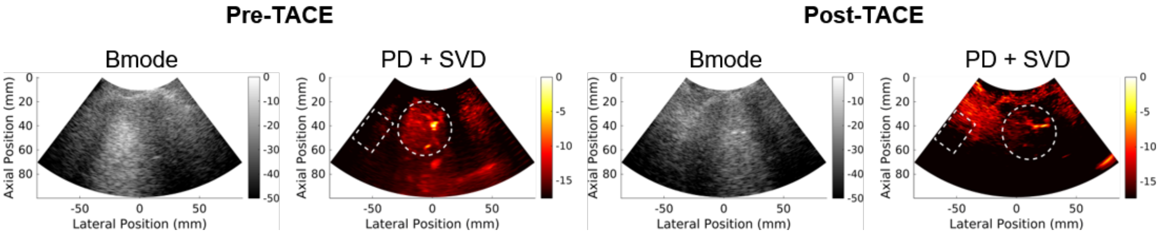

Figure 4.3: Example of paired pre-TACE (*left*) and post-TACE (*right*) ROIs generated for Subject 6.

a tumor region of interest (ROI) for each case, as depicted in Figure 4.3. The size of the ROI was scaled to the largest tumor diameter, measured using the pre-treatment CT or MRI, and adjusted based on the field-of-view. The noise ROI was defined as a 20×30 mm rectangular region corresponding to noise in the PD image formed using SVD filtering. Using the tumor and blood ROIs, the contrast was measured as

$$C = 10\log_{10}(\frac{\bar{S}_{tumor}}{\bar{S}_{noise}}), \tag{4.9}$$

where $\bar{S}_{tumor}$ indicates the average tumor intensity and $\bar{S}_{noise}$ is the mean noise intensity. Since the TACE procedure occludes blood flow at the tumor site, a decrease in contrast between pre-TACE and post-TACE images was expected for successful cases. The change in contrast between time points was measured for each subject as $C_{Pre-TACE} - C_{Post-TACE}$.

4.4.2 Coherence-Based Beamforming

Unlike PD and ppCFPD, CFPD image intensity does not scale linearly with echo power so changes in CFPD image contrast are not proportional to changes in blood flow. However, coherence-based imaging can improve detection tasks, such as the identification of tumor-feeding vessels [84]. To study the feasibility of using CFPD and ppCFPD imaging to detect tumor blood flow, the tumor-to-background contrast and generalized contrast-to-noise ratio (GCNR) were computed for the pre-TACE images. Both complete and incomplete pre-TACE cases were considered.

Since HCC and NET are hypervascular lesions, the pre-TACE images were expected to produce a positive tumor-to-background contrast, measured using Eq. 4.9. Since the contrast quantifies the difference between the tumor and background enhancement, a higher contrast is assumed to indicate improved visibility of the lesion.

Similarly, the generalized contrast-to-noise ratio (GCNR) measures the likelihood of discrimination based on the amount of overlap between the signal and background intensity

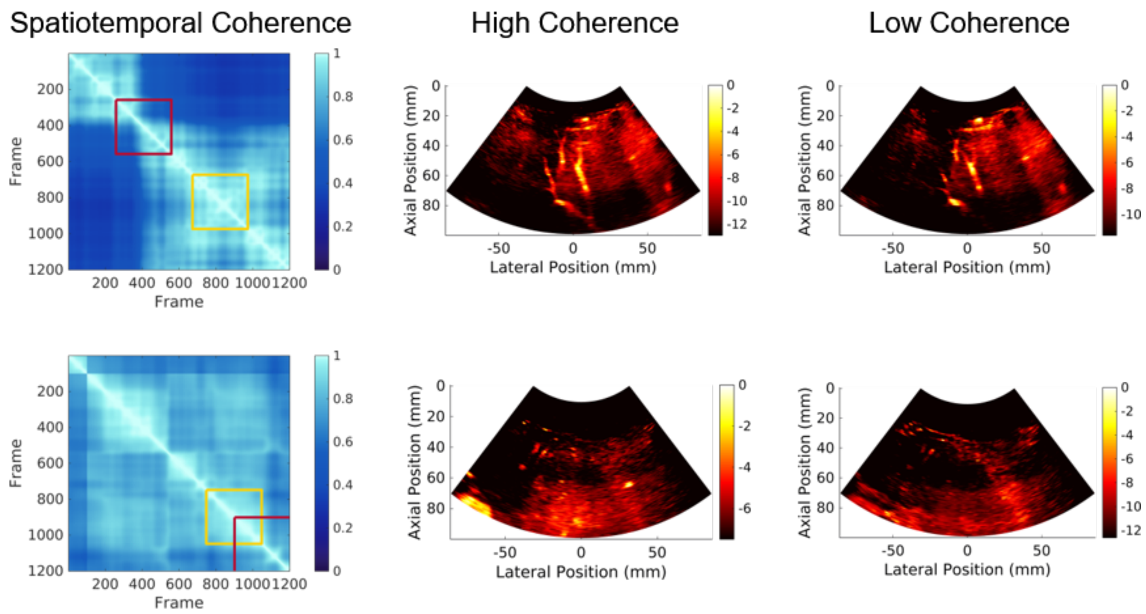

Figure 4.4: Examples of data ensembles with low (red box) and high (yellow box) spatiotemporal coherence for Subject 10 (*top*) and Subject 1 (*bottom*). The high coherence image (*center*) exhibits higher blood flow sensitivity than the low coherence image (*right*).

histograms [100]. The GCNR is computed as

$$GCNR = 1 - \int_{-\infty}^{\infty}\int_{-\infty}^{\infty} \mathbf{min}\{f(x)g(x)\}dx, \tag{4.10}$$

where $f(x)$ is the intensity distribution of the background and $g(x)$ is the intensity distribution of the blood signal. A GCNR of 1 indicates complete discrimination of the blood signal from the background, and a GCNR of 0 indicates no discrimination. For this study, 256 bins were used.

4.5 Results and Discussion

Images are displayed on a log scale with the upper bound (0 dB) equal to the maximum image intensity. The lower bound of the dynamic range was defined as the median intensity of the background region of interest for each image.

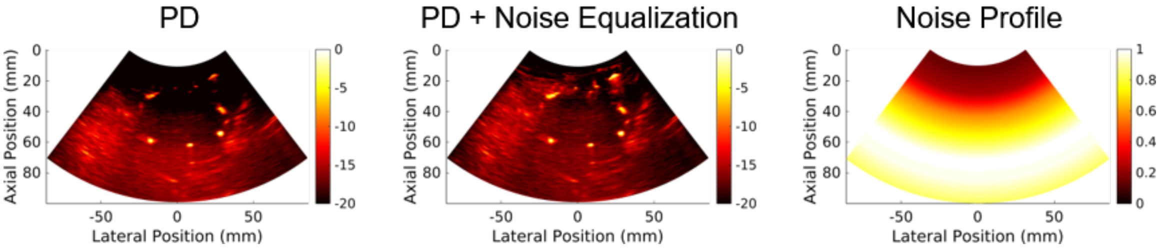

Figure 4.5: Conventional power Doppler images (*left*) exhibit a depth-dependent bias that can be reduced by performing noise equalization (*center*). The derived noise profile for Subject 11 is shown on the right.

4.5.1 Spatiotemporal Coherence

Qualitatively, the global spatiotemporal coherence was an effective indicator of data quality and metric for adaptive ensemble choice. Ensembles with low spatiotemporal coherence exhibited greater motion and may require higher cutoff frequencies for sufficient rejection of the tissue signal, which can decrease sensitivity toward low velocity blood flow. Adaptive demodulation additionally improved ensemble coherence through the reduction of axial motion. As shown in Figure 4.4, spatiotemporal coherence may be a valuable metric to assess image quality during clinical data acquisition and processing.

4.5.2 Noise Equalization

Noise equalization improved differentiation of low intensity blood flow, especially for deep targets in SNR-limited conditions [44, 106]. In addition, applying the equalization produced a more uniform noise floor, depicted in Figure 4.5 which permits equitable comparison between images. As shown in Figure 4.6 the pre-TACE power Doppler contrast was improved for both IIR filtering (before: 0.34 ± 4.05 dB, after: 2.27 ± 2.18 dB) and SVD filtering (before: 0.34 ± 3.16 dB, after: 2.25 ± 1.37 dB) with noise equalization.

4.5.3 Changes in Contrast as a Measure of Therapeutic Efficacy

Treatment-induced changes in tumor contrast are observed after TACE. As shown in Figure 4.7, cases with a complete response exhibited a decrease in contrast (IIR = 2.01 ± 1.71 dB, SVD = 2.12 ± 1.44 dB). In comparison, incomplete cases do not exhibit a clear trend for contrast change (IIR = 0.71 ± 3.36 dB, SVD = 0.53 ± 1.17 dB). In this study, an upper SVD cutoff to reject noise is not employed because low velocity flow may exist within the last rank singular vectors [106]. As a result, the SVD and IIR filters exhibit comparable noise rejection and a similar tumor-to-noise contrast. However, the SVD filter was more robust for tissue signal rejection, as shown in Figure 4.8. Since IIR filtering is not adaptive, a higher cutoff frequency often had to be used to achieve sufficient rejection of the tissue signal.

Qualitatively, the observed change in tumor enhancement after TACE aligns with the therapeutic response, as depicted in Figure 4.9. Full suppression of blood flow within and adjacent to the tumor site is observed for Subjects 2 and 15, who exhibited a complete response. In comparison, Subjects 8 and 10 had a partial therapeutic response and exhibit residual blood flow. Before TACE, Subject 8 exhibits discrete and sub-resolvable blood

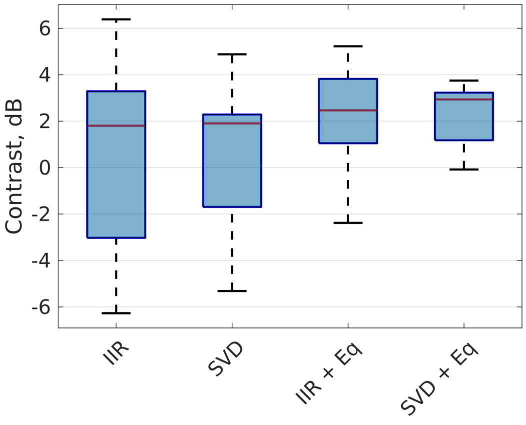

Figure 4.6: The blood-to-background contrast is improved by applying noise equalization.

Filter	CR	PR	SD
IIR	2.01 ± 1.71	0.49 ± 3.83	1.58
SVD	2.12 ± 1.44	0.77 ± 1.2	-0.43

Table 4.2: Change in Contrast (dB) between Pre-TACE and post-TACE images by therapeutic response (CR = 7, PR = 4, SD = 1) for PD images with noise equalization.

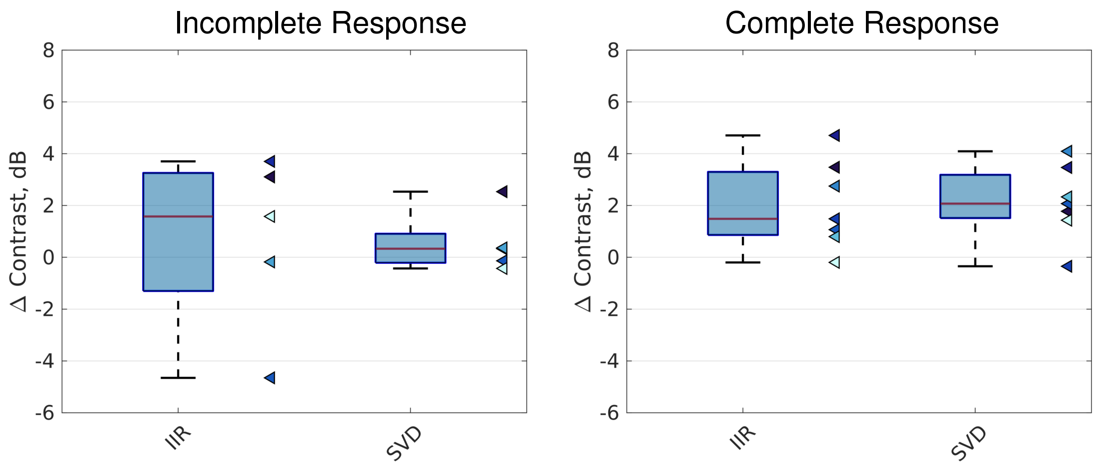

Figure 4.7: Complete (CR) cases exhibited a greater change in contrast after TACE than incomplete (PR, SD) cases.

flow at the tumor site. Although a decrease in vascular burden is observed after TACE, several discrete vessels remain. For Subject 10, the Portal Vein and peripheral tumor vasculature is visible before TACE. The portal vein is no longer in the field of view following TACE, but some residual tumor vasculature is observed. Lastly, Subject 11 had no change in observed vessels following TACE, which corresponds to the stable disease classification at follow up.

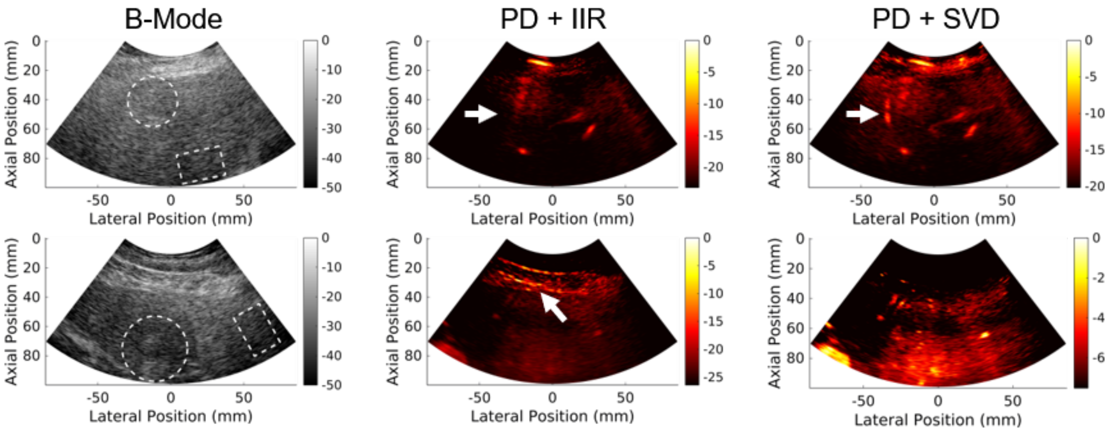

Figure 4.8: As shown for Subject 9 (*top*) and Subject 1 (*bottom*), the SVD filter was more robust than the IIR filter at preserving blood flow and rejecting the tissue signal.

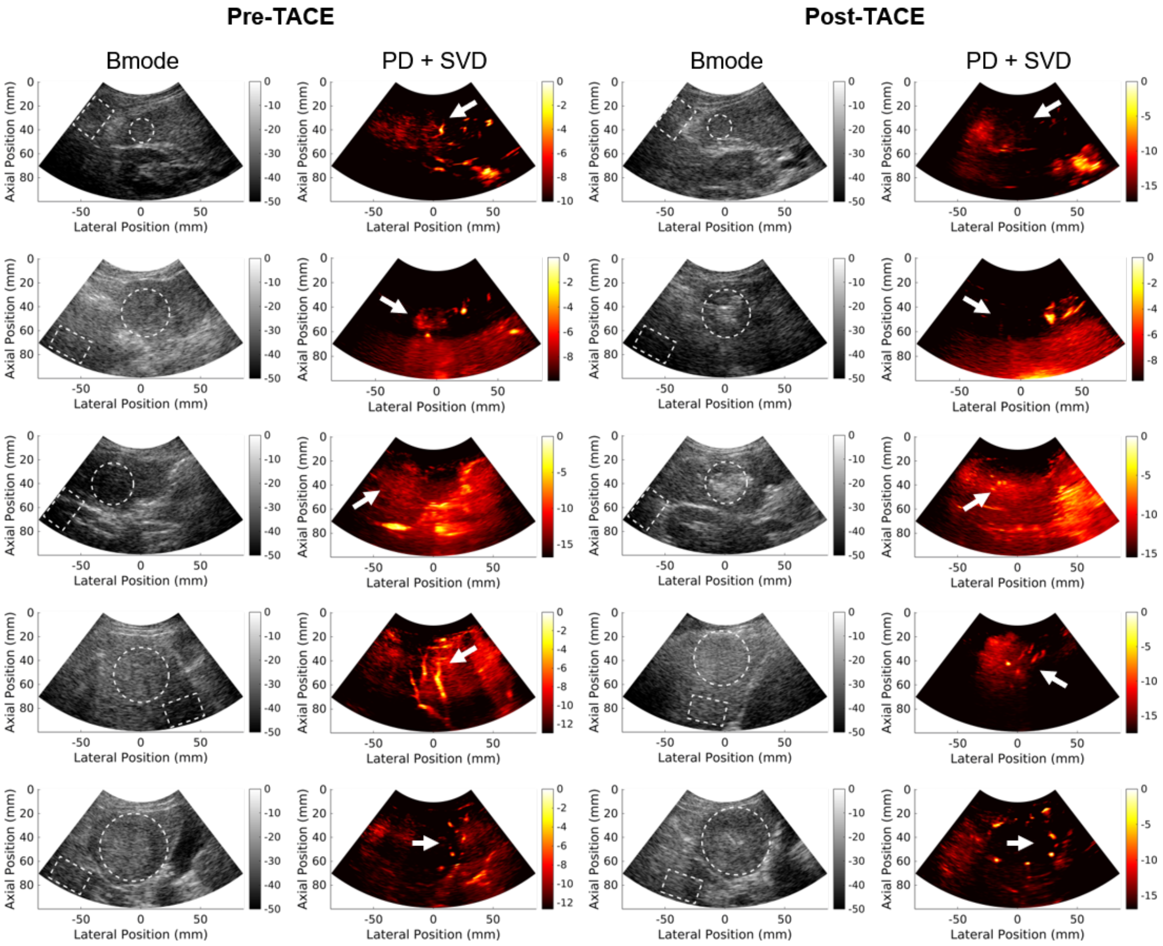

Figure 4.9: Paired Pre-TACE (*left*) and Post-TACE (*right*) images for subjects with complete response, partial response, or stable disease at follow-up using mRECIST criteria.
Rows 1 and 2: Subject 2 and Subject 15 were classified as complete response.
Rows 3 and 4: Subject 8 and Subject 10 were classified as a partial response.
Row 5: Subject 11 presented with stable disease at follow up, indicating no change.

4.5.4 Coherence Beamforming

Initial feasibility for liver tumor flow detection with coherence imaging methods is demonstrated, as potrayed in Figure 4.10. Qualitatively, CPFD and ppCFPD improved suppression of background noise, which yields improved detection of conspicuous vessels. Two cases (Subjects 7 and 11) exhibited ppCFPD image dropout at the tumor location due to dark-region artifacts, described in the next section, and were excluded from image quality assessment. As show in Figure 4.11, the coherence imaging methods produced a

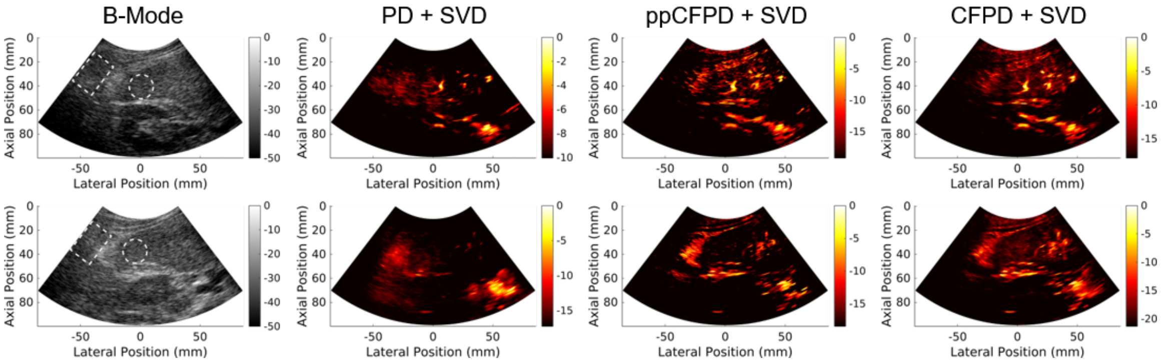

Figure 4.10: Comparison of PD + SVD, ppCFPD + SVD, and CFPD + SVD images for Subject 2. Blood flow is visible at the tumor site for pre-TACE (*top*) and suppressed in post-TACE (*bottom*) images.

higher tumor-to-background contrast (CFPD = 4.81 ± 1.81 dB, ppCFPD = 6.97 ± 4.55 dB) in comparison to the power Doppler methods (IIR = 1.97 ± 2.18 dB, SVD = 2.07 ± 1.44 dB). However, we pair this finding with a note of caution regarding two weaknesses of image quality measures for adaptive beamforming.

As described by Rindal and others, we first recognize that image contrast is sensitive to dynamic range transformations [159, 160]. CFPD images portray the normalized coherence of the echo data, which does not scale linearly with echo power. Therefore, quantitative comparison between CFPD and power Doppler contrast may be complicated by non-linear dynamic range bias. In recent literature, several techniques have been proposed to enable fairer comparison between conventional and adaptive beamformers for B-mode (tissue) applications. One such method is histogram matching, wherein images containing varied dynamic ranges are transformed to a consistent scale [160]. However, a limitation of histogram matching for blood flow applications arises when the adaptive and conventional images exhibit different image features; For example, low velocity blood flow that is obscured in power Doppler may be uncovered due to improved rejection of tissue or acoustic clutter. For blood flow imaging, there remains an unsolved need for robust, invariant measures of clinical image quality.

A potential solution for adaptive imaging is the generalized contrast-to-noise ratio,

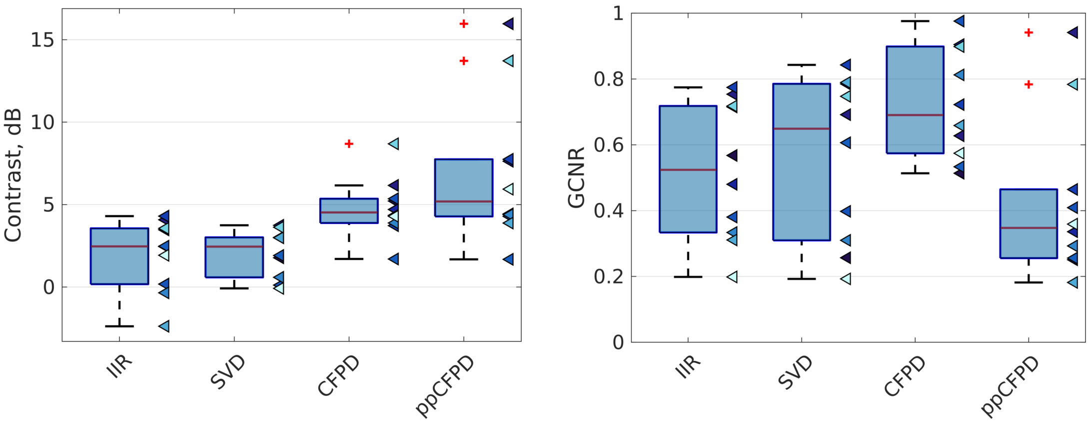

Figure 4.11: Pre-TACE tumor-to-background contrast (*left*) and GCNR (*right*) metrics. Subjects 7 and 13 were excluded due to the presence of dark-region artifacts that obscured perception of tumor blood flow.

which is a scale-invariant metric that can be used to assess vessel detectability [100]. As shown in Figure 4.11, we observe that CFPD yields a higher GCNR than power Doppler, which indicates improved discrimination (CFPD = 0.72 ± 0.17, PD + IIR = 0.52 ± 0.21, PD + SVD = 0.56 ± 0.25). In comparison, ppCFPD performed slightly worse than PD with SVD with a difference in GCNR of 0.44 ± 0.25 dB.

The disparity between ppCFPD contrast and GCNR performance demonstrates a second weakness of the adaptive beamformers in the current study. Adaptive beamformers, including ppCFPD and CFPD, are susceptible to the formation of 'dark-region' artifacts [103]. Dark-region artifacts occur during adaptive beamforming when the imaging field of view contains hyperechoic structures which produce strong off-axis scattering. Off-axis

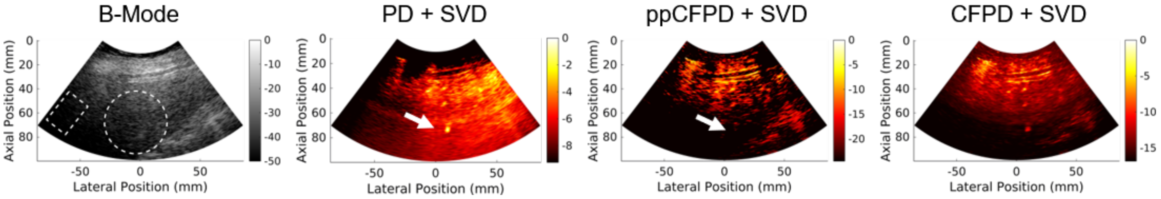

Figure 4.12: Subject 13 exhibits a dark-region artifact that obscures visualization of blood flow at the tumor site. For ppCFPD, dark-region artifacts manifest as negative pixels, which are set to zero. For CFPD, dark region artifacts degrade coherence measures and result in lower contrast.

signals result in negative coherence measures, which decrease contrast and affect visualization of blood flow, as shown in Figure 4.12. For ppCFPD, negative pixel values are set to zero, so dark region artifacts present as image dropout. Since CFPD pixel intensity is positive-valued, image drop out does not occur, but coherence measures are likely degraded.

As performed for other adaptive beamformers, negative pixel values are not considered for ppCFPD image quality metrics. Under the assumption of additive noise, the ppCFPD background pixel intensity is expected to follow a zero-mean Gaussian distribution. Thus, roughly half of the noise pixels are expected to fall below zero; however, the presence of dark-region artifacts decreases the proportion of excluded background pixels, which degrades metric computation. In addition, strong off-axis scattering can cause signal-bearing regions to produce negative coherence values, resulting in drop-out in areas of blood flow.

The channel data degradation likely arises from a number of factors, including acoustic clutter (*e.g.* off-axis scattering and reverberation), phase aberration, and attenuation from cirrhotic liver parenchyma. Channel-based processing methods, such as ADMIRE or HOSVD filtering, may aid in reducing acoustic clutter [51, 105]. Similarly, methods that operate across transmit angles, rather than across channels, have been proposed for aberration correction and coherence computations [107, 161].

Figure 4.13 demonstrates initial feasibility of applying an HOSVD filter to reduce ppCFPD image drop-out. The SVD-filtered ppCFPD image preserves conspicuous vasculature within the tumor region, but areas of low-intensity enhancement are suppressed. Enhancement at the tumor site is expected to correspond to unresolvable blood flow, which may be valuable for assessment of TACE [27]. Figure 4.13 displays the histogram of pixels within the background ROI for Subject 2, where the pixels are observed to be skewed toward negative values. To reduce this effect, an HOSVD filter was implemented with three upper cutoffs along the temporal, channel, and spatial dimensions [105]. Matching SVD, a 40 Hz cutoff was employed to choose the temporal cutoff. The spatial cutoff was

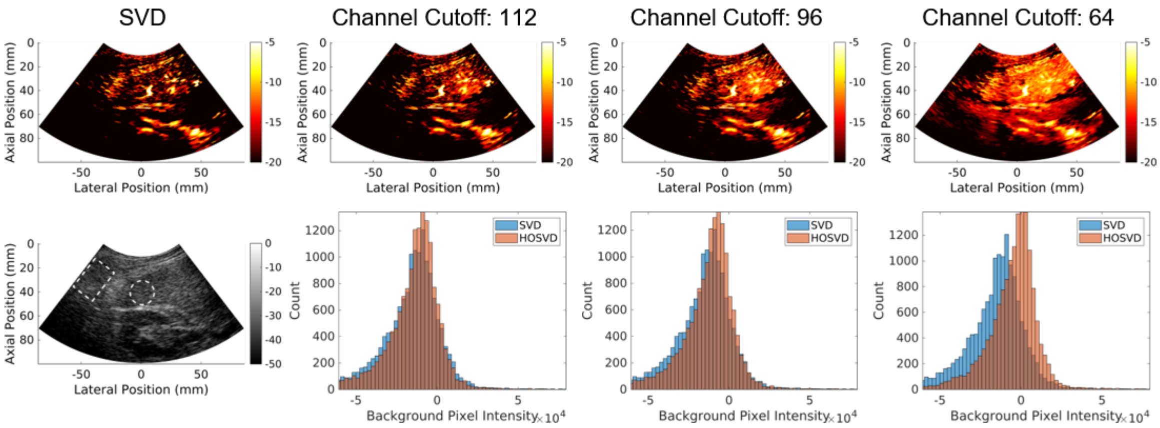

Figure 4.13: A ppCFPD image formed with SVD filtering (*column 1*) compared to ppCFPD images formed with HOSVD filtering (*columns 2-4*). The ppCFPD images suffered from dark region artifacts, which cause negative pixel values. HOSVD filtering increased image coherence, resulting in higher pixel intensities. However, greater rejection of channel singular vectors with HOSVD (*increasing left to right*) resulted in rejection of background noise and affected image contrast.

empirically selected. Images were formed using three channel cutoffs (64, 96, or 112) to reject noise and off-axis scattering within the higher rank vectors. Rejection of channel components using an HOSVD filter improved image coherence, and may be valuable for preservation of unresolvable blood flow.

In future work, a straightforward approach to improve the quality of the channel data is to modify the transmit angle sequence. Plane wave imaging sequences invoke a trade-off between frame rate, resolution, and contrast [58]. Image resolution is determined by the angular span; however, the number and inter-transmit angular spacing affect the image contrast. Sparse angular sequences introduce grating lobes, which degrade the channel coherence. For future work, a smaller angular span is recommended. As shown in Figure 4.14, employing an acquisition sequence with 9 angles spaced between -4 and 4 degrees, rather than -8 and 8 degrees, improves the channel quality without lowering frame rate.

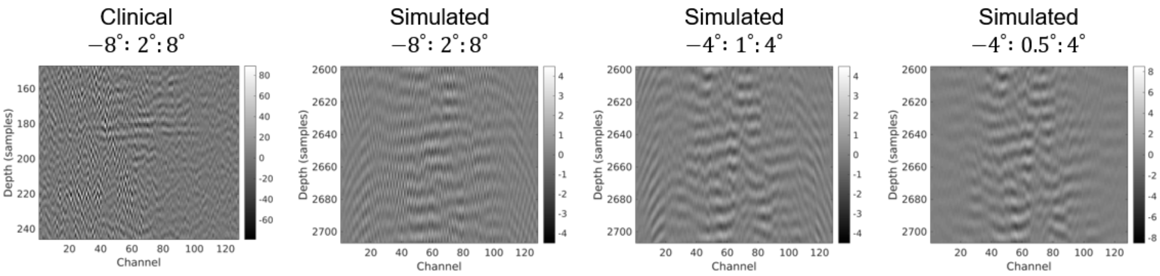

Figure 4.14: Example of filtered, delayed channel data from Subject 2 that is degraded by strong off-axis signals. As demonstrated using Field II simulations, the use of a smaller angle span or greater number of angles improves the appearance of the channel data.

4.6 Conclusions

This pilot study demonstrates that power Doppler imaging with advanced processing methods may be used to differentiate complete and incomplete therapy immediately after TACE. Using power Doppler imaging, we demonstrate that the change in contrast between pre-TACE and post-TACE images was indicative of procedural outcome. Advanced image processing methods, including adaptive ensemble selection, noise equalization, and SVD filtering, improved sensitivity to low velocity tumoral flow by (1) improving the tumor-to-background contrast and (2) improving rejection of the tissue signal. Challenges and considerations for aperture domain processing are addressed.

Adaptive selection of the imaging ensemble using the spatiotemporal coherence produced fewer tissue artifacts. Regions of high spatiotemporal coherence exhibit improved tissue stationarity, which improves separation of tissue and low velocity blood flow during filtering. In this work, the spatiotemporal coherence was employed to optimize retrospective ensemble selection from datasets containing 2 seconds of data. However, several datasets produced insufficient rejection of the tissue data due to excess motion. During the TACE procedure, the subject is under mild sedation and may experience difficulty breath-holding due to discomfort. Spatiotemporal coherence could be a potential solution for intraoperative assessment of data quality, and should be considered during real-time imaging.

Similarly, the use of noise equalization yielded improved tumor-to-background contrast and improved homogeneity of the noise floor. We note that noise equalization does not directly change the intrinsic separation between the blood signal and the noise floor, but improves the dynamic range of small vessels. Noise equalization reduces intensity bias caused by TGC and other processing, which enabled the TACE-induced changes in blood flow to be detected using the change in contrast, a relative measure. Direct measurement of the change in blood echo power, which scales linearly with blood volume, is compromised by factors including the field-of-view and cardiac cycle. In future work, the change in power could be considered by EKG gating and by fixing the probe during TACE to ensure a consistent field-of-view.

Both SVD and IIR filtering yielded sufficient rejection of the tissue signal to permit TACE-induced changes in blood flow to be observed. The SVD filter produced better rejection of tissue clutter than the IIR filter, likely due to adaptive basis generation and blockwise processing. Filtering efficacy was likely improved by the application of adaptive demodulation to reduce axial motion as described by Tierney *et al.*[79]. A 2D motion correction algorithm, such as speckle tracking, could further address rotational and lateral translation.

The aperture domain processing improved visualization of coherent signals, such as conspicuous vasculature, but was limited by aperture data degradation. This work demonstrates that CFPD and ppCFPD can detect low velocity blood flow in liver tumors, but additional studies are needed to assess if sensitivity is retained for perfusion-level (*e.g.* sub-resolution) flow. A primary limitation of this study is that strong off-axis scattering resulted in the presence of dark-region artifacts that compromised measurement of image contrast. The application of channel-based filtering methods, such as HOSVD, may address these limitations. Since CFPD image intensity does not scale with the blood echo power, alternative measures of vessel detection, such as a reader study, may also be considered.

For future work, transmit sequence design should be considered, including the number and span of steering angles. The use of smaller inter-angle spacing may reduce the presence of grating lobes and improve coherence estimation. In addition, methods to synthetically increase the number or span of the transmissions could be applied to increase the signal-to-noise level of the data. In addition, the development of real-time power Doppler imaging via GPU and parallel processing would improve data collection and enable more robust assessment of the proposed processing methods.

Non-contrast power Doppler is a potential solution for immediate evaluation of therapeutic response during TACE procedures. In combination with adaptive filtering, motion compensation, and noise equalization, power Doppler is sensitive to changes in low velocity blood flow. In addition, we demonstrate preliminary feasibility of using coherence-based imaging methods to improve detection of conspicuous tumor blood vessels in cluttered environments. The findings of this pilot study indicate that power Doppler can be used to detect residual vascularity and differentiate therapeutic outcome after TACE.

Chapter 5

Conclusions and Future Work

This thesis presents aperture domain methods to improve visualization of low velocity blood flow in challenging imaging environments. The clinical objective of this work was to improve evaluation of residual blood flow following TACE procedures, which may lead to improved identification of collateral feeder vasculature, earlier retreatment of recurrent lesions, and improve procedural outcomes. Non-contrast power Doppler ultrasound is an attractive modality for TACE evaluation because it eliminates the need to intravenously administer contrast and reduces radiation exposure. The primary barriers for ultrasound evaluation of blood flow in liver lesions, as well as other deep imaging targets, are insufficient signal separation and inadequate signal-to-noise ratio [41]. We proposed two technologies that address these barriers and potentially facilitate earlier evaluation of TACE efficacy.

The first contribution of this thesis was developing a coherence-based beamforming method, termed power-preserving Coherent Flow Power Doppler (ppCFPD). This method is a modified form of CFPD that employs spatial coherence to suppress clutter, while retaining proportionality between image intensity and the fractional moving blood volume. In addition, a theoretical bound was devised to enable adaptive thresholding to remove remaining spurious noise. Validation was performed using simulated, phantom, and *in vivo* data.

In Chapter 2, ppCFPD was shown to improve image quality in experimental data. This work is the first example of a spatial coherence beamforming method that can preserve a linear imaging response toward the echo power. This outcome addresses a primary limitation of CFPD imaging, which has a non-linear imaging response that is dependent on the SNR and flat with respect to echo power. As a result, CFPD is appropriate for anatomical or feature detection tasks, but not quantitative or semi-quantitative assessment [84]. We demonstrate that ppCFPD is sensitive toward changes in blood signal power, which is proportional to the blood volume; thus, ppCFPD may be well-suited for perfusion imaging applications.

Future work may be performed to further characterize the ppCFPD parameters. The coherence measure is estimated by averaging the covariance for short lag values, which aligns with SLSC and CFPD imaging. The rationale for using short lag values is that the coherence of blood is readily separable from incoherent clutter and noise. However, lateral resolution improves with an increasing maximum lag, which may be valuable for small vessel imaging. Similarly, the application of an axial kernel improves the covariance estimate for ppCFPD imaging, but reduces the axial resolution. In this thesis, the maximum lag value and kernel sizes are only studied in a limited scope, and may be further optimized.

In addition, additional study is necessary to validate ppCFPD for clinical imaging of microvascular flow. Low velocity blood flow is typically associated with small-diameter vessels, including arterioles, venules, and capillaries. Prior work in the lab and by others has suggested that sub-resolution blood flow may appear on Doppler imaging as a haze, rather than as discrete vessels [27, 34]. Validation of ppCFPD and the thresholding technique were performed using single vessel simulations, which are not representative of true microvascular flow. Additional research is needed to determine the feasibility and imaging characteristics of applying ppCFPD to visualize sub-resolution blood flow.

A limitation for ppCFPD imaging is the potential to develop ‘dark region artifacts’, which are regions of drop-out adjacent to bright targets [103]. Since ppCFPD employs a measure of covariance between channels, strong off-axis echoes manifest as negative pixel values. Dark region artifacts compromise vessel detection and quantitative measures, as low-amplitude blood flow may be obscured. One potential solution to mitigate dark region artifacts is to pre-process the delayed channel data using a channel-dimension filter to remove strong off-axis contributions. As shown in Chapter 2, aperture domain features could be leveraged using an HOSVD or SVD filter.

The second contribution of this thesis was establishing a framework for higher-order singular value decomposition (HOSVD) filtering of aperture data. The efficacy of this technique compared to SVD filtering was demonstrated using simulated and *in vivo* data. Further, we studied the novel application of an SVD filter to aperture data for further comparison. Finally, both technologies were successfully applied to clinical data and preliminary feasibility was shown for using HOSVD to improve visualization of residual blood flow after TACE.

A shortcoming of the current filtering framework is that the spatial dimension classifier is sensitive to spatially-variant imaging features, such as depth-dependent gain or inhomogeneous tissue regions. Although the classifier worked well in simulation and for initial *in vivo* liver imaging, it was not robust when applied to the TACE data. This is likely due to factors such as cirrhosis and field-of-view heterogeneity in the TACE data, which are not considered in the proposed classifier. In addition, the TACE data employed different imaging parameters and filter implementation, as the TACE data focused on larger fields-of-view, blockwise processing, and longer ensembles. The dimensions of the aperture data tensor affect subspace distribution across singular values and singular vectors. For example, the effect of sample size on noise-bearing singular values is modelled by the Marcenko-Pastur distribution [120]. In addition, factors including aperture-based effects (aberration, reverberation, off-axis signals), complex motion (tissue compression, out-of-frame motion), and varied field of view (cirrhosis, multiple vessels) likely affect estimation of the Nakagami parameters. A variety of alternative cutoff methods have been proposed for SVD and HOSVD filtering. These methods include manual (*e.g.* defined number of singular vectors), parameterized (*e.g.* based on frequency or singular value magnitude), and automated (*e.g.* spatial correlation matrix) techniques.

Clinical adoption of HOSVD filtering will primarily be limited by its associated computational burden. As described in Chapter 3, implementing the HOSVD filter incurs substantially greater computational cost than a conventional SVD filter. This burden may be reduced through the use of parallel computing or GPU processing, which could enable real-time or more efficient processing. Alternatively, we note that the classifier features proposed for the HOSVD filter could be applied to other SVD or blind-source-separation frameworks. We have demonstrated that an SVD filter can be applied to a casorati matrix of aperture data, and have proposed efficient projection-based techniques as well.

Lastly, the work presented in Chapter 4 demonstrates the feasibility of using non-contrast ultrasound to evaluate tumor vascular response after TACE therapy. This work extends a prior study that demonstrated that non-contrast ultrasound is sensitive to suppression of blood flow incurred by TACE [27]. In this thesis, non-contrast ultrasound was combined with adaptive demodulation, aperture domain beamforming, noise equalization, and adaptive ensemble selection. These methods were shown to improve flow detection in clinical data, as characterized by image quality and a novel reader assessment. The use of noise equalization removed the depth-dependent effects of time-gain compensation, which enabled a novel assessment of tumor power. In addition, the use of a temporal correlation measure for ensemble selection further illustrates the benefit of adaptive demodulation for low-velocity blood flow imaging.

The advantage of using ultrasound for post-operative assessment of TACE is the capacity for immediate evaluation before the patient leaves the operating suite. Conventional evaluation of therapeutic efficacy using MRI or CT cannot be performed until 4-6 weeks post-treatment [8, 10, 16]; similarly, contrast-enhanced ultrasound is susceptible to artifacts until 1-2 days post-treatment [18, 23]. Re-treatment of lesions that exhibit recurrence or residual tumor burden is performed ‘on-demand’ based on follow-up imaging [8, 11, 15]. Multiple sessions are frequently used to maximize chemoembolization response; however, repeated TACE can be detrimental to liver and vascular function [162]. Immediate follow-up would allow the clinician to re-treat residual tumor within a single TACE treatment, which would likely improve therapeutic efficacy and improve patient outcomes.

Future work will further validate the pilot study discussed in Chapter 4 to characterize the relationship between post-TACE ultrasound findings and patient outcomes. Future recruitment will focus on patients with intermediate-stage hepatocellular carcinoma, which often presents with hypervascularity at the tumor site. Continuation of this clinical study will permit comparison between ultrasound and follow-up MRI/CT, evaluation of image quality based on tumor size and location, and measurement of time-to-progression. The relationship between ultrasound findings and treatment efficacy will be determined using a Cox Proportional Hazard model. In addition, further research may consider the implications of tumor vessel morphology, the tortuosity, size, and density of tumoral vessels may influence therapeutic delivery.

In addition, work will be performed to further develop post-processing methods and improve the acquisition sequence. Since the acquisition frame rate is limited by the number of angles, one focus of improvement may be adjusting the spacing of the angular sequence. Using a sparse angle sequence incurs grating lobes, so using a tighter spacing and smaller total angular span would improve contrast resolution [58]. In addition, the development of real-time processing and display of power Doppler images would improve data acquisition, particularly for deep lesions. The development of real-time processing and independent component analysis (ICA) clutter filtering is ongoing work that will enable improved study of low-velocity and perfusion-level flow [163–165]. The methods presented in this thesis are also complimentary with other techniques developed in the lab, such as Aperture Domain Model Image REconstruction (ADMIRE) [166–168], deep learning methods for clutter rejection [169, 170], and coded transmit sequences for increased imaging SNR [171].

The application of ultrasound imaging to evaluate changes in blood flow after TACE additionally supports research to optimize TACE embolization endpoints. A deficiency of the TACE procedure is the lack of an objective endpoint metric to assess the degree of embolization achieved [172]. Procedural completion is evidenced by qualitative presentation of digital subtraction angiography, characterized by decreased contrast diffusion within the target region and contrast backflow. Angiographic studies suggest that embolization to a substasis antegrade flow produces a greater treatment benefit, in comparison to full-stasis endpoints [173]. Overall, TACE outcomes remain mixed with complete or partial response achieved reported as (51-76%), in part due to varied levels of embolization achieved [9–13]. In particular, tumors supported by multiple vessels have a lower response rate, as feeding vessels outside of the region of contrast diffusion may not be detected with DSA [174]. Since Power Doppler and ppCFPD are indicative of the fractional moving blood volume, ultrasound may be an effective modality to measure the degree of arterial stasis. Additionally, ultrasound-based assessment is well-suited for clinical adoption in comparison to other modalities, as it is portable and does not require specialized operating suites.

Beyond TACE, this work has broader applications for functional and therapeutic assessment. TACE is an appealing clinical application for the development and validation of flow imaging methods due to its controlled nature and potential for clinical benefit. However, several other therapies for the treatment of hepatocellular carcinoma could benefit from perfusion evaluation, including transarterial radioembolization (TARE), 'bland' transarterial embolization (TAE), and radiofrequency ablation. These methods comparably involve ablation or embolization to reduce tumor viability, and could benefit from ultrasonic blood flow imaging for navigation or treatment evaluation. Numerous other clinical ultrasound applications are limited or degraded by acoustic clutter, such as functional neuroimaging, which could also benefit from the aperture domain methods presented in this thesis.

In conclusion, this thesis presents the development, validation, and clinical assessment of two aperture domain technologies to improve blood flow imaging in poor imaging environments. This work addresses two limitations of Doppler imaging, poor SNR and insufficient signal-separation, which limit clinical evaluation of low-velocity blood flow using ultrasound. In Chapter 2, an aperture domain beamforming method is presented improves image quality by rejecting acoustic clutter sources. In Chapter 3, a higher-order singular value decomposition filter is proposed that operates on a tensor of aperture data for greater suppression of clutter and noise signals. These technologies are shown to overcome clinical barriers and enable non-contrast ultrasound assessment during TACE procedures. Overall, this work demonstrates the value of aperture domain methods and motivates future study of filtering and beamforming methods.

REFERENCES

[1] S. J. Henley, E. M. Ward, S. Scott, J. Ma, R. N. Anderson, A. U. Firth, C. C. Thomas, F. Islami, H. K. Weir, D. R. Lewis *et al.*, “Annual report to the nation on the status of cancer, part i: national cancer statistics,” *Cancer*, vol. 126, no. 10, pp. 2225–2249, 2020.

[2] D. Anwanwan, S. K. Singh, S. Singh, V. Saikam, and R. Singh, “Challenges in liver cancer and possible treatment approaches,” *Biochimica et Biophysica Acta (BBA)-Reviews on Cancer*, vol. 1873, no. 1, p. 188314, 2020.

[3] A. G. Singal, A. Pillai, and J. Tiro, “Early detection, curative treatment, and survival rates for hepatocellular carcinoma surveillance in patients with cirrhosis: a meta-analysis,” *PLoS Med*, vol. 11, no. 4, p. e1001624, 2014.

[4] Y.-T. Lee, J. J. Wang, M. Luu, M. Noureddin, K. Kosari, V. G. Agopian, N. E. Rich, S. C. Lu, H.-R. Tseng, N. N. Nissen *et al.*, “The mortality and overall survival trends of primary liver cancer in the united states,” *JNCI: Journal of the National Cancer Institute*, 2021.

[5] J. M. Llovet, C. Brú, and J. Bruix, “Prognosis of hepatocellular carcinoma: the bclc staging classification,” in *Seminars in liver disease*, vol. 19. © 1999 by Thieme Medical Publishers, Inc., 1999, pp. 329–338.

[6] E. A. F. T. S. O. T. Liver *et al.*, “Easl clinical practice guidelines: management of hepatocellular carcinoma,” *Journal of hepatology*, vol. 69, no. 1, pp. 182–236, 2018.

[7] V. Mazzaferro, S. Bhoori, C. Sposito, M. Bongini, M. Langer, R. Miceli, and L. Mariani, “Milan criteria in liver transplantation for hepatocellular carcinoma: an evidence-based analysis of 15 years of experience,” *Liver transplantation*, vol. 17, no. S2, pp. S44–S57, 2011.

[8] T. Chemoembolization, “Quality improvement guidelines for transarterial chemoembolization and embolization of hepatic malignancy,” *J Vasc Interv Radiol*, vol. 28, pp. 1210–1223, 2017.

[9] K. Malagari, M. Pomoni, H. Moschouris, E. Bouma, J. Koskinas, A. Stefaniotou, A. Marinis, A. Kelekis, E. Alexopoulou, A. Chatziioannou *et al.*, “Chemoembolization with doxorubicin-eluting beads for unresectable hepatocellular carcinoma: five-year survival analysis,” *Cardiovascular and interventional radiology*, vol. 35, no. 5, pp. 1119–1128, 2012.

[10] H.-D. Kim, J. An, J. H. Kim, D. I. Gwon, J. H. Shin, G.-Y. Ko, H.-K. Yoon, K.-B. Sung, K. M. Kim, and H. C. Lee, “Impact of the interval between transarterial chemoembolization sessions on survival in patients with unresectable hepatocellular carcinoma,” *Journal of Vascular and Interventional Radiology*, vol. 27, no. 4, pp. 504–513, 2016.

[11] E. Terzi, R. Golfieri, F. Piscaglia, M. Galassi, A. Dazzi, S. Leoni, E. Giampalma, M. Renzulli, and L. Bolondi, "Response rate and clinical outcome of hcc after first and repeated ctace performed "on demand"," *Journal of hepatology*, vol. 57, no. 6, pp. 1258–1267, 2012.

[12] R. Lencioni, T. de Baere, M. C. Soulen, W. S. Rilling, and J.-F. H. Geschwind, "Lipiodol transarterial chemoembolization for hepatocellular carcinoma: a systematic review of efficacy and safety data," *Hepatology*, vol. 64, no. 1, pp. 106–116, 2016.

[13] N. Haywood, K. Gennaro, J. Obert, P. F. Sauer, D. T. Redden, J. Zarzour, J. K. Smith, D. Bolus, S. Saddekni, A. K. A. Aal *et al.*, "Does the degree of hepatocellular carcinoma tumor necrosis following transarterial chemoembolization impact patient survival?" *Journal of oncology*, vol. 2016, 2016.

[14] R. J. Lewandowski, D. Wang, J. Gehl, B. Atassi, R. K. Ryu, K. Sato, A. A. Nemcek Jr, F. H. Miller, M. F. Mulcahy, L. Kulik *et al.*, "A comparison of chemoembolization endpoints using angiographic versus transcatheter intraarterial perfusion/mr imaging monitoring," *Journal of Vascular and Interventional Radiology*, vol. 18, no. 10, pp. 1249–1257, 2007.

[15] W. Sieghart, F. Hucke, M. Pinter, I. Graziadei, W. Vogel, C. Müller, H. Heinzl, M. Trauner, and M. Peck-Radosavljevic, "The art of decision making: retreatment with transarterial chemoembolization in patients with hepatocellular carcinoma," *Hepatology*, vol. 57, no. 6, pp. 2261–2273, 2013.

[16] N. Voizard, M. Cerny, A. Assad, J.-S. Billiard, D. Olivié, P. Perreault, A. Kielar, R. K. Do, T. Yokoo, C. B. Sirlin *et al.*, "Assessment of hepatocellular carcinoma treatment response with li-rads: a pictorial review," *Insights into imaging*, vol. 10, no. 1, pp. 1–22, 2019.

[17] R. Lencioni and J. M. Llovet, "Modified recist (mrecist) assessment for hepatocellular carcinoma," in *Seminars in liver disease*, vol. 30. © Thieme Medical Publishers, 2010, pp. 052–060.

[18] K. Nam, M. Stanczak, A. Lyshchik, P. Machado, Y. Kono, F. Forsberg, C. M. Shaw, and J. R. Eisenbrey, "Evaluation of hepatocellular carcinoma transarterial chemoembolization using quantitative analysis of 2d and 3d real-time contrast enhanced ultrasound," *Biomedical physics & engineering express*, vol. 4, no. 3, p. 035039, 2018.

[19] J. Wang, J.-J. Cheng, K.-Y. Huang, Z.-G. Zhuang, X.-B. Zhang, J.-C. Chi, X.-L. Hua, and J.-R. Xu, "Quantitative assessment of angiographic perfusion reduction using color-coded digital subtraction angiography during transarterial chemoembolization," *Abdominal Radiology*, vol. 41, no. 3, pp. 545–552, 2016.

[20] Y.-J. Ho, M.-B. Chang, Y.-H. Lin, C.-H. Yao, and T.-C. Huang, "Quantitative portal vein velocity of liver cancer patients with transcatheter arterial chemoembolization on angiography," *The Scientific World Journal*, vol. 2012, 2012.

[21] J. Iwazawa, S. Ohue, T. Mitani, H. Abe, N. Hashimoto, M. Hamuro, and K. Nakamura, "Identifying feeding arteries during tace of hepatic tumors: comparison of c-arm ct and

digital subtraction angiography," *American Journal of Roentgenology*, vol. 192, no. 4, pp. 1057–1063, 2009.

[22] I. Oezdemir, C. E. Wessner, C. Shaw, J. R. Eisenbrey, and K. Hoyt, "Tumor vascular networks depicted in contrast-enhanced ultrasound images as a predictor for transarterial chemoembolization treatment response," *Ultrasound in medicine & biology*, vol. 46, no. 9, pp. 2276–2286, 2020.

[23] C. M. Shaw, J. R. Eisenbrey, A. Lyshchik, P. L. O'Kane, D. A. Merton, P. Machado, L. Pino, D. B. Brown, and F. Forsberg, "Contrast-enhanced ultrasound evaluation of residual blood flow to hepatocellular carcinoma after treatment with transarterial chemoembolization using drug-eluting beads: A prospective study," *Journal of Ultrasound in Medicine*, vol. 34, no. 5, pp. 859–867, 2015.

[24] H. Moschouris, K. Malagari, M. G. Papadaki, I. Kornezos, P. Gkoutzios, N. Tepelenis, and D. Matsaidonis, "Short-term evaluation of liver tumors after transarterial chemoembolization: limitations and feasibility of contrast-enhanced ultrasonography," *Abdominal imaging*, vol. 36, no. 6, pp. 718–728, 2011.

[25] K. Kubota, N. Hisa, Y. Fujiwara, M. Fukumoto, D. Yoshida, and S. Yoshida, "Evaluation of the intratumoral vasculature of hepatocellular carcinoma by power doppler sonography: advantages and disadvantages versus conventional color doppler sonography," *Abdominal imaging*, vol. 25, no. 2, pp. 172–178, 2000.

[26] K. Kubota, N. Hisa, T. Nishikawa, Y. Fujiwara, Y. Murata, S. Itoh, D. Yoshida, and S. Yoshida, "Evaluation of hepatocellular carcinoma after treatment with transcatheter arterial chemoembolization: comparison of lipiodol-ct, power doppler sonography, and dynamic mri," *Abdominal imaging*, vol. 26, no. 2, pp. 184–190, 2001.

[27] J. Tierney, J. Baker, A. Borgmann, D. Brown, and B. Byram, "Non-contrast power doppler ultrasound imaging for early assessment of trans-arterial chemoembolization of liver tumors," *Scientific reports*, vol. 9, no. 1, pp. 1–12, 2019.

[28] T. L. Szabo, *Diagnostic ultrasound imaging: inside out*. Academic Press, 2004.

[29] J. A. Jensen, "A model for the propagation and scattering of ultrasound in tissue," *The Journal of the Acoustical Society of America*, vol. 89, no. 1, pp. 182–190, 1991.

[30] G. D. Ludwig, "The velocity of sound through tissues and the acoustic impedance of tissues," *The journal of the acoustical society of America*, vol. 22, no. 6, pp. 862–866, 1950.

[31] T. Loupas, J. Powers, and R. W. Gill, "An axial velocity estimator for ultrasound blood flow imaging, based on a full evaluation of the doppler equation by means of a two-dimensional autocorrelation approach," *IEEE transactions on ultrasonics, ferroelectrics, and frequency control*, vol. 42, no. 4, pp. 672–688, 1995.

[32] C. Kasai, K. Namekawa, A. Koyano, and R. Omoto, “Real-time two-dimensional blood flow imaging using an autocorrelation technique,” *IEEE Transactions on sonics and ultrasonics*, vol. 32, no. 3, pp. 458–464, 1985.

[33] G. F. Pinton, J. J. Dahl, and G. E. Trahey, “Rapid tracking of small displacements with ultrasound,” *IEEE transactions on ultrasonics, ferroelectrics, and frequency control*, vol. 53, no. 6, pp. 1103–1117, 2006.

[34] J. M. Rubin, R. O. Bude, P. L. Carson, R. L. Bree, and R. S. Adler, “Power doppler us: a potentially useful alternative to mean frequency-based color doppler us.” *Radiology*, vol. 190, no. 3, pp. 853–856, 1994.

[35] K. K. Shung, R. A. Sigelmann, and J. M. Reid, “Scattering of ultrasound by blood,” *IEEE Transactions on Biomedical Engineering*, vol. 23, no. 6, pp. 460–467, 1976.

[36] M. Imbault, D. Chauvet, J.-L. Gennisson, L. Capelle, and M. Tanter, “Intraoperative functional ultrasound imaging of human brain activity,” *Scientific reports*, vol. 7, no. 1, pp. 1–7, 2017.

[37] E. Macé, G. Montaldo, I. Cohen, M. Baulac, M. Fink, and M. Tanter, “Functional ultrasound imaging of the brain,” *Nature methods*, vol. 8, no. 8, pp. 662–664, 2011.

[38] Y.-Y. Kim, C. An, K. S. A. Do Young Kim, J.-Y. Choi, and M.-J. Kim, “Failure of hepatocellular carcinoma surveillance: inadequate echogenic window and macronodular parenchyma as potential culprits,” *Ultrasonography*, vol. 38, no. 4, p. 311, 2019.

[39] O. Simmons, D. T. Fetzer, T. Yokoo, J. A. Marrero, A. Yopp, Y. Kono, N. Parikh, T. Browning, and A. G. Singal, “Predictors of adequate ultrasound quality for hepatocellular carcinoma surveillance in patients with cirrhosis,” *Alimentary pharmacology & therapeutics*, vol. 45, no. 1, pp. 169–177, 2017.

[40] R. F. Hanna, V. Z. Miloushev, A. Tang, L. A. Finklestone, S. Z. Brejt, R. S. Sandhu, C. S. Santillan, T. Wolfson, A. Gamst, and C. B. Sirlin, “Comparative 13-year meta-analysis of the sensitivity and positive predictive value of ultrasound, ct, and mri for detecting hepatocellular carcinoma,” *Abdominal Radiology*, vol. 41, no. 1, pp. 71–90, 2016.

[41] H.-J. Kang, J. M. Lee, S. K. Jeon, H. Ryu, J. Yoo, J. K. Lee, and J. K. Han, “Microvascular flow imaging of residual or recurrent hepatocellular carcinoma after transarterial chemoembolization: comparison with color/power doppler imaging,” *Korean journal of radiology*, vol. 20, no. 7, p. 1114, 2019.

[42] F. Viola and W. F. Walker, “A comparison of the performance of time-delay estimators in medical ultrasound,” *IEEE transactions on ultrasonics, ferroelectrics, and frequency control*, vol. 50, no. 4, pp. 392–401, 2003.

[43] M. Bayat, M. Fatemi, and A. Alizad, “Background removal and vessel filtering of noncontrast ultrasound images of microvasculature,” *IEEE Transactions on Biomedical Engineering*, vol. 66, no. 3, pp. 831–842, 2018.

[44] C. Huang, P. Song, P. Gong, J. D. Trzasko, A. Manduca, and S. Chen, "Debiasing-based noise suppression for ultrafast ultrasound microvessel imaging," *IEEE transactions on ultrasonics, ferroelectrics, and frequency control*, vol. 66, no. 8, pp. 1281–1291, 2019.

[45] Y. L. Li, D. Hyun, L. Abou-Elkacem, J. K. Willmann, and J. J. Dahl, "Visualization of small-diameter vessels by reduction of incoherent reverberation with coherent flow power doppler," *IEEE transactions on ultrasonics, ferroelectrics, and frequency control*, vol. 63, no. 11, pp. 1878–1889, 2016.

[46] S. Flax and M. O'Donnell, "Phase-aberration correction using signals from point reflectors and diffuse scatterers: Basic principles," *IEEE transactions on ultrasonics, ferroelectrics, and frequency control*, vol. 35, no. 6, pp. 758–767, 1988.

[47] J. J. Dahl, D. A. Guenther, and G. E. Trahey, "Adaptive imaging and spatial compounding in the presence of aberration," *IEEE transactions on ultrasonics, ferroelectrics, and frequency control*, vol. 52, no. 7, pp. 1131–1144, 2005.

[48] B. Byram and J. Shu, "Pseudononlinear ultrasound simulation approach for reverberation clutter," *Journal of Medical Imaging*, vol. 3, no. 4, p. 046005, 2016.

[49] G. Pinton, G. Trahey, and J. Dahl, "Characteristics of the spatial coherence function from backscattered ultrasound with phase aberration and reverberation clutter," in *2011 IEEE International Ultrasonics Symposium.* IEEE, 2011, pp. 684–687.

[50] J. J. Dahl and N. M. Sheth, "Reverberation clutter from subcutaneous tissue layers: Simulation and in vivo demonstrations," *Ultrasound in medicine & biology*, vol. 40, no. 4, pp. 714–726, 2014.

[51] B. Byram, J. Shu, and K. Dei, "Nonlinear beamforming of aperture domain signals," in *2015 IEEE International Ultrasonics Symposium (IUS).* IEEe, 2015, pp. 1–6.

[52] M. A. Lediju, G. E. Trahey, B. C. Byram, and J. J. Dahl, "Short-lag spatial coherence of backscattered echoes: Imaging characteristics," *IEEE transactions on ultrasonics, ferroelectrics, and frequency control*, vol. 58, no. 7, pp. 1377–1388, 2011.

[53] A. Heimdal and H. Torp, "Ultrasound doppler measurements of low velocity blood flow: Limitations due to clutter signals from vibrating muscles," *IEEE transactions on ultrasonics, ferroelectrics, and frequency control*, vol. 44, no. 4, pp. 873–881, 1997.

[54] S. Bjaerum, H. Torp, and K. Kristoffersen, "Clutter filter design for ultrasound color flow imaging," *IEEE transactions on ultrasonics, ferroelectrics, and frequency control*, vol. 49, no. 2, pp. 204–216, 2002.

[55] ——, "Clutter filters adapted to tissue motion in ultrasound color flow imaging," *IEEE transactions on ultrasonics, ferroelectrics, and frequency control*, vol. 49, no. 6, pp. 693–704, 2002.

[56] C. Alfred and L. Lovstakken, “Eigen-based clutter filter design for ultrasound color flow imaging: A review,” *IEEE transactions on ultrasonics, ferroelectrics, and frequency control*, vol. 57, no. 5, pp. 1096–1111, 2010.

[57] C. Demené, T. Deffieux, M. Pernot, B.-F. Osmanski, V. Biran, J.-L. Gennisson, L.-A. Sieu, A. Bergel, S. Franqui, J.-M. Correas *et al.*, “Spatiotemporal clutter filtering of ultrafast ultrasound data highly increases doppler and fultrasound sensitivity,” *IEEE transactions on medical imaging*, vol. 34, no. 11, pp. 2271–2285, 2015.

[58] B. Denarie, T. A. Tangen, I. K. Ekroll, N. Rolim, H. Torp, T. Bjåstad, and L. Lovstakken, “Coherent plane wave compounding for very high frame rate ultrasonography of rapidly moving targets,” *IEEE transactions on medical imaging*, vol. 32, no. 7, pp. 1265–1276, 2013.

[59] J. Bercoff, G. Montaldo, T. Loupas, D. Savery, F. Mézière, M. Fink, and M. Tanter, “Ultrafast compound doppler imaging: Providing full blood flow characterization,” *IEEE transactions on ultrasonics, ferroelectrics, and frequency control*, vol. 58, no. 1, pp. 134–147, 2011.

[60] J. W. Goodman, *Statistical optics*. John Wiley & Sons, 2015.

[61] R. Mallart and M. Fink, “The van cittert–zernike theorem in pulse echo measurements,” *The Journal of the Acoustical Society of America*, vol. 90, no. 5, pp. 2718–2727, 1991.

[62] Y. L. Li and J. J. Dahl, “Coherent flow power doppler (cfpd): Flow detection using spatial coherence beamforming,” *IEEE transactions on ultrasonics, ferroelectrics, and frequency control*, vol. 62, no. 6, pp. 1022–1035, 2015.

[63] C. Kargel, G. Hobenreich, B. Trummer, and M. F. Insana, “Adaptive clutter rejection filtering in ultrasonic strain-flow imaging,” *IEEE Transactions on Ultrasonics, Ferroelectrics, and Frequency Control*, vol. 50, no. 7, pp. 824–835, 2003.

[64] R. Nayak, V. Kumar, J. Webb, A. Gregory, M. Fatemi, and A. Alizad, “Non-contrast agent based small vessel imaging of human thyroid using motion corrected power doppler imaging,” *Scientific reports*, vol. 8, no. 1, pp. 1–15, 2018.

[65] P. Song, A. Manduca, J. D. Trzasko, and S. Chen, “Ultrasound small vessel imaging with block-wise adaptive local clutter filtering,” *IEEE transactions on medical imaging*, vol. 36, no. 1, pp. 251–262, 2016.

[66] A. J. Chee, B. Y. Yiu, and C. Alfred, “A gpu-parallelized eigen-based clutter filter framework for ultrasound color flow imaging,” *IEEE Transactions on Ultrasonics, Ferroelectrics, and Frequency Control*, vol. 64, no. 1, pp. 150–163, 2017.

[67] F. W. Mauldin, F. Viola, and W. F. Walker, “Complex principal components for robust motion estimation,” *IEEE Transactions on Ultrasonics, Ferroelectrics, and Frequency Control*, vol. 57, no. 11, pp. 2437–2449, 2010.

[68] M. Kim, C. K. Abbey, J. Hedhli, L. W. Dobrucki, and M. F. Insana, “Expanding acquisition and clutter filter dimensions for improved perfusion sensitivity,” *IEEE transactions on ultrasonics, ferroelectrics, and frequency control*, vol. 64, no. 10, pp. 1429–1438, 2017.

[69] F. Song, D. Zhang, and X. Gong, “Performance evaluation of eigendecomposition-based adaptive clutter filter for color flow imaging,” *Ultrasonics*, vol. 44, pp. e67–e71, 2006.

[70] B. M. Asl and A. Mahloojifar, “Eigenspace-based minimum variance beamforming applied to medical ultrasound imaging,” *IEEE Transactions on Ultrasonics, Ferroelectrics, and Frequency Control*, vol. 57, no. 11, pp. 2381–2390, 2010.

[71] M.-L. Li, “Adaptive imaging using principal-component-synthesized aperture data,” in *2008 IEEE Ultrasonics Symposium*. IEEE, 2008, pp. 1076–1079.

[72] F. Yang, J. Zhao, C. Liu, Y. Mao, J. Mu, X. Wei, J. Jia, S. Zhang, X. Xin, and J. Tan, “Superb microvascular imaging technique in depicting vascularity in focal liver lesions: more hypervascular supply patterns were depicted in hepatocellular carcinoma,” *Cancer Imaging*, vol. 19, no. 1, pp. 1–11, 2019.

[73] K. Ozgun, J. Tierney, and B. Byram, “A spatial coherence beamformer design for power doppler imaging,” *IEEE transactions on medical imaging*, vol. 39, no. 5, pp. 1558–1570, 2019.

[74] S. T. Torp-Pedersen and L. Terslev, “Settings and artefacts relevant in colour/power doppler ultrasound in rheumatology,” *Annals of the rheumatic diseases*, vol. 67, no. 2, pp. 143–149, 2008.

[75] M. Kim, C. K. Abbey, and M. F. Insana, “Efficiency of us tissue perfusion estimators,” *IEEE transactions on ultrasonics, ferroelectrics, and frequency control*, vol. 63, no. 8, pp. 1131–1139, 2016.

[76] J. Tierney, K. Walsh, H. Griffith, J. Baker, D. Brown, and B. Byram, “Combining slow flow techniques with adaptive demodulation for improved perfusion ultrasound imaging without contrast,” *IEEE transactions on ultrasonics, ferroelectrics, and frequency control*, 2019.

[77] R. Nayak, V. Kumar, J. Webb, M. Fatemi, and A. Alizad, “Non-invasive small vessel imaging of human thyroid using motion-corrected spatiotemporal clutter filtering,” *Ultrasound in medicine & biology*, 2019.

[78] S. I. Nikolov and J. A. Jensen, “In-vivo synthetic aperture flow imaging in medical ultrasound,” *IEEE transactions on ultrasonics, ferroelectrics, and frequency control*, vol. 50, no. 7, pp. 848–856, 2003.

[79] J. Tierney, C. Coolbaugh, T. Towse, and B. Byram, “Adaptive clutter demodulation for non-contrast ultrasound perfusion imaging,” *IEEE transactions on medical imaging*, vol. 36, no. 9, pp. 1979–1991, 2017.

[80] J. Camacho, M. Parrilla, and C. Fritsch, “Phase coherence imaging,” *IEEE transactions on ultrasonics, ferroelectrics, and frequency control*, vol. 56, no. 5, pp. 958–974, 2009.

[81] M. Fink, R. Mallart, and F. Cancre, “The random phase transducer: A new technique for incoherent processing-basic principles and theory,” *IEEE transactions on ultrasonics, ferroelectrics, and frequency control*, vol. 37, no. 2, pp. 54–69, 1990.

[82] N. B. Bottenus and G. E. Trahey, “Equivalence of time and aperture domain additive noise in ultrasound coherence,” *The Journal of the Acoustical Society of America*, vol. 137, no. 1, pp. 132–138, 2015.

[83] Y. L. Li, D. Hyun, I. Durot, J. K. Willmann, and J. J. Dahl, “High sensitivity liver vasculature visualization using a real-time coherent flow power doppler (cfpd) imaging system: A pilot clinical study,” in *2018 IEEE International Ultrasonics Symposium (IUS)*. IEEE, 2018, pp. 1–9.

[84] J. J. Dahl, D. Hyun, Y. Li, M. Jakovljevic, M. A. Bell, W. J. Long, N. Bottenus, V. Kakkad, and G. E. Trahey, “Coherence beamforming and its applications to the difficult-to-image patient,” in *Ultrasonics Symposium (IUS), 2017 IEEE International*. IEEE, 2017, pp. 1–10.

[85] S. O. Dymling, H. W. Persson, and C. H. Hertz, “Measurement of blood perfusion in tissue using doppler ultrasound,” *Ultrasound in Medicine and Biology*, vol. 17, no. 5, pp. 433–444, 1991.

[86] J. M. Rubin, R. S. Adler, J. B. Fowlkes, S. Spratt, J. E. Pallister, J.-F. Chen, and P. L. Carson, “Fractional moving blood volume: estimation with power doppler us.” *Radiology*, vol. 197, no. 1, pp. 183–190, 1995.

[87] R. J. Gillies, P. A. Schomack, T. W. Secomb, and N. Raghunand, “Causes and effects of heterogeneous perfusion in tumors,” *Neoplasia*, vol. 1, no. 3, pp. 197–207, 1999.

[88] D. V. Sahani, N.-S. Holalkere, P. R. Mueller, and A. X. Zhu, “Advanced hepatocellular carcinoma: Ct perfusion of liver and tumor tissue—initial experience,” *Radiology*, vol. 243, no. 3, pp. 736–743, 2007.

[89] T. Loupas, R. Peterson, and R. W. Gill, “Experimental evaluation of velocity and power estimation for ultrasound blood flow imaging, by means of a two-dimensional autocorrelation approach,” *IEEE transactions on ultrasonics, ferroelectrics, and frequency control*, vol. 42, no. 4, pp. 689–699, 1995.

[90] K. Ozgun, J. Tierney, and B. Byram, “An adapted coherent flow power doppler beamforming scheme for improved sensitivity towards blood signal energy,” in *2018 IEEE International Ultrasonics Symposium (IUS)*. IEEE, 2018, pp. 1–4.

[91] A. Stanziola, C. H. Leow, E. Bazigou, P. D. Weinberg, and M.-X. Tang, “Asap: Super-contrast vasculature imaging using coherence analysis and high frame-rate contrast enhanced ultrasound,” *IEEE transactions on medical imaging*, vol. 37, no. 8, pp. 1847–1856, 2018.

[92] A. A. Nair, T. D. Tran, and M. A. L. Bell, "Robust short-lag spatial coherence imaging," *IEEE transactions on ultrasonics, ferroelectrics, and frequency control*, vol. 65, no. 3, pp. 366–377, 2018.

[93] J. F. Kenney and E. Keeping, *Mathematics of statistics. Pt. II*, 2nd ed. D. Van Nostrand Co., Inc, 1951, pp. 215–225.

[94] B. H. Friemel, L. N. Bohs, K. R. Nightingale, and G. E. Trahey, "Speckle decorrelation due to two-dimensional flow gradients," *IEEE transactions on ultrasonics, ferroelectrics, and frequency control*, vol. 45, no. 2, pp. 317–327, 1998.

[95] W. Long, N. Bottenus, and G. E. Trahey, "Lag-one coherence as a metric for ultrasonic image quality," *IEEE transactions on ultrasonics, ferroelectrics, and frequency control*, vol. 65, no. 10, pp. 1768–1780, 2018.

[96] J. A. Jensen, "Field: A program for simulating ultrasound systems," in *10th Nordicbalti Conference on Biomedical Imaging*, vol. 4. Citeseer, 1996, pp. 351–353.

[97] J. A. Jensen and N. B. Svendsen, "Calculation of pressure fields from arbitrarily shaped, apodized, and excited ultrasound transducers," *IEEE transactions on ultrasonics, ferroelectrics, and frequency control*, vol. 39, no. 2, pp. 262–267, 1992.

[98] J. A. Jensen, *Estimation of blood velocities using ultrasound: a signal processing approach.* Cambridge University Press, 1996.

[99] G. Montaldo, M. Tanter, J. Bercoff, N. Benech, and M. Fink, "Coherent plane-wave compounding for very high frame rate ultrasonography and transient elastography," *IEEE transactions on ultrasonics, ferroelectrics, and frequency control*, vol. 56, no. 3, pp. 489–506, 2009.

[100] A. Rodriguez-Molares, O. M. H. Rindal, J. D'hooge, S.-E. Måsøy, A. Austeng, and H. Torp, "The generalized contrast-to-noise ratio," in *2018 IEEE International Ultrasonics Symposium (IUS).* IEEE, 2018, pp. 1–4.

[101] D. Dumont, J. Dahl, E. Miller, J. Allen, B. Fahey, and G. Trahey, "Lower-limb vascular imaging with acoustic radiation force elastography: demonstration of in vivo feasibility," *IEEE transactions on ultrasonics, ferroelectrics, and frequency control*, vol. 56, no. 5, pp. 931–944, 2009.

[102] J. J. Dahl, D. Hyun, M. Lediju, and G. E. Trahey, "Lesion detectability in diagnostic ultrasound with short-lag spatial coherence imaging," *Ultrasonic imaging*, vol. 33, no. 2, pp. 119–133, 2011.

[103] O. M. H. Rindal, A. Rodriguez-Molares, and A. Austeng, "The dark region artifact in adaptive ultrasound beamforming," in *2017 IEEE International Ultrasonics Symposium (IUS).* IEEE, 2017, pp. 1–4.

[104] M. R. Morgan, G. E. Trahey, and W. F. Walker, "Multi-covariate imaging of sub-resolution targets (mist)," *IEEE transactions on medical imaging*, 2019.

[105] K. A. Ozgun and B. C. Byram, “Multidimensional clutter filtering of aperture domain data for improved blood flow sensitivity,” *IEEE Transactions on Ultrasonics, Ferroelectrics, and Frequency Control*, 2021.

[106] P. Song, A. Manduca, J. D. Trzasko, and S. Chen, “Noise equalization for ultrafast plane wave microvessel imaging,” *IEEE transactions on ultrasonics, ferroelectrics, and frequency control*, vol. 64, no. 11, pp. 1776–1781, 2017.

[107] Y. L. Li and J. J. Dahl, “Angular coherence in ultrasound imaging: Theory and applications,” *The Journal of the Acoustical Society of America*, vol. 141, no. 3, pp. 1582–1594, 2017.

[108] P. Song, J. D. Trzasko, A. Manduca, B. Qiang, R. Kadirvel, D. F. Kallmes, and S. Chen, “Accelerated singular value-based ultrasound blood flow clutter filtering with randomized singular value decomposition and randomized spatial downsampling,” *IEEE transactions on ultrasonics, ferroelectrics, and frequency control*, vol. 64, no. 4, pp. 706–716, 2017.

[109] J. Baranger, B. Arnal, F. Perren, O. Baud, M. Tanter, and C. Demené, “Adaptive spatiotemporal svd clutter filtering for ultrafast doppler imaging using similarity of spatial singular vectors,” *IEEE transactions on medical imaging*, vol. 37, no. 7, pp. 1574–1586, 2018.

[110] M. Bayat and M. Fatemi, “Concurrent clutter and noise suppression via low rank plus sparse optimization for non-contrast ultrasound flow doppler processing in microvasculature,” in *2018 IEEE International Conference on Acoustics, Speech and Signal Processing (ICASSP).* IEEE, 2018, pp. 1080–1084.

[111] F. W. Mauldin, D. Lin, and J. A. Hossack, “The singular value filter: A general filter design strategy for pca-based signal separation in medical ultrasound imaging,” *IEEE transactions on medical imaging*, vol. 30, no. 11, pp. 1951–1964, 2011.

[112] A. P. Kadi and T. Loupas, “On the performance of regression and step-initialized iir clutter filters for color doppler systems in diagnostic medical ultrasound,” *IEEE transactions on ultrasonics, ferroelectrics, and frequency control*, vol. 42, no. 5, pp. 927–937, 1995.

[113] H. Torp, “Clutter rejection filters in color flow imaging: A theoretical approach,” *IEEE transactions on ultrasonics, ferroelectrics, and frequency control*, vol. 44, no. 2, pp. 417–424, 1997.

[114] U.-W. Lok, P. Song, J. D. Trzasko, R. Daigle, E. A. Borisch, C. Huang, P. Gong, S. Tang, W. Ling, and S. Chen, “Real time svd-based clutter filtering using randomized singular value decomposition and spatial downsampling for micro-vessel imaging on a verasonics ultrasound system,” *Ultrasonics*, vol. 107, p. 106163, 2020.

[115] C. Xu, J. H. Choi, K. Comess, and Y. Kim, “Color doppler and spectral doppler with high frame-rate imaging,” in *2010 IEEE International Ultrasonics Symposium.* IEEE, 2010, pp. 1562–1566.

[116] M. Kim, Y. Zhu, J. Hedhli, L. W. Dobrucki, and M. F. Insana, "Multidimensional clutter filter optimization for ultrasonic perfusion imaging," *IEEE transactions on ultrasonics, ferroelectrics, and frequency control*, vol. 65, no. 11, pp. 2020–2029, 2018.

[117] F. Vignon, J. S. Shin, S.-W. Huang, and J.-L. Robert, "Adaptive ultrasound clutter rejection through spatial eigenvector filtering," in *2017 IEEE International Ultrasonics Symposium (IUS)*. IEEE, 2017, pp. 1–4.

[118] L. De Lathauwer, B. De Moor, and J. Vandewalle, "A multilinear singular value decomposition," *SIAM journal on Matrix Analysis and Applications*, vol. 21, no. 4, pp. 1253–1278, 2000.

[119] T. G. Kolda and B. W. Bader, "Tensor decompositions and applications," *SIAM review*, vol. 51, no. 3, pp. 455–500, 2009.

[120] R. R. Nadakuditi and A. Edelman, "Sample eigenvalue based detection of high-dimensional signals in white noise using relatively few samples," *IEEE Transactions on Signal Processing*, vol. 56, no. 7, pp. 2625–2638, 2008.

[121] P.-C. Li and M.-L. Li, "Adaptive imaging using the generalized coherence factor," *IEEE transactions on ultrasonics, ferroelectrics, and frequency control*, vol. 50, no. 2, pp. 128–141, 2003.

[122] M. K. Jeong and S. J. Kwon, "Estimation of side lobes in ultrasound imaging systems," *Biomedical Engineering Letters*, vol. 5, no. 3, pp. 229–239, 2015.

[123] P. M. Shankar, "A compound scattering pdf for the ultrasonic echo envelope and its relationship to k and nakagami distributions," *IEEE transactions on ultrasonics, ferroelectrics, and frequency control*, vol. 50, no. 3, pp. 339–343, 2003.

[124] P. Shankar, "A general statistical model for ultrasonic backscattering from tissues," *IEEE transactions on ultrasonics, ferroelectrics, and frequency control*, vol. 47, no. 3, pp. 727–736, 2000.

[125] N. Wang, X. Song, and J. Cheng, "Generalized method of moments estimation of the nakagami-m fading parameter," *IEEE transactions on wireless communications*, vol. 11, no. 9, pp. 3316–3325, 2012.

[126] A. Abdi and M. Kaveh, "Performance comparison of three different estimators for the nakagami m parameter using monte carlo simulation," *IEEE communications letters*, vol. 4, no. 4, pp. 119–121, 2000.

[127] A. Rodriguez-Molares, O. M. H. Rindal, O. Bernard, A. Nair, M. A. L. Bell, H. Liebgott, A. Austeng *et al.*, "The ultrasound toolbox," in *2017 IEEE International Ultrasonics Symposium (IUS)*. IEEE, 2017, pp. 1–4.

[128] N. Vervliet, O. Debals, and L. De Lathauwer, "Tensorlab 3.0—numerical optimization strategies for large-scale constrained and coupled matrix/tensor factorization," in *2016 50th Asilomar Conference on Signals, Systems and Computers*. IEEE, 2016, pp. 1733–1738.

[129] A. J. Chee and C. Alfred, “Receiver-operating characteristic analysis of eigen-based clutter filters for ultrasound color flow imaging,” *IEEE transactions on ultrasonics, ferroelectrics, and frequency control*, vol. 65, no. 3, pp. 390–399, 2017.

[130] S.-L. Wang, M.-L. Li, and P.-C. Li, “Estimating the blood velocity vector using aperture domain data,” *IEEE transactions on ultrasonics, ferroelectrics, and frequency control*, vol. 54, no. 1, pp. 70–78, 2006.

[131] X. Mestre, “Improved estimation of eigenvalues and eigenvectors of covariance matrices using their sample estimates,” *IEEE Transactions on Information Theory*, vol. 54, no. 11, pp. 5113–5129, 2008.

[132] K. Ozgun and B. Byram, “A general framework for channel domain svd clutter filtering,” in *2019 IEEE International Ultrasonics Symposium (IUS)*. IEEE, 2019, pp. 2246–2248.

[133] N. Vannieuwenhoven, R. Vandebril, and K. Meerbergen, “A new truncation strategy for the higher-order singular value decomposition,” *SIAM Journal on Scientific Computing*, vol. 34, no. 2, pp. A1027–A1052, 2012.

[134] J. Brown, K. Christensen-Jeffries, S. Harput, G. Zhang, J. Zhu, C. Dunsby, M.-X. Tang, and R. J. Eckersley, “Investigation of microbubble detection methods for super-resolution imaging of microvasculature,” *IEEE transactions on ultrasonics, ferroelectrics, and frequency control*, vol. 66, no. 4, pp. 676–691, 2019.

[135] S. Adabi, S. Ghavami, M. Fatemi, and A. Alizad, “Non-local based denoising framework for in vivo contrast-free ultrasound microvessel imaging,” *Sensors*, vol. 19, no. 2, p. 245, 2019.

[136] Y. Desailly, A.-M. Tissier, J.-M. Correas, F. Wintzenrieth, M. Tanter, and O. Couture, “Contrast enhanced ultrasound by real-time spatiotemporal filtering of ultrafast images,” *Physics in Medicine & Biology*, vol. 62, no. 1, p. 31, 2016.

[137] C. F. Dietrich, C. P. Nolsøe, R. G. Barr, A. Berzigotti, P. N. Burns, V. Cantisani, M. C. Chammas, N. Chaubal, B. I. Choi, D.-A. Clevert *et al.*, “Guidelines and good clinical practice recommendations for contrast-enhanced ultrasound (ceus) in the liver–update 2020 wfumb in cooperation with efsumb, afsumb, aium, and flaus,” *Ultrasound in medicine & biology*, 2020.

[138] S. R. Wilson, A. Lyshchik, F. Piscaglia, D. Cosgrove, H.-J. Jang, C. Sirlin, C. F. Dietrich, T. K. Kim, J. K. Willmann, and Y. Kono, “Ceus li-rads: algorithm, implementation, and key differences from ct/mri,” *Abdominal radiology*, vol. 43, no. 1, pp. 127–142, 2018.

[139] T. J. Dubinsky, J. Revels, S. Wang, G. Toia, R. Sonneborn, D. S. Hippe, and T. Erpelding, “Comparison of superb microvascular imaging with color flow and power doppler imaging of small hepatocellular carcinomas,” *Journal of Ultrasound in Medicine*, vol. 37, no. 12, pp. 2915–2924, 2018.

[140] M.-N. He, K. Lv, Y.-X. Jiang, and T.-A. Jiang, "Application of superb microvascular imaging in focal liver lesions," *World journal of gastroenterology*, vol. 23, no. 43, p. 7765, 2017.

[141] B. Oosterveld, J. Thijssen, P. Hartman, R. Romijn, and G. Rosenbusch, "Ultrasound attenuation and texture analysis of diffuse liver disease: methods and preliminary results," *Physics in Medicine & Biology*, vol. 36, no. 8, p. 1039, 1991.

[142] M. A. L. Bell, J. J. Dahl, and G. E. Trahey, "Resolution and brightness characteristics of short-lag spatial coherence (slsc) images," *IEEE transactions on ultrasonics, ferroelectrics, and frequency control*, vol. 62, no. 7, pp. 1265–1276, 2015.

[143] K. A. Ozgun and B. C. Byram, "An adaptive coherent flow power doppler beamforming scheme for improved sensitivity towards blood signal energy," in *Medical Imaging 2019: Ultrasonic Imaging and Tomography*, vol. 10955. International Society for Optics and Photonics, 2019, p. 109550H.

[144] Y. R. Nobel and D. S. Goldberg, "Variable use of meld exception points in patients with neuroendocrine tumors metastatic to the liver and its impact on patient outcomes," *Transplantation*, vol. 99, no. 11, p. 2341, 2015.

[145] P.-Y. Tao, Z.-S. Zhang, T.-C. Wang, M.-Q. Yu, and Y.-D. Xiao, "A predictive model of incomplete response after transarterial chemoembolization for early or intermediate stage of hepatocellular carcinoma: consideration of hepatic angiographic and cross-sectional imaging," *Abdominal Radiology*, vol. 46, no. 2, pp. 581–589, 2021.

[146] I. Miki, S. Murata, F. Uchiyama, D. Yasui, T. Ueda, F. Sugihara, H. Saito, H. Yamaguchi, R. Murakami, C. Kawamoto *et al.*, "Evaluation of the relationship between hepatocellular carcinoma location and transarterial chemoembolization efficacy," *World journal of gastroenterology*, vol. 23, no. 35, p. 6437, 2017.

[147] D. B. Brown, C. E. Fundakowski, M. Lisker-Melman, J. S. Crippin, T. K. Pilgram, W. Chapman, and M. D. Darcy, "Comparison of meld and child-pugh scores to predict survival after chemoembolization for hepatocellular carcinoma," *Journal of vascular and interventional radiology*, vol. 15, no. 11, pp. 1209–1218, 2004.

[148] F. Hucke, M. Pinter, I. Graziadei, S. Bota, W. Vogel, C. Müller, H. Heinzl, F. Waneck, M. Trauner, M. Peck-Radosavljevic *et al.*, "How to state suitability and start transarterial chemoembolization in patients with intermediate stage hepatocellular carcinoma," *Journal of hepatology*, vol. 61, no. 6, pp. 1287–1296, 2014.

[149] G. Vesselle, C. Quirier-Leleu, S. Velasco, F. Charier, C. Silvain, S. Boucebci, P. Ingrand, and J.-P. Tasu, "Predictive factors for complete response of chemoembolization with drug-eluting beads (deb-tace) for hepatocellular carcinoma," *European radiology*, vol. 26, no. 6, pp. 1640–1648, 2016.

[150] L. Kadalayil, R. Benini, L. Pallan, J. O'beirne, L. Marelli, D. Yu, A. Hackshaw, R. Fox, P. Johnson, A. Burroughs *et al.*, "A simple prognostic scoring system for patients receiving transarterial embolisation for hepatocellular cancer," *Annals of oncology*, vol. 24, no. 10, pp. 2565–2570, 2013.

[151] J. Iwazawa, S. Ohue, N. Hashimoto, O. Muramoto, and T. Mitani, "Clinical utility and limitations of tumor-feeder detection software for liver cancer embolization," *European journal of radiology*, vol. 82, no. 10, pp. 1665–1671, 2013.

[152] C. Park, J. H. Kim, P. H. Kim, S. Y. Kim, D. I. Gwon, H. H. Chu, M. Park, J. Hur, J. Y. Kim, and D. J. Kim, "Imaging predictors of survival in patients with single small hepatocellular carcinoma treated with transarterial chemoembolization," *Korean Journal of Radiology*, vol. 22, no. 2, p. 213, 2021.

[153] S. Wu, H. Charles, J. Park, A. Goldenberg, and A. Deipolyi, "Obesity conveys poor outcome in patients with hepatocellular carcinoma treated by transarterial chemoembolization," *Diagnostic and interventional imaging*, vol. 98, no. 1, pp. 37–42, 2017.

[154] R. Nayak, J. MacNeill, C. Flores, J. Webb, M. Fatemi, and A. Alizad, "Quantitative assessment of ensemble coherency in contrast-free ultrasound microvasculature imaging," *Medical Physics*, 2021.

[155] R. Nayak, N. Nawar, J. Webb, M. Fatemi, and A. Alizad, "Impact of imaging cross-section on visualization of thyroid microvessels using ultrasound: Pilot study," *Scientific reports*, vol. 10, no. 1, pp. 1–9, 2020.

[156] J. E. Tierney, M. George, C. Coolbaugh, T. Towse, and B. C. Byram, "Combining adaptive demodulation with singular value decomposition filtering for improved non-contrast perfusion ultrasound imaging," in *Medical Imaging 2018: Ultrasonic Imaging and Tomography*, vol. 10580. International Society for Optics and Photonics, 2018, p. 1058008.

[157] D. Hyun, A. L. C. Crowley, and J. J. Dahl, "Efficient strategies for estimating the spatial coherence of backscatter," *IEEE transactions on ultrasonics, ferroelectrics, and frequency control*, vol. 64, no. 3, pp. 500–513, 2016.

[158] E. Mace, G. Montaldo, B.-F. Osmanski, I. Cohen, M. Fink, and M. Tanter, "Functional ultrasound imaging of the brain: theory and basic principles," *IEEE transactions on ultrasonics, ferroelectrics, and frequency control*, vol. 60, no. 3, pp. 492–506, 2013.

[159] O. M. H. Rindal, A. Austeng, A. Fatemi, and A. Rodriguez-Molares, "The effect of dynamic range alterations in the estimation of contrast," *IEEE transactions on ultrasonics, ferroelectrics, and frequency control*, vol. 66, no. 7, pp. 1198–1208, 2019.

[160] N. Bottenus, B. Byram, and D. Hyun, "Histogram matching for visual ultrasound image comparison," *IEEE Transactions on Ultrasonics, Ferroelectrics, and Frequency Control*, 2020.

[161] H. Bendjador, T. Deffieux, and M. Tanter, “The svd beamformer: Physical principles and application to ultrafast adaptive ultrasound,” *IEEE transactions on medical imaging*, vol. 39, no. 10, pp. 3100–3112, 2020.

[162] A. L. Cheng, D. Amarapurkar, Y. Chao, P.-J. Chen, J.-F. Geschwind, K. L. Goh, K.-H. Han, M. Kudo, H. C. Lee, R.-C. Lee *et al.*, “Re-evaluating transarterial chemoembolization for the treatment of hepatocellular carcinoma: Consensus recommendations and review by an international expert panel,” *Liver International*, vol. 34, no. 2, pp. 174–183, 2014.

[163] A. Weeks, J. Tierney, and B. Byram, “Block-wise independent component analysis for slow flow non-contrast ultrasound imaging,” in *2019 IEEE International Ultrasonics Symposium (IUS)*. IEEE, 2019, pp. 2256–2258.

[164] A. Weeks, J. T. Stanton, and B. Byram, “A novel, adaptive hierarchical clustering approach for independent component sorting for block-wise ica filtering,” in *Medical Imaging 2021: Ultrasonic Imaging and Tomography*, vol. 11602. International Society for Optics and Photonics, 2021, p. 116020O.

[165] J. Tierney, J. Baker, D. Brown, D. Wilkes, and B. Byram, “Independent component-based spatiotemporal clutter filtering for slow flow ultrasound,” *IEEE transactions on medical imaging*, vol. 39, no. 5, pp. 1472–1482, 2019.

[166] B. Byram, K. Dei, J. Tierney, and D. Dumont, “A model and regularization scheme for ultrasonic beamforming clutter reduction,” *IEEE transactions on ultrasonics, ferroelectrics, and frequency control*, vol. 62, no. 11, pp. 1913–1927, 2015.

[167] C. Khan, K. Dei, S. Schlunk, K. Ozgun, and B. Byram, “A real-time, gpu-based implementation of aperture domain model image reconstruction,” *IEEE Transactions on Ultrasonics, Ferroelectrics, and Frequency Control*, vol. 68, no. 6, pp. 2101–2116, 2021.

[168] S. Schlunk and B. Byram, “Using admire to improve minimum variance performance in the presence of reverberation clutter,” in *Medical Imaging 2021: Ultrasonic Imaging and Tomography*, vol. 11602. International Society for Optics and Photonics, 2021, p. 116020Q.

[169] J. Tierney, A. Luchies, M. Berger, and B. Byram, “Evaluating input domain and model selection for deep network ultrasound beamforming,” *IEEE Transactions on Ultrasonics, Ferroelectrics, and Frequency Control*, 2021.

[170] B. Byram, J. Tierney, and M. Berger, “Ultrasound beamforming using deep networks,” *The Journal of the Acoustical Society of America*, vol. 148, no. 4, pp. 2446–2446, 2020.

[171] E. P. Vienneau and B. C. Byram, “A coded excitation framework for increased signal-to-noise ratio of in vivo ultrasound power doppler imaging,” in *Medical Imaging 2021: Ultrasonic Imaging and Tomography*, vol. 11602. International Society for Optics and Photonics, 2021, p. 116020P.

[172] A. M. Covey and S. M. Hussain, “Liver-directed therapy for hepatocellular carcinoma: an overview of techniques, outcomes, and posttreatment imaging findings,” *American Journal of Roentgenology*, vol. 209, no. 1, pp. 67–76, 2017.

[173] B. Jin, D. Wang, R. J. Lewandowski, A. Riaz, R. K. Ryu, K. T. Sato, A. C. Larson, R. Salem, and R. A. Omary, “The impact of chemoembolization endpoints on survival in hepatocellular carcinoma patients,” *AJR. American journal of roentgenology*, vol. 196, no. 4, p. 919, 2011.

[174] N. Kothary, C. Takehana, K. Mueller, P. Sullivan, A. Tahvildari, V. Sidhar, J. Rosenberg, J. D. Louie, and D. Y. Sze, “Watershed hepatocellular carcinomas: the risk of incomplete response following transhepatic arterial chemoembolization,” *Journal of Vascular and Interventional Radiology*, vol. 26, no. 8, pp. 1122–1129, 2015.

Appendix A

Elaboration on Location-Scale Probability

As asserted in Section 2.6.1, location-scale probability statistics, which includes the normal distribution, are used to obtain the model of ppCFPD pixel intensity for noise signals. The family of location-scale probability distributions assert that for any random variable X described by a class of distributions, Ω, that belongs to the location-scale family, the distribution $Y \overset{d}{=} a + bX$ is also a member of Ω.

This means that for two independent, normally-distributed random variables, $X_1 \sim N(\mu_1, \sigma_1^2)$ and $X_2 \sim N(\mu_2, \sigma_2^2)$, their linear combination will also be normally distributed,

$$aX_1 + bX_2 \sim N(a\mu_1 + b\mu_2,\, a^2\sigma_1^2 + b^2\sigma_2^2). \tag{A.1}$$

As posed previously in Equation (2.16), the expression for the ppCFPD pixel intensity for a signal containing only noise is

$$\text{ppCFPD} = AH\sigma_{noise}^2 \frac{1}{M} \sum_{m=1}^{M} \frac{1}{N-m} \sum_{i=1}^{N-m} \rho_{y_i y_{i+m}},$$

where we describe the variable $\rho_{y_i y_{i+m}}$ to be a normally distributed random variable with calculable mean and variance as described in 2.18, assuming that $\rho_{y_i y_{i+m}}$ is approximately equal to its comparable Z-score, $z(m)$, for low correlation values as obtained in the case of IID noise.

The remaining variables in Equation (2.16) are defined as constants, such that the ppCFPD pixel intensity shares a linear relationship with $\rho_{y_i y_{i+m}}$, following the assertions in Equation (A.1). This allows us to obtain the final probability distribution for the ppCFPD pixel intensity described in Equation (2.19).

Appendix B

Closed Form Approximation of a Harmonic number

We note that an approximate closed form solution for generalized harmonic numbers is formulated as

$$\mathcal{H}_n \approx \ln(n) + \gamma + \frac{1}{2n} - \sum_{k=1}^{\infty} \frac{B_{2k}}{2kn^{2k}}, \tag{B.1}$$

where B_k are Bernoulli numbers and γ is the Euler-Mascheroni constant, which describes how harmonic numbers asymptotically approach the natural log. A closed form approximation can be obtained using a truncated series

$$\mathcal{H}_n \approx \ln(n) + \gamma + \frac{1}{2n} - \frac{1}{12n^2} + \frac{1}{120n^4}. \tag{B.2}$$

The accuracy of using the truncated series approximation in the difference equation $\Delta\mathcal{H} = (\mathcal{H}_{\text{N-1}} - \mathcal{H}_{\text{N-M-1}})$ is depicted below in Table 2.1. The relative error was evaluated for N = 128 elements and M = 20 lags as

$$\text{Error, dB} = 20\log_{10}\left(\frac{|\Delta\hat{\mathcal{H}} - \Delta\mathcal{H}|}{\Delta\mathcal{H}}\right). \tag{B.3}$$

Table 2.1: Accuracy of $\mathcal{H}_{\text{N-1}} - \mathcal{H}_{\text{N-M-1}}$ Approximation

Approximation Form	**Error, dB**
$\mathcal{H}_{\text{a}} - \mathcal{H}_{\text{b}} = \ln(\frac{\text{a}}{\text{b}})$	-47.3 dB
$\mathcal{H}_{\text{a}} - \mathcal{H}_{\text{b}} = \ln(\frac{\text{a}}{\text{b}}) + \frac{\text{a}^{-1} - \text{b}^{-1}}{2}$	-98.1 dB
$\mathcal{H}_{\text{a}} - \mathcal{H}_{\text{b}} = \ln(\frac{\text{a}}{\text{b}}) + \frac{\text{a}^{-1} - \text{b}^{-1}}{2} - \frac{\text{a}^{-2} - \text{b}^{-2}}{12}$	-194.7 dB

Appendix C

Power Doppler Noise Statistics

The formula for power Doppler shown in Equation (2.1) may be expanded to

$$\mathrm{PD} = \sum_{a=1}^{A} \left(\sum_{i=1}^{N} y_i(n) \right)^2 , \tag{C.1}$$

where the power Doppler signal is computed as the squared sum of N delayed channel signals, $y_i(n)$, summed over a temporal ensemble, A.

If we assert the same assumptions as in the ppCFPD analysis, namely that $y_i(n) \sim N(0, \sigma^2_{\text{noise}})$, we find that

$$\sum_{i=1}^{N} y_i(n) \sim N(0, N\sigma^2_{\text{noise}}). \tag{C.2}$$

Squaring this normal term yields a Gamma distribution,

$$\left(\sum_{i=1}^{N} y_i(n) \right)^2 \sim \Gamma(\frac{1}{2}, 2N\sigma^2_{\text{noise}}), \tag{C.3}$$

of shape $k = \frac{1}{2}$ and scale $\theta = 2N\sigma^2_{\text{noise}}$. The summation of A Gamma distributed parameters, X_i, with the same scale, θ, produces

$$\sum_{i=1}^{A} X_i \sim \Gamma\left(\sum_{i=1}^{N} k_i, \theta \right), \tag{C.4}$$

hence we find that power Doppler pixel intensity computed for channel signals containing only noise is distributed

$$\mathrm{PD} \sim \Gamma\left(\frac{A}{2}, 2N\sigma^2_{\text{noise}} \right), \tag{C.5}$$

with a non-zero mean and variance of

$$\begin{aligned} \mu_{\text{pixel}} &= k\theta = AN\sigma^2_{\text{noise}} \\ \sigma^2_{\text{pixel}} &= k\theta^2 = 2A(N\sigma^2_{\text{noise}})^2. \end{aligned}$$